DEVELOPMENT OF FUNCTIONALIZED ORGANIC

NANOPARTICLES FOR CANCER

DIAGNOSIS AND THERAPY

Kittipan Siwawannapong

A Thesis Submitted in Partial Fulfillment of the Requirement for the

Degree of Master of Science in Chemistry

Suranaree University of Technology

Academic Year 2019

การพัฒนาเชิงหน้าที่ของอนุภาคนาโนอินทรีย์เฉพาะทาง
เพื่อใช้สำหรับการวินิจฉัยและรักษาโรคมะเร็ง

นายกิตติพันธ์ ศิวะวรรณพงศ์

วิทยานิพนธ์นี้เป็นส่วนหนึ่งของการศึกษาตามหลักสูตรปริญญาวิทยาศาสตรมหาบัณฑิต
สาขาวิชาเคมี
มหาวิทยาลัยเทคโนโลยีสุรนารี
ปีการศึกษา 2562

DEVELOPMENT OF FUNCTIONALIZED ORGANIC

NANOPARTICLES FOR CANCER DIAGNOSIS AND THERAPY

Suranaree University of Technology has approved this thesis submitted in partial fulfillments of the requirement for a Master's degree.

Thesis Examining Committee

_____

(Prof. Dr. James R. Ketudat-Cairns)

Chairperson

_____

(Asst. Prof. Dr. Anyanee Kamkaew)

Member (Thesis Advisor)

_____

(Assoc. Prof. Dr. Sanchai Prayoonpokarach)

Member

_____

(Asst. Prof. Dr. Theeranun Siritanon)

Member

_____

(Asst. Prof. Dr. Parinya Noisa)

Member

_____ _____

(Assoc. Prof. Flt Lt Dr. Kontorn Chamniprasart) (Assoc. Prof. Dr. Worawat Meevasana)

Vice Rector for Academic Affairs Dean of Institute of Science

and Internationalization

กิตติพันธ์ ศิวะวรรณพงศ์ : การพัฒนาเชิงหน้าที่ของอนุภาคนาโนอินทรีย์เฉพาะทางเพื่อใช้สำหรับการวินิจฉัยและรักษาโรคมะเร็ง (DEVELOPMENT OF FUNCTIONALIZED ORGANIC NANOPARTICLES FOR CANCER DIAGNOSIS AND THERAPY) อาจารย์ที่ปรึกษา : ผู้ช่วยศาสตราจารย์ ดร.อัญญานี คำแก้ว, 96 หน้า.

การที่ผู้ป่วยโรคมะเร็งได้รับการรักษาจากยาบางชนิดเป็นระยะเวลาที่ยาวนานอาจพบภาวะแทรกซ้อนอื่น ๆ ตามมา เนื่องจากขนาดของอนุภาคที่ไม่เหมาะสม ทำให้ขับออกจากร่างกายได้ช้าและนำไปสู่การสะสมของตัวยาที่อวัยวะต่าง ๆ จนเกิดความเป็นพิษขึ้น ดังนั้น เพื่อลดโอกาสในการสะสมตัวของอนุภาคยาที่อาจนำไปสู่ผลกระทบในระยะยาว อนุภาคยาขนาดนาโนซึ่งสามารถถูกกำจัดออกจากร่างกายได้อย่างรวดเร็วผ่านระบบปัสสาวะ จึงมีความน่าสนใจต่อการศึกษาค้นคว้า เพื่อลดภาวะเสี่ยงที่อาจเกิดขึ้นให้ได้มากที่สุด งานวิจัยนี้มีจุดมุ่งหมายหลักในการสังเคราะห์อนุภาคนาโนของยาที่สามารถทำหน้าที่ได้ทั้งใช้วินิจฉัย ใช้ทำลายเนื้อเยื่อมะเร็งแบบโฟโตไดนามิกและสามารถถูกกำจัดออกจากร่างกายผ่านระบบปัสสาวะได้

ไพโรฟีโอฟอบาย-เอ (Pa) ซึ่งเป็นสารไวแสงที่ไม่สามารถละลายน้ำได้ ถูกดัดแปลงให้เชื่อมกับพอลิเอทิลีนไกลคอล (PEG) ด้วยปฏิกิริยาการเกิดพันธะเอไมด์ เพื่อสร้างอนุภาคนาโนดอทของ Pa-PEG ที่สามารถละลายน้ำได้ดี เมื่อทำการระบุเอกลักษณ์สมบัติเชิงแสงพบว่าอนุภาคนาโนดอทของ Pa-PEG สามารถปลดปล่อยแสงฟลูออเรสเซนต์ได้ดี นอกจากนั้น ความยาวคลื่นที่สารสามารถดูดกลืนได้สูงที่สุดในช่วงของแสงสีแดงเลื่อนไป (red-shift of Q-band) จาก 680 นาโนเมตรไปยัง 710 นาโนเมตร หลังจากการดัดแปลงสาร ทำให้เป็นประโยชน์ต่อการเกิดปรากฏการณ์การสร้างคลื่นความร้อนเมื่อได้รับการกระตุ้นด้วยแสงอีกด้วย จึงทำให้สามารถนำอนุภาคนาโนดอทของ Pa-PEG ไปใช้ประโยชน์ในการถูกติดตามด้วยภาพถ่ายแบบโฟโตอคลูสติกได้ และเมื่อตรวจสอบความสามารถในการสร้างออกซิเจนโมเลกุลเดี่ยว (singlet oxygen) ของอนุภาคนาโนดอทของ Pa-PEG ในสารละลาย โดยการฉายแสงที่ความยาวคลื่น 660 นาโนเมตร พบว่ามีความสามารถในการสร้างออกซิเจนโมเลกุลเดี่ยวในปริมาณความเข้มข้นที่สูงกว่าโมเลกุล Pa อิสระ ซึ่งเป็นการยืนยันความสามารถในการเกิดปรากฏการณ์โฟโตไดนามิกหลังเพิ่มความสามารถในการละลายน้ำให้กับโมเลกุล Pa

การศึกษาความสามารถในการยับยั้งทำลายเซลล์มะเร็งในระดับเซลล์ (in vitro) พบว่า
เซลล์มะเร็งที่ถูกบ่มด้วยอนุภาคนาโนของ Pa-PEG จะถูกทำลายเป็นส่วนมากหลังการฉายแสงที่
ความยาวคลื่น 660 นาโนเมตร นาน 30 นาที ทั้งนี้เมื่อทำการฉีดอนุภาคนาโน Pa-PEG เข้าสู่ระบบ
หมุนเวียนเลือดทางหางของหนูทดลองที่ถูกปลูกถ่ายมะเร็งไว้บนหลัง และทำการติดตามการสะสม
ของอนุภาคโดยการถ่ายภาพแสงฟลูออเรสเซนต์และโฟโตอคูสติก พบว่าเทคนิคการถ่ายภาพทั้งสอง
ให้ข้อมูลที่สอดคล้องกันว่าอนุภาคนาโนของ Pa-PEG จะสะสมตัวในความเข้มข้นสูงที่สุดที่ 8
ชั่วโมง หลังจากฉีดอนุภาคนาโนของยา Pa-PEG เข้าสู่ร่างกายของหนูทดลองแล้ว ทำให้เลือก
ช่วงเวลาดังกล่าวในการทำการรักษาแบบโฟโตไดนามิก และพบว่าเซลล์มะเร็งถูกทำลายอย่างมี
ประสิทธิภาพด้วยการฉายแสงความยาวคลื่น 660 นาโนเมตร นอกจากนี้ จากการศึกษาการกระจาย
ของอนุภาคนาโน Pa-PEG ในอวัยวะต่าง ๆ ด้วยเทคนิคการถ่ายภาพ พบว่ามีสัญญาณแสงฟลูออเรส
เซนต์และโฟโตอูสติกความเข้มสูงที่ไตของหนูทดลองเมื่อเทียบกับอวัยวะอื่น ๆ เป็นการบ่งชี้ว่า
อนุภาคนาโน Pa-PEG นี้สามารถถูกกำจัดออกจากร่างกายโดยระบบปัสสาวะได้ดี ซึ่งสามารถทำให้
ลดผลกระทบในระยะยาวของการรักษามะเร็งได้

ในงานวิจัยนี้ คณะผู้วิจัยได้แสดงคุณสมบัติโดดเด่นและมีประสิทธิภาพของอนุภาคนาโน
ของยา Pa-PEG ที่สามารถทำหน้าที่ได้ทั้งเป็นตัววินิจฉัยและทำลายมะเร็ง อีกทั้งยังสามารถถูกกำจัด
ออกจากร่างกายได้โดยง่าย ซึ่งจะเป็นประโยชน์ต่อการศึกษาเพิ่มเติมเพื่อนำไปประยุกต์ใช้ในระดับ
คลินิกต่อไป

สาขาวิชาเคมี   ลายมือชื่อนักศึกษา_____
ปีการศึกษา 2562   ลายมือชื่ออาจารย์ที่ปรึกษา_____

KITTIPAN SIWAWANNAPONG : DEVELOPMENT OF
FUNCTIONALIZED ORGANIC NANOPARTICLES FOR CANCER
DIAGNOSIS AND THERAPY. THESIS ADVISOR : ASST. PROF.
ANYANEE KAMKAEW, Ph.D. 96 PP.

Pa-PEG ULTRA-SMALL NANOPARTICLES/ DUAL-MODAL IMAGING/
PHOTODYNAMIC THERAPY/ RENAL CLEARANCE/ TOXICITY

Some severe side effects can be observed in cancer patients who receive a
treatment for a long time; moreover, some drug tend to accumulate inside the body
organs due to its large size with sluggish elimination. Ultra-small nanomedicine is a
promising approach that takes advantage of its small size to minimize the considerable
long-term effect by being rapidly cleared out from the body via the renal pathway.
Therefore, an ultra-small theranostic drug with renal excretable behavior is sought-
after for improving human health. In this work, we reported a versatile ultra-small
nanomaterial that can be both a cancer diagnostic and therapeutic agent for
photodynamic therapy (PDT), with renal clearable function. Pyropheophorbide-a (Pa)
was conjugated with polyethylene glycol to form Pa-PEG nanodots (NDs) via a facile
amide bond coupling reaction. Optical characterization indicated that Pa-PEG NDs
serve as fluorescent imaging agents. Moreover, a red-shift of the Q-band from 680 nm
to 710 nm after modification offered photoacoustic imaging benefiting from heat
pulse signal generation in the more extended NIR range. Singlet oxygen detection
revealed that a higher singlet oxygen concentration was generated during 660 nm light
irradiation compared to that of free Pa molecules in water, confirming the greater

occurrence of photodynamic effect. *In vitro* studies were carried out to confirm the PDT effect with cancer cells; most of the malignant cells were eradicated after cells were exposed to Pa-PEG NDs and light at 660 nm for 30 min. After intravenous injection of nanomaterials into the mice, fluorescence (FL), and photoacoustic (PA) dual-modal imaging consistently suggested that Pa-PEG NDs showed maximum concentration at the tumor site after 8 hours and this was the optimal time for *in vivo* PDT treatment. Finally, the tumors on mice injected with Pa-PEG NDs were effectively inhibited by PDT treatment. Furthermore, nanomaterial biodistribution displayed a higher FL/PA signal in kidneys over other organs, implying these ultra-small nanodots could pass through the kidney's filtration membrane, which would be rapidly eliminated out of the body to reduce the long-term effect. Therefore, we demonstrated the remarkable properties of Pa-PEG NDs that can be both *in vivo* diagnostic and photodynamic therapeutic agents with renal clearable behavior for future clinical translation.
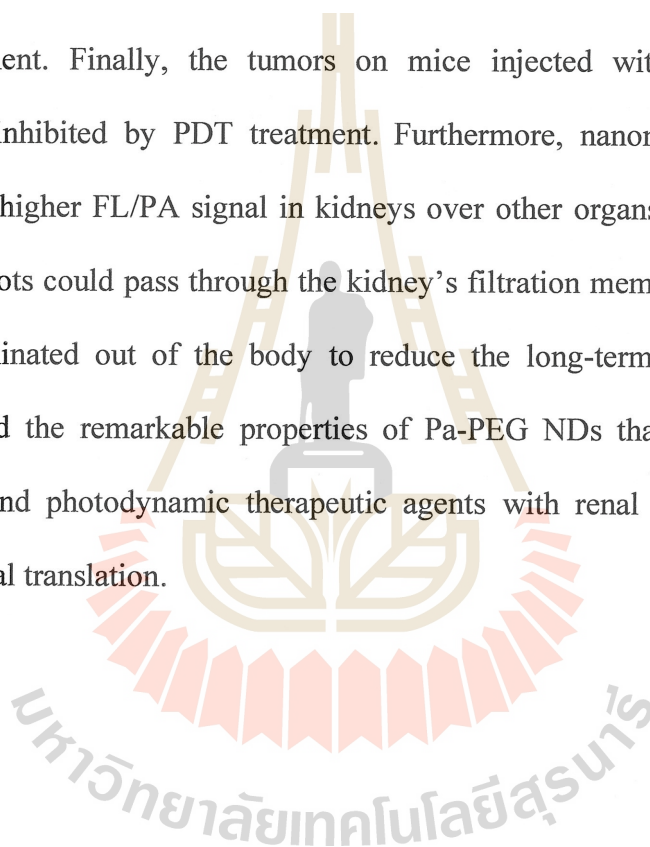
School of Chemistry	Student's Signature_____Kittipan._____
Academic Year 2019	Advisor's Signature_____

ACKNOWLEDGEMENTS

This thesis cannot be completed if I did not receive a tremendous momentum from my advisor, Asst. Prof. Anyanee Kamkaew. In the beginning, I enrolled in M.Sc. program, I had low passion driven to pursue a doctoral degree further, but after she gave me an enormous motivation by allowing me to expand my research experience overseas. My perspective in the research field has enlarged with a passion for pursuing a Ph.D. program. Therefore, I would like to record my sincere gratitude to my the best advisor for her motivation to push me to graduation, her patience for revising all related documents, her encouragement before and after every presentations, her friendliness that reduced all of stress, her advice and guidance from the early stage of this research, her celebration for my success, and her time. If I do not have her as an advisor, I could not have imagined the way I am experiencing at this time. She is an excellent advisor, eternally.

Importantly, this thesis also could not have been finished if I did not obtain vast support from Assoc. Prof. Liang Cheng, a co-advisor at Soochow University. He has been very kind to me since he picked me up at an airport. When any experiments failed, he had never criticized me about those failures, but he always cheered up and encouraged me to repeat it until I obtained the prospective results. He is also my role model, I have never seen any professors that has high eager to do research by themselves like him, his hard-working inspired me to be more active in order to complete my research. Even he had a lot of work, I appreciated that he managed his time to discuss the results with me.

Conducting research in China with him is the best memories for me. Thanks for his enduring support, patience, and everything. It is my honor to be one of his students.

Moreover, I also want to express my appreciation to Chinese colleagues and AK lab members for their supporting. They always facilitated me everything as they can, and I could touch that they were willing to help me every time when I asked them for help: find chemical substance, operate the instrument, coach me to do all unfamiliar assays, and give me a useful suggestion. I might not accomplish my research if I did not obtain all of those, as mentioned above, they are the best mentor for me. Finally, I would like to give special thanks to all the Chinese friends who sustain my life in China when I newly spent my time until the end.

Thanks to the Development and Promotion of Science and Technology Talents Project (DPST) for tuition fees, living expenses, travel grants, and so on. In addition to all lecturers in the School of Chemistry, the Suranaree University of Technology, thanks for their good attitudes and their kind to push me to be a good student. Also, all staff at the Center for Scientific and Technological Equipment for their assistance and suggestion for the access of instruments.

Last but not least, special thanks to my parents: Mr. Ataporn Siwawannapong and Ms. Warinporn Chuenarom, my younger brother, my deceased grandmother, and other family members for their unconditional love, encouragement and supporting me spiritually during my education and throughout my whole life.

Kittipan Siwawannapong

CONTENTS

CONTENTS (Continued)

CONTENTS (Continued)

CONTENTS (Continued)

CONTENTS (Continued)

LIST OF TABLES

LIST OF FIGURES

LIST OF FIGURES (Continued)

LIST OF FIGURES (Continued)

LIST OF FIGURES (Continued)

CHAPTER I

INTRODUCTION

1.1 Significance of the study

Cancer is one of the significant causes of illness and death worldwide. The top three major cancer types in 2018 are cancers of the lung, female breast, and colorectum. World Health Organization (WHO) reported that the global cancer burden is approximated to be 18.1 million new cases and 9.6 million deaths in 2018, and new cases are expected to rise up over the next decade. There are many reasons for the increasing rate of cancer burden, such as population growth and aging, as well as the changing prevalence of specific causes of cancer linked to social and economic development. Notably, almost 70% of deaths from cancer were found in low- and middle-income countries (WHO, 2018). To reduce the cancer growth rate, several treatment methods have been developed to destroy malignant cells in clinical practice, for example, cancer surgery, radiation therapy, or chemotherapy. However, there are many harmful severe effects of those treatments, including: (i) wound complication and poor healing from surgery, (ii) surrounding tissue damage in radiation therapy, and (iii) unexpected results that occurred from chemotherapy: nausea, vomiting, immune depression, and hair loss that make a great distress to all female cancer patients (Goldsmith, 1969; Petrelli et al., 2009). Currently, many scientists have been developing and exploring new cancer curing methods to improve therapeutic efficacy with low severity side effects, and medical cost.

In the past few decades, photodynamic therapy (PDT), a noninvasive method that is repeatable treatment without significant side effects, has received interest from many researchers worldwide in order to improve the effectiveness of PDT and offer various new photodynamic agents to clinically treat various cancer types (Carruth, 1998; Sibata, Colussi, Oleinick, and Kinsella, 2001; van Straten, Mashayekhi, de Bruijn, Oliveira, and Robinson, 2017). In principle, the photodynamic effect is based on the interaction between the light and photosensitizers (PSs) to generate reactive oxygen species (ROS) to kill the tumor cell, Figure 1.1. Singlet oxygen, often generated by organic PSs, is one of the ROS that serves as a signaling molecule to devastate the tumor by stimulating the apoptosis process, also known as programmed cell death (Triesscheijn, Baas, Schellens, and Stewart, 2006; van Straten et al., 2017). To date, researchers are still developing methods to improve the effectiveness of PDT. One possible way is to enhance the potential of PSs to be more highly tumor-specific with large amount of $^1O_2$ generation in deep tissue.
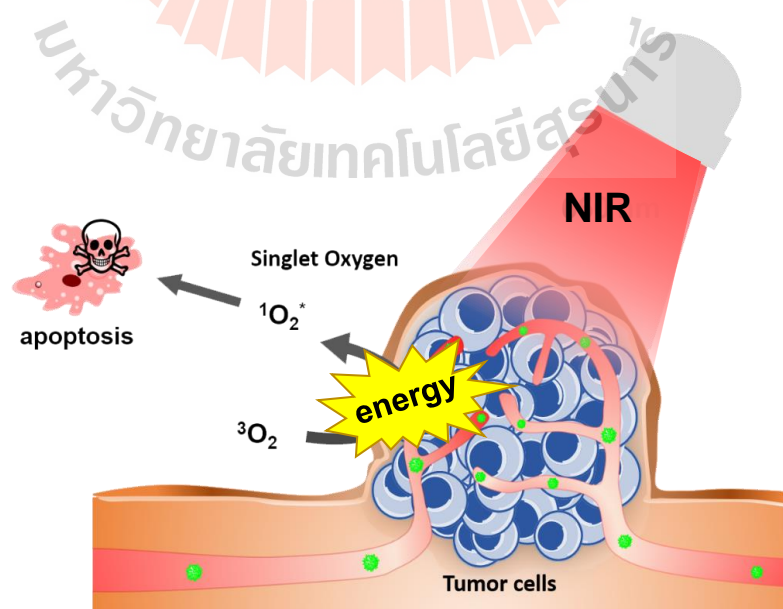
Figure 1.1 Photodynamic therapeutic process under NIR light irradiation.

Porphyrin and its derivatives have widely been utilized as PSs for PDT since they show strong absorption band in the red to NIR spectral region (650-800 nm). This optical window overlapping with the phototherapeutic window (650 – 850 nm) allows high singlet oxygen production during light irradiation, a key cytotoxic agent for devastating tumor cells (Ethirajan, Chen, Joshi, and Pandey, 2011; Hameed et al., 2018; Huang et al., 2019; Josefsen and Boyle, 2012). Most PSs, however, are less soluble in water or biological media owing to their naturally high hydrophobicity from the large π-extended system and have poor tumor homing's selectivity because of too small size (Bonnett, 1995; Wang et al., 2014). To overcome these limitations, nanoparticle engineering has allured researchers by benefiting from the enlarged particle size to increase tumor-targeting behavior via enhanced permeability and retention (EPR) effect and by altering PSs with hydrophilic bio-conjugated molecules: polymers, dendrimers, peptides, or lipids (Cheng, Wang, Feng, Yang, and Liu, 2014; Pandey et al., 2006).

Even though advanced progress in cancer treatment is now developed, serious side effects after treatment are still observed in patients who received a treatment for a long period. One major cause is long time accumulation of relatively large size and high hydrophobicity drugs inside the body which can be harmful to nearby normal tissues (Blanco, Shen, and Ferrari, 2015; Lux et al., 2011). In order to minimize this adverse effect, ultra-small nanoparticle is a dominant approach to minimize the severe long-term effect by rapidly eliminated out from the body via the renal pathway.

In addition, molecular imaging has become a promising tool to assist in the detection, diagnosis, and evaluation, depending on the unique properties of a material (Weissleder, 2006). There are many imaging techniques at the clinical level for

different purposes. Technically, all diagnostic imaging is aimed to track the material's biodistribution post-injection and visualize the internalization of tumors in the living system before PDT treatment (Bauerle, Komljenovic, and Semmler, 2012; Kircher and Willmann, 2012; Mahajan et al., 2015).

Herein, we proposed a nanostructure that offers fluorescence/photoacoustic double imaging-guided PDT characteristics. Briefly, pyropheophorbide-a (Pa) linked with amine polyethylene glycol (PEG), called Pa-PEG nanodots, were facile synthesized with ultra-small size (~2 nm). Proper surface modification tends to accumulate in tumors more than healthy tissues through the EPR effect. *In vivo* test demonstrated that Pa-PEG nanodots can effectively kill the solid tumor on xenograft mice after a high concentration of nanomaterials at the tumor site was exposed to 660 nm excitation light for PDT treatment. In addition to renal clearable behavior, fluorescent imaging showed that Pa-PEG nanodots were mostly eliminated out of the mice's body post-injection after 7-day. Thus, we demonstrate the combined approach of diagnostic and photodynamic therapeutic agent with high potential to be used for tumor devastation in further clinical treatment.

1.2 Research objectives

The ultimate goal of this thesis is to develop effective tumor-targeted PDT nanoprobes that enhance cancer therapy *in vitro* and *in vivo* as follows:

1.2.1 Synthesis and characterization of ultra-small nanomaterials. The aim of the materials syntheses is to find the easy and quick method to prepare the NPs, and this method should be reproducible with uniform particle size.

1.2.2 To visualize cancer cells using synthetic nanomaterials. This objective aims for the effective visualization of tumor cells. The materials should be able to label tumor cells and show high image contrast under the microscope.

1.2.3 To eliminate cancer cells using photodynamic therapy. This objective aims for effective tumor therapy, which can be done by *in vitro* PDT using our synthetic materials.

1.2.4 To determine the efficacy of the materials *in vivo*, including biodistribution, toxicity, targeted tumor imaging and therapy. This is the ultimate goal of this work since we are seeking for the best nanomedicine candidate for clinical translation.

1.2.5 To assess the long-term toxicity of the ultra-small nanomaterials. The purpose of the ultra-small diameter is to minimize long-term toxicity by taking the renal pathway of clearance from the body.

1.3 References

Bauerle, T., Komljenovic, D., and Semmler, W. (2012). Monitoring molecular, functional and morphologic aspects of bone metastases using non-invasive imaging. **Curr Pharm Biotechnol**. 13(4): 584-594.

Blanco, E., Shen, H., and Ferrari, M. (2015). Principles of nanoparticle design for overcoming biological barriers to drug delivery. **Nat Biotechnol**. 33: 941. doi:10.1038/nbt.3330.

Bonnett, R. (1995). Photosensitizers of the porphyrin and phthalocyanine series for photodynamic therapy. **Chem Soc Rev**. 24(1): 19-33. doi:10.1039/CS9952400 019.

Carruth, J. A. (1998). Clinical applications of photodynamic therapy. **Int J Clin Pract**. 52(1): 39-42.

Cheng, L., Wang, C., Feng, L., Yang, K., and Liu, Z. (2014). Functional nano-materials for phototherapies of cancer. **Chem Rev**. 114(21): 10869-10939. doi:10.1021/cr400532z.

Ethirajan, M., Chen, Y., Joshi, P., and Pandey, R. K. (2011). The role of porphyrin chemistry in tumor imaging and photodynamic therapy. **Chem Soc Rev**. 40(1): 340-362. doi:10.1039/b915149b.

Goldsmith, H. S. (1969). Clinical advances in the treatment of cancer. **Am J Surg**. 118(3): 368-376.

Hameed, S., Bhattarai, P., Liang, X., Zhang, N., Xu, Y., Chen, M., and Dai, Z. (2018). Self-assembly of porphyrin-grafted lipid into nanoparticles encapsulating doxorubicin for synergistic chemo-photodynamic therapy and fluorescence imaging. **Theranostics**. 8(19): 5501-5518. doi:10.7150/thno.27721.

Huang, Z., Wei, G., Zeng, Z., Huang, Y., Huang, L., Shen, Y., Sun, X., Xu, C., and Zhao, C. (2019). Enhanced cancer therapy through synergetic photodynamic/immune checkpoint blockade mediated by a liposomal conjugate comprised of porphyrin and IDO inhibitor. **Theranostics**. 9(19): 5542-5557. doi:10.7150/thno.35343.

Josefsen, L. B., and Boyle, R. W. (2012). Unique diagnostic and therapeutic roles of porphyrins and phthalocyanines in photodynamic therapy, imaging and theranostics. **Theranostics**. 2(9): 916-966. doi:10.7150/thno.4571.

Kircher, M. F., and Willmann, J. K. (2012). Molecular body imaging: MR imaging, CT, and US. part I. principles. **Radiology**. 263(3): 633-643. doi:10.1148/ radiol.12102394.

Lux, F., Mignot, A., Mowat, P., Louis, C., Dufort, S., Bernhard, C., Denat, F., Boschetti, F., Brunet, C., Antoine, R., Dugourd, P., Laurent, S., Elst, L. V., Muller, R., Sancey, L., et al. (2011). Ultrasmall rigid particles as multimodal probes for medical applications. **Angew Chem Int Edit**. 50(51): 12299-12303. doi:10.1002/anie.201104104.

Mahajan, A., Goh, V., Basu, S., Vaish, R., Weeks, A. J., Thakur, M. H., and Cook, G. J. (2015). Bench to bedside molecular functional imaging in translational cancer medicine: to image or to imagine? **Clin Radiol**. 70(10): 1060-1082. doi:10.1016/j.crad.2015.06.082.

Pandey, R. K., Goswami, L. N., Chen, Y., Gryshuk, A., Missert, J. R., Oseroff, A., and Dougherty, T. J. (2006). Nature: A rich source for developing multifunctional agents. tumor-imaging and photodynamic therapy. **Lasers Surg Med**. 38(5): 445-467. doi:10.1002/lsm.20352.

Petrelli, N. J., Winer, E. P., Brahmer, J., Dubey, S., Smith, S., Thomas, C., Vahdat, L. T., Obel, J., Vogelzang, N. บ Markman, M., Sweetenham, J. W., Pfister, D., Kris, M. G., Schuchter, L. M., Sawaya, R., et al. (2009). Clinical Cancer Advances 2009: major research advances in cancer treatment, prevention, and screening--a report from the American Society of Clinical Oncology. **J Clin Oncol**. 27(35): 6052-6069. doi:10.1200/JCO.2009.26.6171.

Sibata, C. H., Colussi, V. C., Oleinick, N. L., and Kinsella, T. J. (2001). Photodynamic therapy in oncology. **Expert Opin Pharmac**. 2(6): 917-927. doi:10.1517/14656566.2.6.917.

Triesscheijn, M., Baas, P., Schellens, J. H. M., and Stewart, F. A. (2006). Photodynamic therapy in oncology. **Oncologist**. 11(9): 1034-1044. doi:10.16 34/theoncologist.11-9-1034.

van Straten, D., Mashayekhi, V., de Bruijn, H. S., Oliveira, S., and Robinson, D. J. (2017). Oncologic Photodynamic Therapy: Basic principles, current clinical status and future directions. **Cancers**. 9(2): doi:10.3390/cancers9020019.

Wang, K.-K., Li, J., Kim, B.-J., Lee, J.-H., Shin, H.-W., Ko, S.-H., Lee, W.-Y., Lee, C.-H., Jung, S. H., Kim, Y.-R. (2014). Photophysical properties of pheophorbide-a derivatives and their photodynamic therapeutic effects on a tumor cell line *in vitro*. **Int J Photoenergy**. 7: doi:10.1155/2014/793723.

Weissleder, R. (2006). Molecular imaging in cancer. **Science**. 312(5777): 1168-1171. doi:10.1126/science.1125949.

WHO. (2018). Latest global cancer data: Cancer burden rises to 18.1 million new cases and 9.6 million cancer deaths in 2018 [Press release].

CHAPTER II

LITERATURE REVIEW

2.1 Nanoparticles in drug delivery

In the past decade, nanotechnology has emerged as a tool for molecular imaging and therapy with the goal of enhanced delivery efficacy, safety, and toxicological profiles and may eventually be used in humans for various purposes (Andreou, Pal, Rotter, Yang, and Kircher, 2 0 1 7 ; Gao, 2 0 1 3 ; Kim, Lee, and Hyeon, 2 0 1 7). Nanomaterials are suitable delivery vectors since they are small enough to cross vessel walls and cell membranes to interact with cells in the body (Cooper, Conder, and Harirforoosh, 2014). Moreover, nanoplatforms can be modified to exhibit proper physicochemical and biological features for *in vivo* use by choosing appropriate core materials and modifying their surface (Fang, Wan, Chu, Zhang, and Wu, 2 0 1 5). Targeted drug delivery and multifunctional nanomaterials for diagnosis and therapy have received much attention in nanomedicine. However, there are two major concerns including possible toxicity and uncertainty of biological behaviors of nanomaterials, which restrict their clinical translation (Sajid et al., 2015; Zoroddu et al., 2014). There are numbers of engineered materials that have proper molecular targets and no cytotoxicity *in vitro*; however, *in vivo* distribution, metabolism, and excretion are much more complex and become a bottleneck to entering clinical trials. Until now, more than 200 nanomedicine products are in clinical trials; yet, the success of NPs as clinical therapeutics is still uncertain (Min, Caster, Eblan, and Wang, 2015).

2.2 Photochemical mechanism

In 1900, the photodynamic therapy (PDT) concept was accidentally discovered by a medical student, Oscar Raab, in Munich, Germany. He found that micro-organisms surrounded a certain photosensitizer (PS) were destroyed during light exposure, but the micro-organisms were still remained healthy in the dark environment. However, the PDT concept became more popular in the 1970s in the USA for cancer remedy (Moan and Peng, 2002).
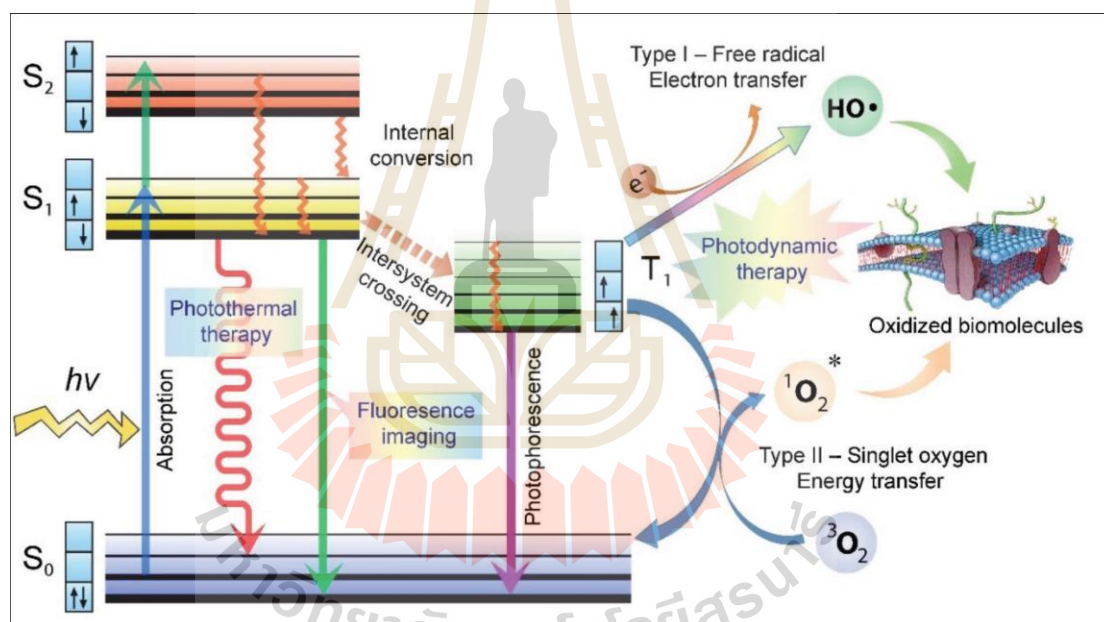
Figure 2.1 Possible transition related to phototherapeutic processes in Jablonski diagram. For photodynamic therapy, after excitation, electron transition from $S_1{\rightarrow}T_1$ takes advantage to the generation of singlet oxygen by molecular oxygen's energy harvesting (Type II). Copyright © 2016 American Chemical Society (Kamkaew, Chen, Zhan, Majewski, and Cai, 2016).

The PDT mechanism initially occurs when an electron of a PS molecule in the ground state (S_0) is promoted to a higher-energy singlet excited state (S_1) by absorbing appropriate energy from light at specific wavelengths. In the singlet excited state, a high energy electron of PS is unstable with a need to release its extra energy (Abrahamse and Hamblin, 2016). As shown in Figure 2.1, there are many directions for relaxing to more stable state (i) via radiative transition in light form (fluorescence), (ii) via non-radiative transition in heat form (internal conversion), and (iii) via transformation of electron pair in the singlet excited state to the triplet excited state (T_1) with parallel spins (intersystem crossing) and then release its energy in light form (phosphorescence) (Jaffe and Miller, 1966). Table 2.1 shows the comparison of the absorption and emission rates of fluorescence and phosphorescence: the absorption rate is prompt occurrence after excitation, fluorescence is slower emission rate, the moving from S_1 to T_1 is relatively required more time, and phosphorescence is the most sluggish transition to stable state due to a tiny probability of occurring (Harris and Bertolucci, 1978).

Table 2.1 Average time scale for radiative and nonradiative processes.

Transition	Time Scale	Radiative Process
Internal Conversion	$10^{-14} - 10^{-11}$ s	No
Vibrational Relaxation	$10^{-14} - 10^{-11}$ s	No
Absorption	10^{-15} s	Yes
Intersystem Crossing	$10^{-8} - 10^{-3}$ s	No
Phosphorescence	$10^{-4} - 10^{-1}$ s	Yes
Fluorescence	$10^{-9} - 10^{-7}$ s	Yes

Even though the transition of $S_1 \rightarrow T_1$ is forbidden according to selection rule, however, intersystem crossing between S_1 and T_1 can be weakly allowed by overlapping of the energy level of both states and able to compete with fluorescence transition. Moreover, the forbidden transition of $T_1 \rightarrow S_0$ provides a long lifetime electron struggling in the triplet excited state. This situation plays an essential role to induce PDT effect that typical oxygen molecule in biological media has sufficient time to harvest excess energy at the triplet excited state. The energy-transfer from T_1 to oxygen molecule leads to the production of singlet oxygen, which is called type II photochemical process. A Type I photochemical mechanism is related to an electron transfer reaction to produce the hydroxyl radical (OH$^\bullet$), which is the potential oxidant to damage most types of biomolecules. Despite that, researchers believe that most PSs take Type II reaction for tackling-cancer PDT (Agostinis et al., 2011; Carruth, 1998; Dolmans, Fukumura, and Jain, 2003).

2.3 Reactive oxygen species and apoptosis

Reactive oxygen species (ROS) in the biological system play a crucial role in the various biological process depending on the dose. ROS include superoxide radicals ($O_2^{\bullet-}$), hydrogen peroxide (H_2O_2), hydroxy radical (OH$^\bullet$), and singlet oxygen ($^1O_2$) (Halliwell, 2011). At low to moderate doses, ROS regulates many common physiological functions related to cell development, for instance, cell division, differentiation, migration, and cell death. In addition to the implication in signaling molecule, ROS leads to the activation of various cellular pathways and transcription factors resulting in cell survival or cell death processes such as autophagy and apoptosis, that regularly happen in organisms (Covarrubias, Hernandez, Schnabel,

Salas-Vidal, and Castro-Obregon, 2008). At the concentrated dose, however, ROS can induce oxidative stress causing uncontrollable oxidative damage to biomolecules, membranes, and organelles such as mitochondria (Halliwell, 2011).

Although advanced researches support the involvement of ROS with therapeutic purposes, the mechanism of actions of ROS-mediated apoptosis are not fully-characterized. Nonetheless, singlet oxygen is widely considered to induce apoptosis for tumor cells destroying during photodynamic therapy (Abrahamse and Hamblin, 2016). The apoptosis process is activated by three main signaling pathways including mitochondrial pathway, death receptor pathway, and endoplasmic reticulum pathway, which are relevant to both extrinsic and intrinsic pathways. In this review, only mitochondrial pathway, the most important pathway, is provided.

2.3.1 Mitochondrial pathway

Mitochondria are made of two membranes, which are vital organelles that play a crucial function as cellular energy (ATP) production via oxidative phosphorylation (Youle and Bliek, 2012). Importantly, mitochondria are responsible for the apoptosis regulation (Orrenius, Gogvadze, and Zhivotovsky, 2015).

Under the stressful conditions, movement across of molecular size less than 1.5 kDa, including proton, via the mitochondrial permeability transition (MPT) pore into the inner membrane is increased, disrupting oxidative phosphorylation (Halestrap, 2009). Intrinsic ROS trigger oxidation of cardiolipin leading to the increased outer mitochondrial membrane permeabilization (MOMP) that cause significant loss of cytochrome c (Cyt c) and also apoptosis-inducing factors (AIF) including endonuclease G (Endo G) and second mitochondria-derived activator of

caspases/direct inhibitor of apoptosis (IAP)-binding protein with low pI (Smac/Diablo), via Bax/Bak channels into the cytosol (Circu and Aw, 2010; Orrenius et al., 2015). Cytochrome c in the existence of dATP, then, forms the apoptosome together with apoptosis activating factor-1 (Apaf-1) and procaspase-9 resulting in self-activation of caspase-9 which can trigger caspases-3, -6, and -7 for protein destruction and apoptosis initiation (Orrenius et al., 2015). While released Smac/Diablo can deactivate the inhibitor of apoptosis proteins (IAP) in the cytosol in order to stop the functioning of anti-apoptosis. In the same situation, AIF and Endo G target the nucleus for DNA fragmentation (Bettaieb and Averill-Bates, 2015). Moreover, DNA damage by ROS can be found in the mitochondria matrix. Considering anti-apoptotic Bcl-2 and Bcl-XL proteins at the outer mitochondrial membrane after ROS activate p53 and/or c-Jun N-terminal kinase (JNK), the apoptosis process is initiated by the stimulation of JNK to pro-apoptotic Bax, Bim, Bak, and Bad proteins. This stimulation brings the pro-apoptotic proteins to form heterodimers with anti-apoptotic Bcl-2 and Bcl-XL proteins, suspending the working of anti-apoptotic proteins, Figure 2.2 (Orrenius et al., 2015; West and Marnett, 2006).
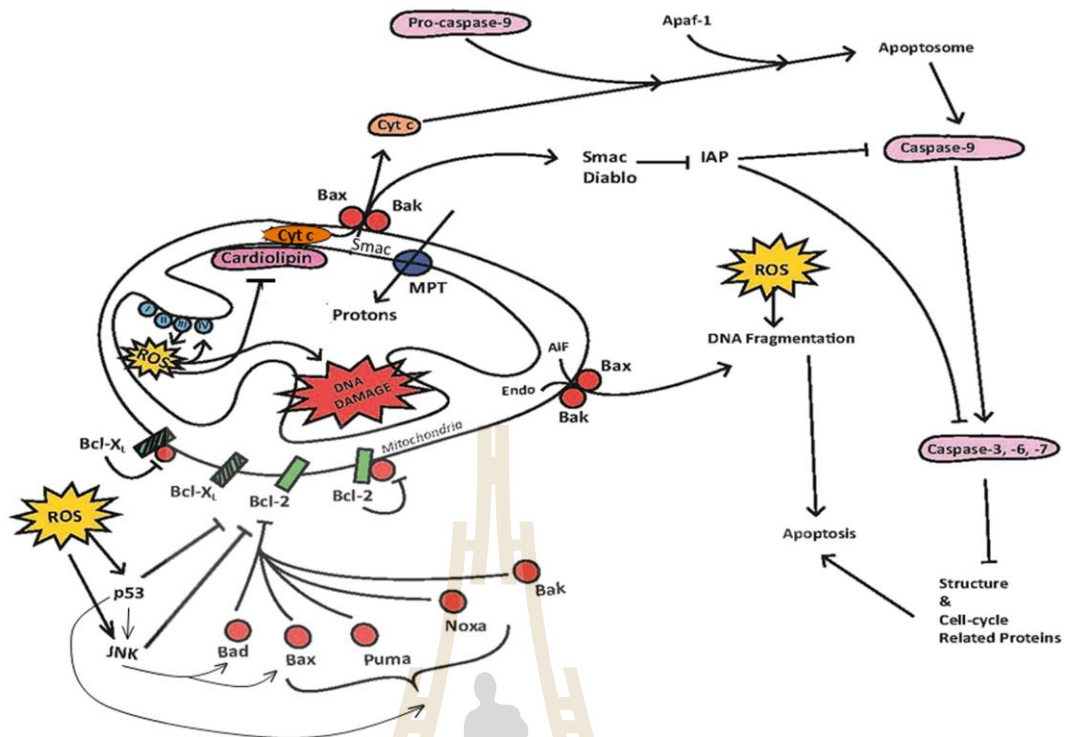
Figure 2.2 Activation of the mitochondrial (intrinsic) pathway of apoptosis by ROS. The promotion of ROS leads to activate caspase-9 for apoptosis induction and to trigger DNA fragmentation. Copyright © 2016 Elsevier B.V. (Redza-Dutordoir and Averill-Bates, 2016).

2.3.2 Apoptosis process

In the adult human, 50-70 billion cells are auto-disrupted each day by apoptosis, or programmed cell death, to maintaining the cell population for effective functioning: normal cell turnover, proper development, processing of the immune system, or chemical-induced cell death (Cole and Kramer, 2016). In healthy conditions, the division rate and death rate are steady in order to regulate homeostasis; nonetheless, a disorder of equilibrium leads to abnormal states. A tumor can be

generated if the division rate is more rapid, or cell processing is inefficient if the division rate is lower than the death rate.

Apoptosis is regulated by both intrinsic and extrinsic signaling pathways. After the activation, there are three common response steps to cell damage, Figure 2.3 (Abou-Ghali and Stiban, 2015).

1. The cell starts to shrink, and chromatin begins to condense.

2. The apoptotic cell forms bleb for becoming fragmented, nucleus split into small pieces, DNA breaks apart.

3. Membrane blebbing becomes debris, called apoptotic bodies, which contain compacted organelles.

To clean the dead cells, apoptotic bodies are detected by macrophages removing the dead fragments from the body.
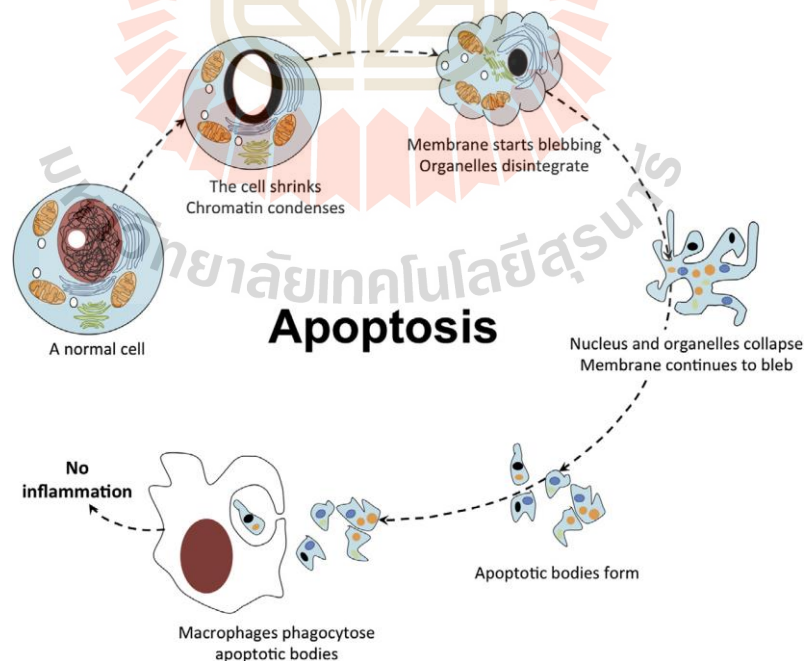
Figure 2.3 Cytology of apoptosis at the different stages after apoptosis activation. Copyright © 2015 Elsevier B.V. (Abou-Ghali and Stiban, 2015).

2.4 Ideal photosensitizer properties

Most of PSs that absorb light in the red to deep red region (600-800 nm), known as therapeutic window, can effectively induce photodynamic therapeutic effect to ruin cancer cells in deep tissue (Kwiatkowski et al., 2018). In this region, biological substances in living media have low light absorption, therefore, the excitation light can penetrate deeper in the tissue to activate PSs with high light dose, Figure 2.4 (Teraphongphom, Kong, Warram, and Rosenthal, 2017).
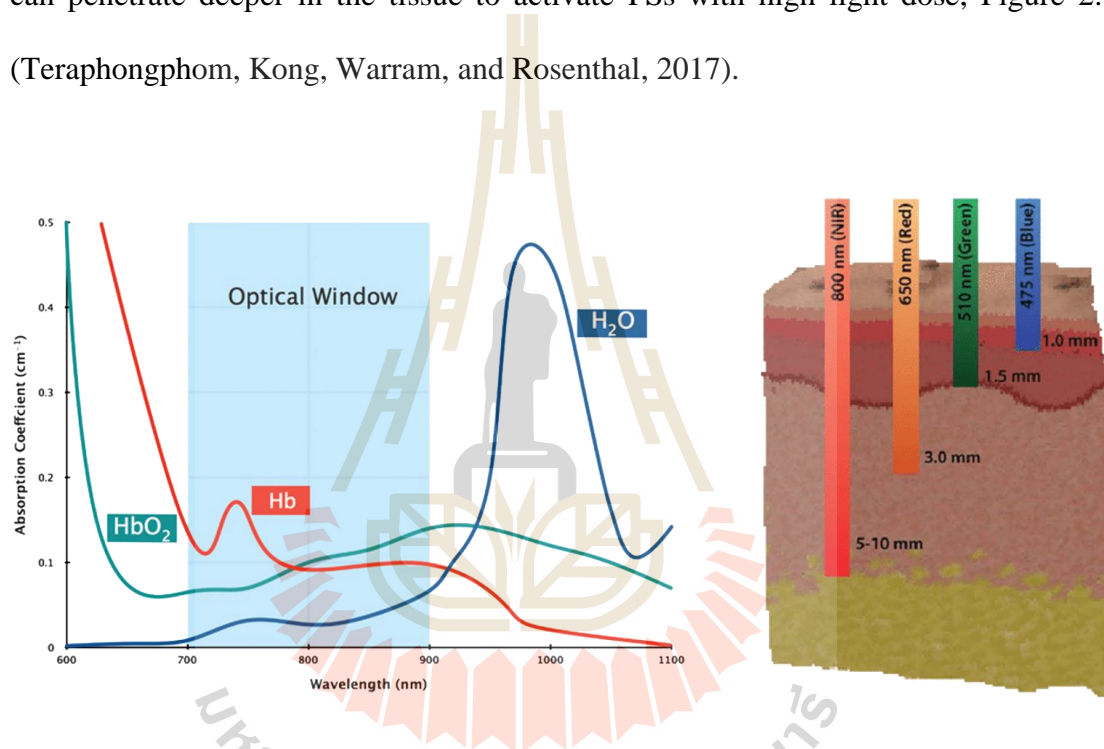
Figure 2.4 Optical window and penetrability of NIR light (a) NIR window is optimal for *in vivo* imaging due to minimal light absorption by hemoglobin (Hb), oxyhemoglobin (HbO$_2$), and water in tissues from 700 to 900 nm. Copyright Macmillan Publishers Ltd. (Phan and Bullen, 2010) and (b) Near infrared (NIR) light has the best penetration depth through soft-tissue. Copyright © 2017 Wiley Periodicals, Inc. (Teraphongphom et al., 2017).

To obtain high PDT effect, the qualifications of photosensitizers should be as follows:

- High chemical purity grade.

- Stable at a comfortable ambient temperature.

- Great photosensitive on a specific wavelength.

- Outstanding photochemical reactivity; the maximum absorbance in Q band should be between 600-800 nm.

- Minimal absorption in Soret band (400-600 nm). This minimizes the absorption caused by sunlight and prevent self-decomposition or photobleaching.

- The absorption in red to deep red region should be prominent over that of other endogenous dye in the body, such as melatonin, hemoglobin, or oxyhemoglobin.

- Diminutive cytotoxicity in the dark environment.

- Miscible with biological media in the body.

- High selectivity for neoplastic tissues: the photosensitizer should be retained at the affected areas for a while with slow leaking out for effective therapy, and should not accumulate at healthy cells to avoid the phototoxic side effects.

- Inexpensive and facile synthesis (Agostinis et al., 2011; Kou, Dou, and Yang, 2017; Nyman and Hynninen, 2004)

2.5 Photosensitizer-based nanoparticle delivery

Modern photodynamic therapy has started since 1970 by Thomas Dougherty at Roswell Park Cancer Institute in Buffalo, NY, however, advanced nanotechnology has just developed in the past decade (Abrahamse and Hamblin, 2016). The combination of PSs with nanomaterials is an attractive way to enhance PDT efficacy and emerged as a nanoplatform for diagnostic and therapeutic purposes with great targeting ability, called nanomedicine (Frimberger, Moore, Cincotta, Cotter, and Foley, 1998; Morley et al., 2012; Verma et al., 2009). Several techniques have been used to provide organic-based, inorganic based, or biomolecular-based photosensitizers for nanomaterial formation including encapsulation, functionalization and immobilization by non-covalent interactions. Most photosensitizers, however, have high hydrophobicity owing to their large conjugated system tending to form an aggregate in an aqueous media which blocks the PDT effect. In order to raise the PDT effect, PSs are required to be a monomeric form (Xu et al., 2014). One of the popular ways to separate them into an individual molecule is the conjugation between the well-match functional group on hydrophilic polymer and on PSs (Gross, Gilead, Scherz, Neeman, and Salomon, 2003).

Currently, there are many FDA-approved nanomedicines assemble polyethylene glycol (PEG) for both imaging and therapeutic purposes due to its stability, nanosized offering, and biodegradable ability (Davis et al., 2010; Jacobson et al., 2010; Keren et al., 2008; Lim et al., 2010; O'Brien et al., 2004; Wagner, Dullaart, Bock, and Zweck, 2006). The introduction of hydrophilic PEG into a peripheral functional group on PS surface, known as PEGylation, can form nanoparticle through self-assembly for drug delivery. PEGylated PSs have been vastly explored their behavior affecting on *in vivo*

application for cancer treatment. The hydrophilic PEG chain prevents the aggregate of hydrophobic PSs, enabling effective PDT to kill malignant cells. It was reported that nanoparticles from PEGylation could prolong circulation time in the bloodstream and have high targeting ability via the enhance permeability and retention (EPR) effect (Aliabadi and Lavasanifar, 2006; Kanaras, Kamounah, Schaumburg, Kiely, and Brust, 2002; H. Maeda, Wu, Sawa, Matsumura, and Hori, 2000). High concentration of nanoparticles at the tumor accumulated by EPR effect demonstrates a great contrast signal at tumor area against the background during imaging, offering a potential ability to serve as a promising agent for locating the tumor site (Gref et al., 1994). Moreover, the PEG polymer-coated PSs reduce the uptake by the reticuloendothelial system (RES), such as the liver and spleen, by decreasing serum protein absorption. The interaction reduction with serum protein allows the NPs circulate in the blood vessels for further accumulation at the tumor bed (Owens and Peppas, 2006; Saba, 1970).

Porphyrin and its derivatives are extensively used as PSs in PDT since they are not toxic to organs, possess red to deep red absorption, and can produce singlet oxygen, which is a key cytotoxic agent for tumor devastation (Ethirajan, Chen, Joshi, and Pandey, 2011; Hameed et al., 2018; Z. Huang et al., 2019; Josefsen and Boyle, 2012; Sun et al., 2019). Chlorophyll-a and its derivatives are one of the families containing a large π conjugation system of porphyrin structure, which provides strong absorption in the 300-700 nm region. Pyropheophorbide-a (Pa) is a molecule derived from chlorophyll-a. Currently, many Pa-conjugated nanomaterials have been reported as effective PDT agents *in vitro* and *in vivo* (Chen et al., 2005; Helmreich et al., 2005; Ng, Lovell, Vedadi, Hajian, and Zheng, 2013; Rancan et al., 2007; Tan et al., 2016;

Zhou, Wei, Wu, Chen, and Xing, 2012). Rapozzi et al. reported the effect of PEGylation on the photosensitizer (pheophorbide-a) biodistribution. (Rapozzi et al., 2010). The results showed that the nanomaterials (mPEG-Pba) could be distributed to a whole body with a higher amount of photosensitizer in the tumor compared to free Pba. However, the authors did not study the PDT effect of the prepared NPs in this work. In other works, PEGylation of photosensitizers (Pba and Ce6) exhibited efficient intracellular uptake and phototoxicity *in vitro* for cancer treatment. Yet, *in vivo* studies were not reported in these works. However, the relatively large diameter of these nanomaterials led to the prolonged retention in RES organs, resulting in poor clearance from the body due to the sluggish excretion via hepatocyte (Blanco, Shen, and Ferrari, 2015; Lux et al., 2011). Hence, the long-retention period of those nanomaterials can cause long-term effects (e.g., potential toxicity) that restrict their clinical translation.

Notably, ultra-small nanoparticles with a size less than 6-8 nm can pass through the glomerular capillary of kidney filtration to enable faster elimination from the body via renal partway compared to hepatobiliary excretion (Choi et al., 2007; X. Huang et al., 2013; Shen et al., 2017; Tang et al., 2016). Moreover, there are some reported nanoparticles with the size between 1-20 nm containing negative charge on the surface tend to have renal excretable properties (Du, Yu, and Zheng, 2018). To balance tumor retention ability and renal eliminable behavior for reducing long-term effects, it is a great interest to explore renal-clearable nanomaterials containing imaging-guided and therapeutic properties for cancer therapy.

2.6 Tumor-Targeting in PDT *in vivo*

Synthetic nanoparticles for biomedical applications in cancer diagnosis and therapy have been studied their qualifications in both *in vitro* and *in vivo* assays for achieving the prospective goal of cancer treatment in the research scale. One of the most crucial information provided by an *in vivo* experiment is an optimal time for applying therapy. While *in vitro* assays are necessary for investigating the nanomaterial interaction at the cellular level. Tumor-bearing mice have been used as a model for elucidating the appropriate time post-injection, which relies on targeting ability of each nanomedicine. There are two practical ways for drug delivery to introduce the nanomaterials into the solid tumors, including (i) active targeting involving the conjugation of targeting ligand that matches with the overexpressed receptors on tumor and (ii) passive targeting involving the benefit of EPR effect, Figure 2.5 (Chinen et al., 2015; Sinha, Kim, Nie, and Shin, 2006). However, this literature review is focused on passive targeting for cancer diagnosis.
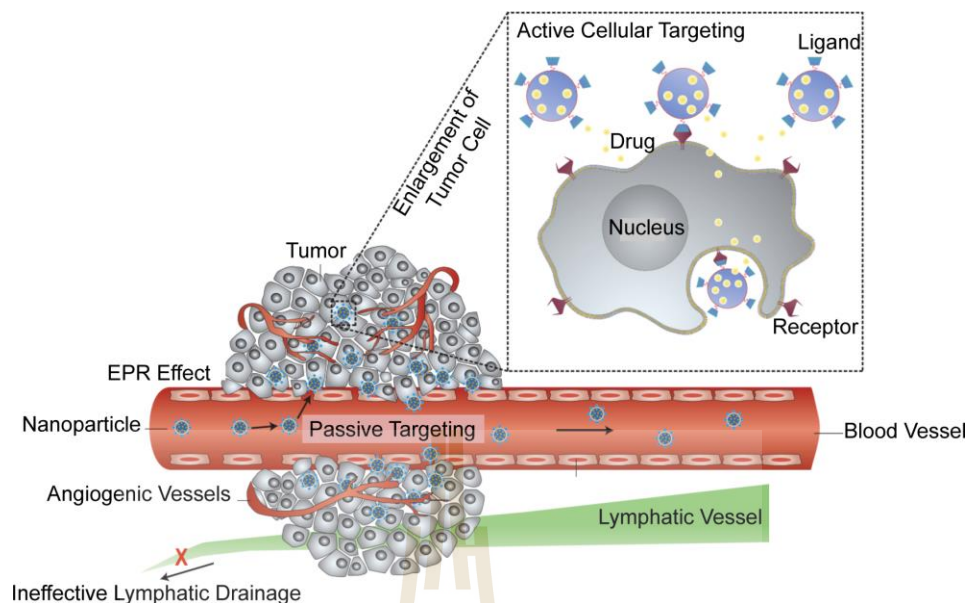
Figure 2.5 Diagram depicting the enhanced permeability and retention effect (Peer et al., 2007). Copyright © 2007 Macmillan Publishers Ltd.

Passive targeting allows circulated nanomaterials in the bloodstream with a diameter not larger than 150 nm passes through the leakage blood vessels into the cancer tissue (Bertrand, Wu, Xu, Kamaly, and Farokhzad, 2013; Cho, Wang, Nie, Chen, and Shin, 2008; Danhier, Feron, and Preat, 2010). In the presence of tumor cells, Figure 2.5, rapid vascularization is built to provide sufficient nutrient consumption for serving the fast-growing up of tumor tissue, and this rapid forming of blood vessels causes disorderly arrangement of endothelial cells resulting in defective vascular structure. Hence, nanomaterials that smaller than pore structure on blood vessel can move out the blood circulation system via the leaky vasculatures, enhancing permeability and retention of nanomaterials (Frank et al., 2014; Hiroshi Maeda, 2015; H. Maeda et al., 2000; Prabhakar et al., 2013). In addition, tumor tissues are meager lymphatic drainage allowing longer retention time in solid tumors

with poor elimination by lymphatic system (Frank et al., 2014; H. Maeda et al., 2000; Peer et al., 2007). Nanomaterials that passively extravasate from the blood circulation system and stuck within a tumor area are identified as the enhanced permeability and retention effect or EPR effect. As a result of the EPR effect, nanomedicines can internalize in tumor bed 10-100 times higher than the introduction of free PSs (Sinha et al., 2006).

2.7 Molecular imaging techniques

The opacity of the human body is one of the problems for disease diagnosis. Formerly, surgery was unavoidable in treating a disease leading to pain and wounds. However, in the present time, noninvasive techniques have been developed to assist diagnosis in several diseases, such as magnetic resonance imaging, near-infrared imaging, positron emission tomography, single-photon positron emission tomography, computed tomography, and optical imaging (Fass, 2008; Lu and Yuan, 2015).

In principle, most of the biomedical imaging techniques involve electromagnetic interaction of a contrast agent that is introduced into the tissue, after which computer processing will generate anatomical images to evaluate the activity changes in the body, which is important in tumor diagnosis. Imaging techniques are qualified as powerful tools for cancer diagnosis and have several advantages, including being noninvasive, allowing real-time monitoring, and being nondestructive to surrounding tissues, which help with therapeutic planning and injury reduction.

2.7.1 Fluorescent imaging

Near-infrared (NIR) imaging is one direct method of optical imaging for real-time quantitative analysis. This method is a combination of NIR spectroscopy and digital imaging processing, to create a cross-sectional photo of tissues for powerful tumor diagnosis based on fluorescent light emitted from triggered loaded fluorescence dyes. The NIR imaging system consists of an excitation source, imaging optic, monochromator, and a focal plane array (FPA) as an image sensing detector, Figure 2.6. In principle, upon excitation, the absorbed dyes within living tissues will emit the signal at a longer wavelength to an imaging optic, and the specific wavelength will be selected before reaching the FPA detector, the results of cross-sectional 2D or 3D images of tissue are obtained after signal processing. Furthermore, NIR imaging has high sensitivity and resolution and is inexpensive, nondestructive to living organisms, none of high energy ray radiation, and relatively low cost (Frangioni, 2003; Luo, Zhang, Su, Cheng, and Shi, 2011).
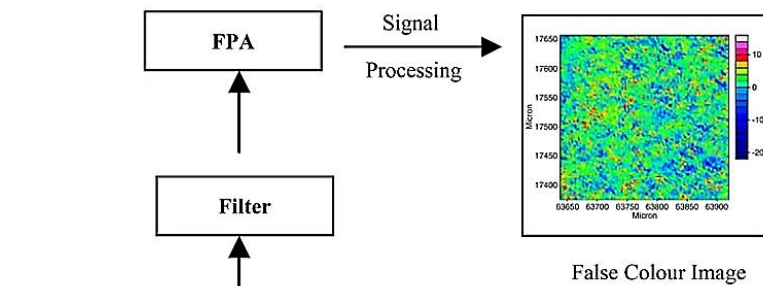
Figure 2.6 Basic configuration of a near-infrared imaging system. Copyright © 2005 Elsevier B.V. (Reich, 2005).

2.7.2 Photoacoustic imaging

Photoacoustic (PA) imaging is noninvasive imaging technique that recently developed for imaging-guided therapy. The formation of a photoacoustic signal is based on the NIR excitation of PSs to generate the photoacoustic effect. The interaction between periodical pulsed NIR laser (pulse duration < 10 ns) and PSs causes rapid heat generation after light absorption leading to the thermal expansion, which induces the change of pressure around the tumor biome. This pressure change initiates the formation of sound waves, known as acoustic waves, which are detected by measuring the formed sound waves with ultrasound (US) detector before signal processing to build an image and show on a computer screen, Figure 2.7 (Attia et al.,

2019; Lengenfelder et al., 2019; Wang and Hu, 2012). In addition, PA imaging is a useful technique accompanied with high sensitivity and high spatial resolution for deep-seated tumor visualization due to the advantage of NIR laser (700-900 nm) that can deeply penetrate through the skin.

| laser pulse | → | absorption | → | thermal expansion | → | acoustic waves | → | ultrasound detection | → | image formation |
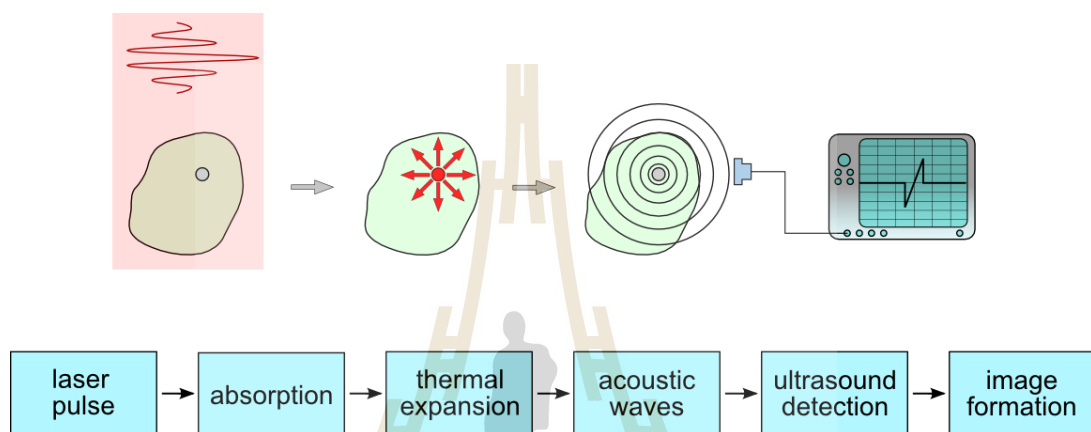
Figure 2.7 Basic principle of a photoacoustic imaging system. Copyright © 1997-2020, Global Information, Inc. (Johnson, 2018)

Compared to PA, fluorescence (FL) imaging offers higher resolution and greater sensitivity, whereas it has poor spatial resolution due to the limitation of light penetration ability (Ge et al., 2015; Jing et al., 2014; Moore and Jokerst, 2019). Therefore, combining FL and PA imaging modalities in a single particle may overcome the limitation of these two imaging techniques, which enhance imaging resolution and improve its sensitivity for tracking the accumulation of nanomaterials (Yang and Chen, 2019).

2.8 The reduction of long-term toxicity

An engineered nanoparticle nowadays serves as a powerful tool to realize tumor imaging and therapy in both research scale and clinical translation (Jiang et al., 2017; Moghimi and Szebeni, 2003; Walkey, Olsen, Guo, Emili, and Chan, 2012; Yu et al., 2017; Zhang, Poon, Tavares, McGilvray, and Chan, 2016). However, an administration of nanomedicine into the body can cause high uptake by the reticuloendothelial system (RES), leading to slow elimination in feces and raise the long-term effect to patients (Blanco et al., 2015; Lux et al., 2011). On the other clearable process, the kidneys are also play a pivotal role for nanomaterial clearance. Glomerular filtration membrane (GBM) in the kidneys has pores with sizes of 2-8 nm, and podocytes are ordered in a monolayer with gaps of 4-11 nm. These layers are size-selective glomerular membrane, which only allows the nanomaterials with diameter 2-8 nm to move across the GBM, Figure 2.8 (Du et al., 2018). In order to reduce to the potential side effect, preparing nanoparticles with a size less than 8 nm is an attractive way to conquer this drawback since they are small enough to pass through the GBM of kidneys for disposing of urine-contained nanomedicines. Thus, there is a significant demand to prepare ultra-small theranostic agents with renal excretable behaviors.
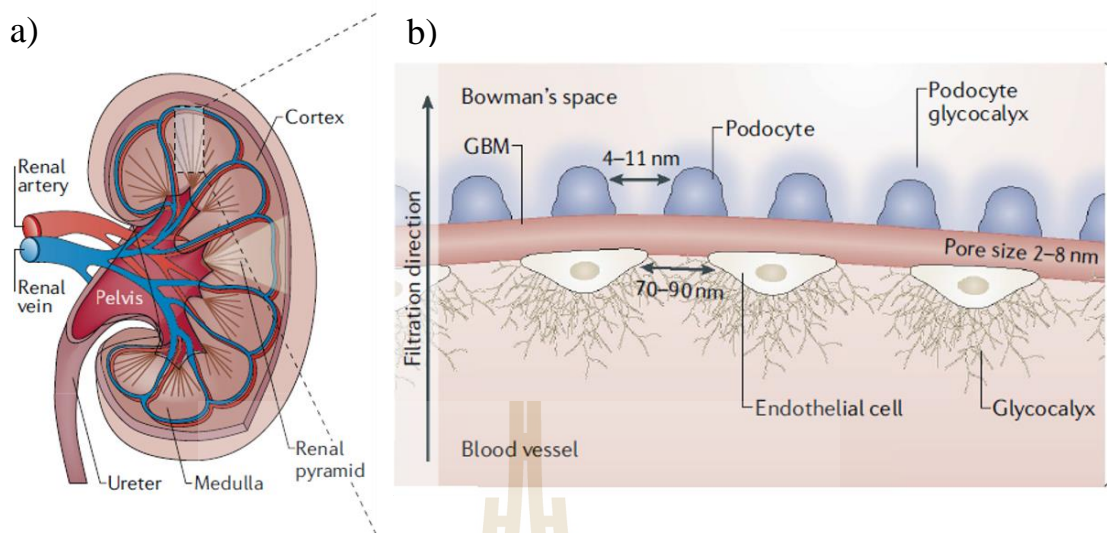
Figure 2.8 Anatomy of kidney (a) The blood introduces to the renal artery and flow out through the renal vein allowing the filtration at the glomerular membrane. (b) The glomerular filtration membrane structure offers the size- selective nanoparticles in sizes 2-8 nm. Copyright © 2018, Springer Nature (Du et al., 2018)

2.9 References

Abou-Ghali, M., and Stiban, J. (2015). Regulation of ceramide channel formation and disassembly: Insights on the initiation of apoptosis. **Saudi J Biol Sci**. 22(6): 760-772. doi:10.1016/j.sjbs.2015.03.005.

Abrahamse, H., and Hamblin, Michael R. (2016). New photosensitizers for photodynamic therapy. **Biochem J**. 473(4): 347-364. doi:10.1042/bj2015 0942.

Agostinis, P., Berg, K., Cengel, K. A., Foster, T. H., Girotti, A. W., Gollnick, S. O., Hahn, Stephen M. Hamblin, Michael R., Juzeniene, A., Kessel, D., Korbelik, M., Moan, J., Mroz, P., Nowis, D., Piette, J., et al. (2011). Photodynamic

therapy of cancer: An update. **CA-Cancer J Clin**. 61(4): 250-281. doi:10.3 322/caac.20114.

Aliabadi, H. M., and Lavasanifar, A. (2006). Polymeric micelles for drug delivery. **Expert Opin Drug Del**. 3(1): 139-162. doi:10.1517/17425247.3.1.139.

Andreou, C., Pal, S., Rotter, L., Yang, J., and Kircher, M. F. (2017). Molecular Imaging in Nanotechnology and Theranostics. **Mol Imaging Biol**. 19(3): 363-372. doi:10.1007/s11307-017-1056-z.

Attia, A. B. E., Balasundaram, G., Moothanchery, M., Dinish, U. S., Bi, R., Ntziachristos, V., and Olivo, M. (2019). A review of clinical photoacoustic imaging: Current and future trends. **Photoacoustics**. 16: 100144. doi:10.1 016/j.pacs.2019.100144.

Bertrand, N., Wu, J., Xu, X., Kamaly, N., and Farokhzad, O. (2013). Cancer Nanotechnology: The impact of passive and active targeting in the era of modern cancer biology. **Adv Drug Deliver Rev**. 66: doi:10.1016/j.addr.201 3.11.009.

Bettaieb, A., and Averill-Bates, D. A. (2015). Thermotolerance induced at a mild temperature of 40°C alleviates heat shock-induced ER stress and apoptosis in HeLa cells. **Biochim Biophys Acta**. 1853(1): 52-62. doi:10.1016/j.bbamcr. 2014.09.016.

Blanco, E., Shen, H., and Ferrari, M. (2015). Principles of nanoparticle design for overcoming biological barriers to drug delivery. **Nat Biotechnol**. 33: 941. doi:10.1038/nbt.3330.

Carruth, J. A. (1998). Clinical applications of photodynamic therapy. **Int J Clin Pract**. 52(1): 39-42.

Chen, Y., Zheng, X., Dobhal, M. P., Gryshuk, A., Morgan, J., Dougherty, T. J., Oseroff, A., and Pandey, R. K. (2005). Methyl Pyropheophorbide-a Analogues: Potential fluorescent probes for the peripheral-type benzodiazepine receptor. Effect of central metal in photosensitizing efficacy. **J Med Chem**. 48(11): 3692-3695. doi:10.1021/jm050039k.

Chinen, A. B., Guan, C. M., Ferrer, J. R., Barnaby, S. N., Merkel, T. J., and Mirkin, C. A. (2015). Nanoparticle probes for the detection of cancer biomarkers, cells, and tissues by fluorescence. **Chem Rev**. 115(19): 10530-10574. doi:1 0.1021/acs.chemrev.5b00321.

Cho, K., Wang, X., Nie, S., Chen, Z., and Shin, D. (2008). Therapeutic nanoparticles for drug delivery in cancer. **Clin Cancer Res**. 14: 1310-1316. doi:10.1158/ 1078-0432.CCR-07-1441.

Choi, H. S., Liu, W., Misra, P., Tanaka, E., Zimmer, J. P., Itty Ipe, B., Bawendi, M., and Frangioni, J. V. (2007). Renal clearance of quantum dots. **Nat Biotechnol**. 25(10): 1165-1170. doi:10.1038/nbt1340.

Circu, M. L., and Aw, T. Y. (2010). Reactive oxygen species, cellular redox systems, and apoptosis. **Free Radical Bio Med**. 48(6): 749-762. doi:10.1016/j.freerad biomed.2009.12.022.

Cole, L., and Kramer, P. R. (2016). Chapter 2.3 - Apoptosis, growth, and aging. In L. Cole and P. R. Kramer (Eds.). **Human Physiology, Biochemistry and Basic Medicine**. (pp. 63-66). Boston: Academic Press.

Cooper, D. L., Conder, C. M., and Harirforoosh, S. (2014). Nanoparticles in drug delivery: mechanism of action, formulation and clinical application towards

reduction in drug-associated nephrotoxicity. **Expert Opin Drug Del**. 11(10): 1661-1680. doi:10.1517/17425247.2014.938046.

Covarrubias, L., Hernandez, D., Schnabel, D., Salas-Vidal, E., and Castro-Obregon, S. (2008). Function of reactive oxygen species during animal development: Passive or active? **Dev Biol**. 320: 1-11. doi:10.1016/j.ydbio.2008.04.041.

Danhier, F., Feron, O., and Preat, V. (2010). To exploit the tumor microenvironment: Passive and active targeting of nanocarriers for anticancer drug delivery. **J Control Release**. 148: 135-146. doi:10.1016/j.jconrel.2010.08.027.

Davis, M. E., Zuckerman, J. E., Choi, C. H. J., Seligson, D., Tolcher, A., Alabi, C. A., Yen, Y., Heidel, J. D., and Ribas, A. (2010). Evidence of RNAi in humans from systemically administered siRNA via targeted nanoparticles. **Nature**. 464(7291): 1067-1070. doi:10.1038/nature08956.

Dolmans, D. E. J. G. J., Fukumura, D., and Jain, R. K. (2003). Photodynamic therapy for cancer. **Nat Rev Cancer**. 3: 380. doi:10.1038/nrc1071.

Du, B., Yu, M., and Zheng, J. (2018). Transport and interactions of nanoparticles in the kidneys. **Nat Rev Mater**. 3: 358-374. doi:10.1038/s41578-018-0038-3.

Ethirajan, M., Chen, Y., Joshi, P., and Pandey, R. K. (2011). The role of porphyrin chemistry in tumor imaging and photodynamic therapy. **Chem Soc Rev**. 40(1): 340-362. doi:10.1039/B915149B.

Fang, Z., Wan, L. Y., Chu, L. Y., Zhang, Y. Q., and Wu, J. F. (2015). 'Smart' nanoparticles as drug delivery systems for applications in tumor therapy. **Expert Opin Drug Delivery**. 12(12): 1943-1953. doi:10.1517/17425247. 2015.1071352.

Fass, L. (2008). Imaging and cancer: A review. **Mol Oncol**. 2(2): 115-152. doi:10.1 016/j.molonc.2008.04.001.

Frangioni, J. V. (2003). *In vivo* near-infrared fluorescence imaging. **Curr Opin Chem Biol**. 7(5): 626-634. doi:10.1016/j.cbpa.2003.08.007.

Frank, D., Tyagi, C., Tomar, L., Choonara, Y., du Toit, L., Kumar, P., Penny, C., and Pillay, V. (2014). Overview of the role of nanotechnological innovations in the detection and treatment of solid tumors. **Int J Nanomed**. 9: 589-613. doi:10.2147/IJN.S50941.

Frimberger, A., Moore, A., Cincotta, L., Cotter, S., and Foley, J. (1998). Photodynamic therapy of naturally occurring tumors in animals using novel benzophenothiazine photosensitizer. **Clin Cancer Res**. 4: 2207-2218.

Gao, X. (2013). Molecular imaging with multifunctional nanoparticles. **Clin Chem**. 59(10): 1532-1533. doi:10.1373/clinchem.2012.198200.

Ge, J., Jia, Q., Liu, W., Guo, L., Liu, Q., Lan, M., Zhang, H., Meng, X., and Wang, P. (2015). Red-emissive carbon dots for fluorescent, photoacoustic, and thermal theranostics in living mice. **Adv Mater**. 27(28): 4169-4177. doi:10.1002/adma .201500323.

Gref, R., Minamitake, Y., Peracchia, M. T., Trubetskoy, V. S., Torchilin, V. P., and Langer, R. (1994). Biodegradable long-circulating polymeric nanospheres. **Science**. 263: 1600-1603. doi:10.1126/science.8128245.

Gross, S., Gilead, A., Scherz, A., Neeman, M., and Salomon, Y. (2003). Monitoring photodynamic therapy of solid tumors online by BOLD-contrast MRI. **Nat Med**. 9(10): 1327-1331. doi:10.1038/nm940.

Halestrap, A. (2009). Halestrap AP.. What is the mitochondrial permeability transition pore?. **J Mol Cell Cardiol**. 46: 821-831. doi:10.1016/j.yjmcc.2009.02.021.

Halliwell, B. (2011). Free radicals and antioxidants—Quo vadis? **Trends Pharmacol Sci**. 32: 125-130. doi:10.1016/j.tips.2010.12.002.

Hameed, S., Bhattarai, P., Liang, X., Zhang, N., Xu, Y., Chen, M., and Dai, Z. (2018). Self-assembly of porphyrin-grafted lipid into nanoparticles encapsulating doxorubicin for synergistic chemo-photodynamic therapy and fluorescence imaging. **Theranostics**. 8(19): 5501-5518. doi:10.7150/thno.27721.

Harris, D. C., and Bertolucci, M. D. (1978). **Symmetry and spectroscopy: an introduction to vibrational and electronic spectroscopy**: Oxford University Press.

Helmreich, M., Ermilov, E. A., Meyer, M., Jux, N., Hirsch, A., and Röder, B. (2005). Dissipation of electronic excitation energy within a C_{60} [6:0]-hexaadduct carrying 12 pyropheophorbide a moieties. **J Am Chem Soc**. 127(23): 8376-8385. doi:10.1021/ja0503581.

Huang, X., Zhang, F., Zhu, L., Choi, K. Y., Guo, N., Guo, J., Tackett, K., Anilkumar, P., Liu, G., Quan, Q., Choi, H. S., Niu, G., Sun, Y.-P., Lee, S., and Chen, X. (2013). Effect of injection routes on the biodistribution, clearance, and tumor uptake of carbon dots. **ACS Nano**. 7(7): 5684-5693. doi:10.1021/nn401911k.

Huang, Z., Wei, G., Zeng, Z., Huang, Y., Huang, L., Shen, Y., Sun, X., Sun, X. Xu, C., and Zhao, C. (2019). Enhanced cancer therapy through synergetic photodynamic/immune checkpoint blockade mediated by a liposomal conjugate comprised of porphyrin and IDO inhibitor. **Theranostics**. 9(19): 5542-5557. doi:10.7150/thno.35343.

Jacobson, G. B., Gonzalez-Gonzalez, E., Spitler, R., Shinde, R., Leake, D., Kaspar, R. L., Contag, C. H., and Zare, R. N. (2010). Biodegradable nanoparticles with sustained release of functional siRNA in skin. **J Pharm Sci**. 99(10): 4261-4266. doi:10.1002/jps.22147.

Jaffe, H. H., and Miller, A. L. (1966). The fates of electronic excitation energy. **J Chem Educ**. 43(9): 469. doi:10.1021/ed043p469.

Jiang, W., Yuan, H., Chan, C., von Roemeling, C., Yan, Z., Weissman, I., and Kim, B. (2017). Lessons from immuno-oncology: A new era for cancer nanomedicine? **Nat Rev Drug Discov**. 16: doi:10.1038/nrd.2017.34.

Jing, L., Ding, K., Kershaw, S. V., Kempson, I. M., Rogach, A. L., and Gao, M. (2014). Magnetically engineered semiconductor quantum dots as multimodal imaging probes. **Adv Mater**. 26(37): 6367-6386. doi:10.1002/adma.2014022 96.

Johnson, J. (2018). **Global photoacoustic imaging market research report 2018**.

Josefsen, L. B., and Boyle, R. W. (2012). Unique diagnostic and therapeutic roles of porphyrins and phthalocyanines in photodynamic therapy, imaging and theranostics. **Theranostics**. 2(9): 916-966. doi:10.7150/thno.4571.

Kamkaew, A., Chen, F., Zhan, Y., Majewski, R. L., and Cai, W. (2016). Scintillating nanoparticles as energy mediators for enhanced photodynamic therapy. **ACS Nano**. 10(4): 3918-3935. doi:10.1021/acsnano.6b01401.

Kanaras, A. G., Kamounah, F. S., Schaumburg, K., Kiely, C. J., and Brust, M. (2002). Thioalkylated tetraethylene glycol: A new ligand for water soluble monolayer protected gold clusters. **Chem Commun**. 2294-2295. doi:10.1039/B207838B.

Keren, S., Zavaleta, C., Cheng, Z., Zerda, A., Gheysens, O., and Gambhir, S. (2008). Noninvasive molecular imaging of small living subjects using raman spectroscopy. **PNAS USA**. 105: 5844-5849. doi:10.1073/pnas.0710575105.

Kim, J., Lee, N., and Hyeon, T. (2017). Recent development of nanoparticles for molecular imaging. **Philos Trans A Math Phys Eng Sci**. 375: 2107. doi: 10.1098/rsta.2017.0022.

Kou, J., Dou, D., and Yang, L. (2017). Porphyrin photosensitizers in photodynamic therapy and its applications. **Oncotarget**. 8(46): 81591-81603. doi:10.18632/ oncotarget.20189.

Kwiatkowski, S., Knap, B., Przystupski, D., Saczko, J., Kędzierska, E., Knap-Czop, K., Kotlińska, J., Michel, O., Kotowski, K., and Kulbacka, J. (2018). Photodynamic therapy – mechanisms, photosensitizers and combinations. **Biomed Pharmacother**. 106: 1098-1107. doi:10.1016/j.biopha.2018.07.049.

Lengenfelder, B., Mehari, F., Hohmann, M., Heinlein, M., Chelales, E., Waldner, M., Klämpfl, F., Zalevsky, Z., and Schmidt, M. (2019). Remote photoacoustic sensing using speckle-analysis. **Sci Rep-UK**. 9: 1057. doi:10.1038/s41598-018-38446-x.

Lim, W. T., Tan, E. H., Toh, C. K., Hee, S. W., Leong, S. S., Ang, P. C. S., Wong, N. S. , and Chowbay, B. (2010). Phase I pharmacokinetic study of a weekly liposomal paclitaxel formulation (Genexol-PM) in patients with solid tumors. **Ann Oncol**. 21(2): 382-388. doi:10.1093/annonc/mdp315.

Lu, F.-M., and Yuan, Z. (2015). PET/SPECT molecular imaging in clinical neuroscience: recent advances in the investigation of CNS diseases. **Quant Imag Med Surg**. 5(3): 433-447. doi:10.3978/j.issn.2223-4292.2015.03.16.

Luo, S., Zhang, E., Su, Y., Cheng, T., and Shi, C. (2011). A review of NIR dyes in cancer targeting and imaging. **Biomaterials**. 32(29): 7127-7138. doi:10.10 16/j.biomaterials.2011.06.024.

Lux, F., Mignot, A., Mowat, P., Louis, C., Dufort, S., Bernhard, C., Denat, F., Boschetti, F., Brunet, C., Antoine, R., Dugourd, P., Laurent, S., Elst, L. V., Muller, R., Sancey, L., et al. (2011). Ultrasmall rigid particles as multimodal probes for medical applications. **Angew Chem Int Edit**. 50(51): 12299-12303. doi:10.1002/anie.201104104.

Maeda, H. (2015). Toward a full understanding of the EPR effect in primary and metastatic tumors as well as issues related to its heterogeneity. **Adv Drug Deliver Rev**. 91. doi:10.1016/j.addr.2015.01.002.

Maeda, H., Wu, J., Sawa, T., Matsumura, Y., and Hori, K. (2000). Tumor vascular permeability and the EPR effect in macromolecular therapeutics: a review. **J Control Release**. 65(1): 271-284. doi:10.1016/S0168-3659(99)00248-5.

Min, Y., Caster, J. M., Eblan, M. J., and Wang, A. Z. (2015). Clinical translation of nanomedicine. **Chem Rev**. 115(19): 11147-11190. doi:10.1021/acs.chemrev. 5b00116.

Moan, J., and Peng, Q. (2002). An outline of the hundred-year history of PDT. **Anticancer Res**. 23: 3591-3600.

Moghimi, S., and Szebeni, J. (2003). Stealth liposomes and long circulating nanoparticles: Critical issues in pharmacokinetics, opsonization and protein-binding properties. **Prog Lipid Res**. 42: 463-478. doi:10.1016/S01637827 (03)00033-X.

Moore, C., and Jokerst, J. V. (2019). Strategies for image-guided therapy, surgery, and drug delivery using photoacoustic imaging. **Theranostics**. 9(6): 1550-1571. doi:10.7150/thno.32362.

Morley, S., Griffiths, J., Philips, G., Moseley, H., O'Grady, C., Mellish, K., Lankester, C. L. Faris, B., Young, R. J., Brown, S. B., and Rhodes, L. E. (2012). Phase IIa randomized, placebo-controlled study of antimicrobial photodynamic therapy in bacterially colonized, chronic leg ulcers and diabetic foot ulcers: A new approach to antimicrobial therapy. **J Dermatol**. 168. doi:10.1111/bjd. 12098.

Ng, K. K., Lovell, J. F., Vedadi, A., Hajian, T., and Zheng, G. (2013). Self-assembled porphyrin nanodiscs with structure-dependent activation for phototherapy and photodiagnostic applications. **ACS Nano**. 7(4): 3484-3490. doi:10.1021/nn40 0418y.

Nyman, E., and Hynninen, P. (2004). Research advances in the use of tetrapyrrolic photosensitizers for photodynamic therapy. **J Photoch Photobio B**. 73: 1-28. doi:10.1016/j.jphotobiol.2003.10.002.

O'Brien, M., Wigler, N., Inbar, M., Rosso, R., Grischke, E., Santoro, A., Catane, R., Kieback, D., Tomczak, P., Ackland, S., Orlandi, F., Mellars, L., Alland, L., and Tendler, C. (2004). Reduced cardiotoxicity and comparable efficacy in a phase III trial of pegylated liposomal doxorubicin HCl (CAELYX/Doxil) versus conventional doxorubicin for first-line treatment of metastatic breast cancer. **Ann Oncol**. 15: 440-449. doi:10.1093/annone/mdh097.

Orrenius, S., Gogvadze, V., and Zhivotovsky, B. (2015). Calcium and mitochondria in the regulation of cell death. **Biochem Bioph Res Co**. 460: 72-81. doi:10.1016/j.bbrc.2015.01.137.

Owens, D., and Peppas, N. (2006). Opsonization, biodistribution, and pharmacokinetics of polymeric nanoparticles. **Int J Pharm**. 307: 93-102. doi:10.1016/j.ijpharm.2005.10.010.

Peer, D., Karp, J., Hong, S., Farokhzad, O., Margalit, R., and Langer, R. (2007). Nanocarriers as an emerging platform for cancer therapy. **Nat Nanotechnol**. 2: 751-760. doi:10.1038/nnano.2007.387.

Phan, T., and Bullen, A. (2010). Practical intravital two-photon microscopy for immunological research: Faster, brighter, deeper. **Immunol Cell Biol**. 88: 438-444. doi:10.1038/icb.2009.116.

Prabhakar, U., Blakey, D., Maeda, H., Jain, R., Sevick, E., Zamboni, W., Farokhzad, O., Barry, S., Gabizon, A., and Grodzinski, P. (2013). Challenges and key considerations of the enhanced permeability and retention effect for nanomedicine drug delivery in oncology. **Cancer Res**. 73: doi:10.1158/0008-5472.CAN-12-4561.

Rancan, F., Helmreich, M., Mölich, A., Ermilov, E. A., Jux, N., Röder, B., Hirsch, A., and Böhm, F. (2007). Synthesis and *in vitro* testing of a pyropheophorbide-a-fullerene hexakis adduct immunoconjugate for photodynamic therapy. **Bioconjugate Chem**. 18 (4): 1078-1086. doi:10.1021/bc0603337.

Rapozzi, V., Zacchigna, M., Biffi, S., Garrovo, C., Cateni, F., Stebel, M., Zorzet, S., Bonora, G. M., Drioli, S., and Xodo, L. (2010). Conjugated PDT drug:

Photosensitizing activity and tissue distribution of PEGylated pheophorbide a. **Cancer Biol Ther**. 10(5): 471-482. doi:10.4161/cbt.10.5.12536.

Redza-Dutordoir, M., and Averill-Bates, D. A. (2016). Activation of apoptosis signalling pathways by reactive oxygen species. **Biochim Biophy Acta Molec Cell Res**. 1863(12): 2977-2992. doi:10.1016/j.bbamcr.2016.09.012.

Reich, G. (2005). **Near-infrared spectroscopy and imaging: Basic principles and pharmaceutical applications** (Vol. 57).

Saba, T. M. (1970). Physiology and physiopathology of the reticuloendothelial System. **Arch Intern Med**. 126(6): 1031-1052. doi:10.1001/archinte.1970. 00310120093014.

Sajid, M., Ilyas, M., Basheer, C., Tariq, M., Daud, M., Baig, N., and Shehzad, F. (2015). Impact of nanoparticles on human and environment: review of toxicity factors, exposures, control strategies, and future prospects. **Environ Sci Pollut Res Int**. 22(6): 4122-4143. doi:10.1007/s11356-014-3994-1.

Shen, S., Jiang, D., Cheng, L., Chao, Y., Nie, K., Dong, Z., Kutyreff, C. J., Engle, J. W., Huang, P., Cai, W., and Liu, Z. (2017). Renal-clearable ultrasmall coordination polymer nanodots for chelator-free ^{64}Cu-labeling and imaging-guided enhanced radiotherapy of cancer. **ACS Nano**. 11(9): 9103-9111. doi:10.1021/acsnano.7b03857.

Sinha, R., Kim, G., Nie, S., and Shin, D. (2006). Nanotechnology in cancer therapeutics: Bioconjugated nanoparticles for drug delivery. **Mol Cancer Ther**. 5: 1909-1917. doi:10.1158/1535-7163.MCT-06-0141.

Sun, S., Sun, S., Sun, Y., Wang, P., Zhang, J., Du, W., Wang, S., and Liang, X. (2019). Bubble-manipulated local drug release from a smart thermosensitive

cerasome for dual-mode imaging guided tumor chemo-photothermal therapy. **Theranostics**. 9(26): 8138-8154. doi:10.7150/thno.36762.

Tan, G., Li, W., Cheng, J., Wang, Z., Wei, S., Jin, Y., Guo, C., and Qu, F. (2016). Magnetic iron oxide modified pyropheophorbide-a fluorescence nanoparticles as photosensitizers for photodynamic therapy against ovarian cancer (SKOV-3) cells. **Photoch Photobio Sci**. 15(12): 1567-1578. doi:10.1039/C6PP00340K.

Tang, S., Peng, C., Xu, J., Du, B., Wang, Q., Vinluan, R. D., Yu, M., Kim, M. J., Zheng, J. (2016). Tailoring renal clearance and tumor targeting of ultrasmall metal nanoparticles with particle density. **Angew Chem Int Ed**. 55(52): 16039-16043. doi:10.1002/anie.201609043.

Teraphongphom, N., Kong, C. S., Warram, J. M., and Rosenthal, E. L. (2017). Specimen mapping in head and neck cancer using fluorescence imaging. **Laryngoscope Investig Otolaryngol**. 2(6): 447-452. doi:10.1002/lio2.84.

Verma, S., Sallum, U., Athar, H., Rosenblum, L., Foley, J., and Hasan, T. (2009). Antimicrobial photodynamic efficacy of side-chain functionalized benz [a]phenothiazinium dyes. **Photochem Photobiol**. 85: 111-118. doi:10.1111/j.1751-1097.2008.00403.x.

Wagner, V., Dullaart, A., Bock, A.-K., and Zweck, A. (2006). The emerging nanomedicine landscape. **Nat Biotechnol**. 24(10): 1211-1217. doi:10.1038/nbt1006-1211.

Walkey, C. D., Olsen, J. B., Guo, H., Emili, A., and Chan, W. C. W. (2012). Nanoparticle size and surface chemistry determine serum protein adsorption

and macrophage uptake. **J Am Chem Soc**. 134(4): 2139-2147. doi:10.1021/ja2084338.

Wang, L. V., and Hu, S. (2012). Photoacoustic tomography: *in vivo* imaging from organelles to organs. **Science**. 335(6075): 1458-1462. doi:10.1126/science.1216210.

West, J. D., and Marnett, L. J. (2006). Endogenous reactive intermediates as modulators of cell signaling and cell death. **Chem Res Toxicol**. 19(2): 173-194. doi:10.1021/tx050321u.

Xu, N., Yao, M., Farinelli, W., Hajjarian, Z., Wang, Y., Redmond, R., and Kochevar, I. (2014). Light-activated sealing of skin wounds. **Laser Surg Med**. 47. doi:10.1002/lsm.22308.

Yang, Z., and Chen, X. (2019). Semiconducting perylene diimide nanostructure: multifunctional phototheranostic nanoplatform. **Account Chem Res**. 52(5): 1245-1254. doi:10.1021/acs.accounts.9b00064.

Youle, R., and Bliek, A. (2012). Mitochondrial fission, fusion, and stress. **Science**. 337: 1062-1065. doi:10.1126/science.1219855.

Yu, M., Zhou, C., Liu, L., Zhang, S., Sun, S., Hankins, J., Sun, X., and Zheng, J. (2017). Interactions of renal-clearable gold nanoparticles with tumor microenvironments: Vasculature and acidity effects. **Angew Chem Int Ed**. 129. doi:10.1002/ange.201612647.

Zhang, Y.-N., Poon, W., Tavares, A. J., McGilvray, I. D., and Chan, W. C. W. (2016). Nanoparticle–liver interactions: Cellular uptake and hepatobiliary elimination. **J Control Release**. 240: 332-348. doi:10.1016/j.jconrel.2016.01.020.

Zhou, A., Wei, Y., Wu, B., Chen, Q., and Xing, D. (2012). Pyropheophorbide-a and c(RGDyK) comodified chitosan-wrapped upconversion nanoparticle for targeted near-infrared photodynamic therapy. **Mol Pharmaceut**. 9(6): 1580-1589. doi:10.1021/mp200590y.

Zoroddu, M. A., Medici, S., Ledda, A., Nurchi, V. M., Lachowicz, J. I., and Peana, M. (2014). Toxicity of nanoparticles. **Curr Med Chem**. 21(33): 3837-3853.
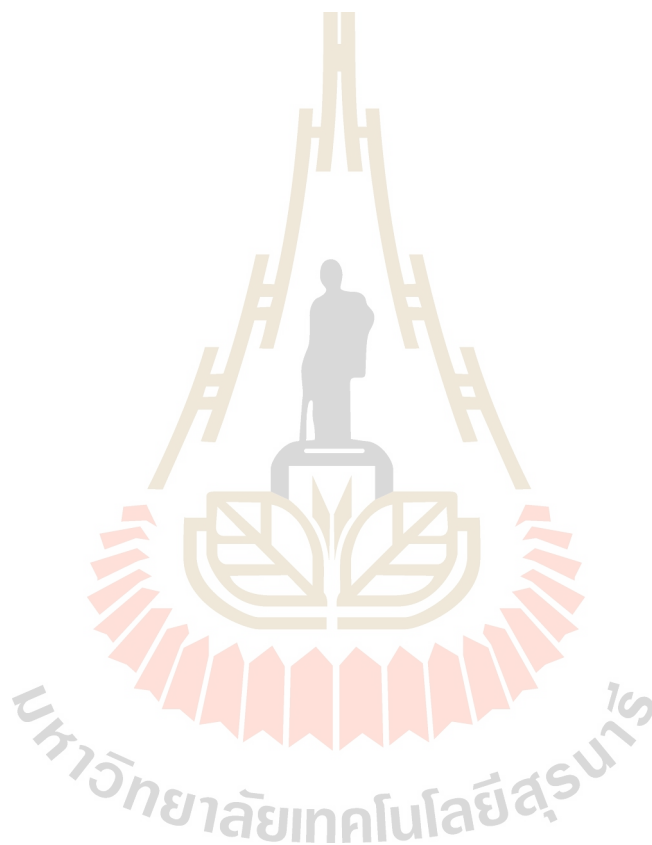
CHAPTER III

EXPERIMENTAL SECTION

3.1 Nanomaterial synthesis and characterization

3.1.1 Chemicals

Chemicals used in this research are listed in Table 3.1 and Table 3.2.

Table 3.1 Chemicals use for nanomaterial synthesis.

Chemicals	Formula	Supplier
Pyropheophorbide-a (Pa)	$C_{33}H_{34}N_4O_3$	Frontier Scientific
Methoxypolyethylene glycol amine 5kDa	$H_2N(CH_2)_2$ $(OCH_2CH_2)_nOCH_3$	Biomatrik
1-ethyl-3-(3-dimethyl aminopropyl) carbodiimide (EDC)	$C_8H_{17}N_3$	Sigma-Aldrich
Dimethyl sulfoxide (DMSO)	$(CH_3)_2SO$	Tokyo Chemical Industry

Table 3.2 Molecular probe for material characterization and for cell experiments.

Chemicals	Formula	Supplier
Singlet oxygen sensor green (SOSG)	$C_{34}H_{21}O_7Cl$	Fisher Scientific
1,3-diphenylisobenzofuran (DPBF)	$C_{20}H_{14}O$	Sigma-Aldrich
Zinc phthalocyanine (ZnPc)	$C_{32}H_{16}N_8Zn$	Sigma-Aldrich
Methyl thiazolyl tetrazolium (MTT)	$C_5H_6N_5S$	Sigma-Aldrich
4′, 6-diamidino-2-phenylindole (DAPI)	$C_{16}H_{15}N_5$	Sigma-Aldrich

3.1.2 Synthesis of Pa-PEG nanodots

Pyropheophorbide-a conjugated with amine polyethylene glycol (Pa-PEG) nanodots were synthesized by a facile method similar to the previously reported protocol (Cheng et al., 2017). Briefly, Pa (10 μmol) and EDC (30 μmol) were mixed in 1 mL dimethyl sulfoxide (DMSO) and stirred for 1 h at 25 ℃ to activate a carboxylic group on Pa. After that, the activated-Pa was dropwise added into DMSO solution containing mPEG-NH$_2$ (9.5 μmol) and continued stirring for 24 h at 25 ℃. Excess amounts of EDC, unreacted Pa, and DMSO were removed by dialysis for 24 h against DI water using a dialysis bag molecular weight cut off (MWCO) 8,000-14,000 Da. Finally, the final product was obtained by filtration using Millipore filter (10 kDa MWCO) and washed three times with DI water. The resulting Pa-PEG nanodots were re-dispersed in 3 mL DI water and stored at 4 ℃ for future use.

3.1.3 Characterizations

3.1.3.1 Transmission electron microscopy (TEM). TEM was used to visualize a morphology of Pa-PEG with high spatial resolution using a Tecnai F20 transmission electron microscope (FEI) with a 200-kV field emission gun. For sample preparation, Pa-PEG nanodots were suspended in water and then dropped on a microgrid with a holey carbon copper as a support membrane. The support membrane was dried at 70 °C under a heat lamp before imaging. The diameter of Pa-PEG nanodots was determined by Nano Measurer 1.2.5 version.

3.1.3.2 Hydrodynamic size (HDs) and Zeta-potential measurement. Pa-PEG nanodots were measured a hydrodynamic size by a Zetasizer Nano Z (Malvern) in physiological media: phosphate-buffered saline (PBS), fetal bovine serum (FBS), Roswell Park Memorial Institute (RPMI) 1640 medium, and deionized (DI) water.

Zeta-potentials of both Pa-PEG nanodots and free Pa molecules dispersed in water were recorded.

3.1.3.3 Absorption and emission spectra. Absorption spectra of free Pa and Pa-PEG nanodots in DI water were recorded from a PerkinElmer Lambda 750 UV-Vis-NIR spectrometer. The absorption spectra were scanned from 250 nm to 800 nm with a data interval of 1 nm, medium speed, and 5.0 nm slit width. Fluorescent spectra of both compounds were obtained from Horiba FluoroMax 4 spectrometer at 660 nm excitation with setting parameters: the observed emission range of 700 nm to 800 nm, 1 nm data interval, and 5.0 nm slit width.

3.1.3.4 ^{1}H-Nuclear magnetic resonance (^{1}H-NMR). Pa-PEG nanodots powder were dissolved in DMSO-d$_6$ and loaded into an NMR tube. Then, ^{1}H-NMR spectra were recorded on a 600 MHz NMR spectrometer at room temperature. Chemical shifts of spectra were reported in ppm unit from the solvent resonance.

3.1.3.5 Matrix assisted laser desorption/ionization–time of flight (MALDI-TOF). MALDI-TOF data was obtained from ultrafleXtremeTM, which was made by Bruker Daltonics, Germany. The standard peptide was used as the standard. Pa-PEG nanodots suspended in water were dropped on the target plate and carried out under the electrospray ionization (ESI) detector.

3.1.3.6 Photobleaching. Pa-PEG nanodots suspended in PBS were filled in the Eppendorf tube. Fluorescent intensity of Pa-PEG nanodots was monitored at 0 days, and then the solution was kept at 4 °C for further imaging at day 1, 3, 5, and 12, using Maestro EX fluorescence imager with 660 nm excitation and 700 nm emission filters. Exposure time was 1,000 ms for each measurement.

3.1.3.7 **Thin layer chromatography (TLC).** TLC was implemented using a silica plate as a stationary phase, and the mixture of acetone: dichloromethane (7:3) was developed as a mobile phase. Then, free Pa solution and Pa-PEG nanodots dispersed in water were spotted on the silica plate above a bottom edge 1.0 cm. After that the TLC plate was developed in a chamber contained the mobile phase for separation. The spots on TLC can be visualized by naked eyes and under the UV light.

3.1.3.8 **Colloidal stability.** Free Pa molecules and Pa-PEG nanodots suspended in water were mixed with 9% NaCl solution in a ratio of 1:1 and then the solutions were centrifuged at room temperature under 10,000 rpm for 5 min. In addition, free Pa molecules dissolved in DMSO were also investigated using the same protocol.

3.1.4 Reactive Oxygen Species Detection

3.1.4.1 **Singlet oxygen detection.** Singlet oxygen production was detected according to the previously reported protocol (Cheng et al., 2017). Briefly, singlet oxygen sensor green (SOSG) 10 μL (0.5 mM) was added into 2 mL of Pa-PEG nanodots solution containing 30 μM of Pa. Then, the solution was exposed to a red LED lamp (600~700 nm) at a power density of 10 mW cm^{-2} for 5, 10, 20, 30, and 60 min. Free Pa solution dissolved in DMSO/water at the same Pa concentration of Pa-PEG nanodots and DI water were also carried out as the control using the same method. Finally, fluorescent intensities of SOSG were measured at an excitation of 494 nm.

3.1.4.2 Singlet oxygen quantum yield. Singlet oxygen quantum yield ($\Phi\Delta$) of free Pa and Pa-PEG nanodots were carried out by an indirect method, using zinc phthalocyanine (ZnPc) and 1,3-diphenylisobenzofuran (DPBF) as a standard and singlet oxygen scavenger, respectively, following the reported procedure (Ramos et al., 2015). In brief, 20 μL of 10 μM DPBF was dropped into 3 mL of Pa-PEG solution containing 2 μM of Pa in DMSO. Then, the mixed solutions were revealed to a red LED lamp at a power density of 10 mW cm–2 for 0, 1, 2, 3, and 4 seconds. Absorption intensities of DPBF at 418 nm were determined to quantify the singlet oxygen consuming-rates by a plate reader (Epoch Microplate Spectrophotometer). To check photostability of material under the presence of singlet oxygen, the absorbance of Pa-PEG nanodots at 660 nm was also recorded at the same time points. ZnPc and free Pa were also examined as the standard and control at the same concentration using the same method. Then, the $\Phi\Delta$ values were calculated following equation (1):

$$\Phi_\Delta = \Phi_\Delta^{ZnPc} \frac{w.\, I_{abs}^{ZnPc}}{w^{ZnPc}.\, I_{abs}} \tag{1}$$

Where (Φ_Δ^{ZnPc}) is the singlet oxygen quantum yield for ZnPc ($\Phi_\Delta = 0.67$ in DMSO) (Pietrangeli et al., 2015); w and w^{ZnPc} are the DPBF photobleaching rates in the presence of Pa-PEG nanodots, and ZnPc, respectively; I_{abs} and I_{abs}^{ZnPc} are the light absorption values for Pa-PEG nanodots ($\lambda = 660$ nm) and ZnPc ($\lambda = 660$ nm), respectively.

3.2 Cell experiments

3.2.1 Cell culture and *in vitro* experiments

4T1 cells (murine breast cancer) were cultured in RPMI-1640 medium supplementing 10% fetal bovine serum (FBS), 1% penicillin/streptomycin, and 2 mL of glutamine 200 mM. The cells were kept at 37 °C under a humidified atmosphere containing 5% CO_2.

3.2.2 *In vitro* photodynamic therapy

4T1 cells were seeded at a density of 1 x 10^4 cells/well into 96-well plates and incubated with the Pa-PEG nanodots at various concentrations (0-40 µM) for 24 h. The cells from the experimental group were irradiated by a red LED lamp at a power density of 10 mW cm^{-2} for 30 and 60 min, whereas the control groups were kept in the dark. Subsequently, all cells were cultured in the dark for another 12 h before washing with PBS (3 times) and incubated with RPMI containing 20% of methyl thiazolyl tetrazolium (MTT) solution (5 mg mL^{-1}) for another 3 h under the same condition. Then, the cells were washed with 3 times PBS before DMSO (100 µL) was added into each well to dissolve formazan crystal. Finally, the absorbance of formazan solutions was detected at 490 nm to determine the relative cell viabilities. Furthermore, calcein AM and PI were co-stained to visualize live and dead cells. Cells were seeded into 6-well plates at 2 x 10^5 cells/well and cultured for 24 h at 37 °C under 5% CO_2. Pa-PEG nanodots were dispersed into RPMI cell-culture media with a concentration of 0.25 µM. After incubation for 8 h, the cells were irradiated by a red LED lamp for 30 min and then incubated for another 24 h. After that, 4 µM calcein acetoxymethyl and propidium iodide (calcein AM/PI, Thermo Fisher Scientific) were added to each well,

and the cells were incubated for 5 min before imaging by ZOE Fluorescent Cell Imager (Bio-Rad).

3.2.3 Cellular uptake investigation

4T1 cells were seeded into 12-well plates containing cover glass slip at a density of 1 x 10^5 cells/well and cultured for 24 h. Pa-PEG nanodots were added into each well at the final concentration of 1 μM of Pa and cultured for various time points (1, 3, 8, and 12 h). After being washed with PBS (3 times), the cells were fixed with 4% paraformaldehyde for 10 min and washed with PBS before staining with 4′, 6-diamidino-2-phenylindole (DAPI) for 15 min. Later, the cells were imaged by a confocal microscope (Leica TCS-SP5II, Germany). Z-stacking imaging was manipulated by a confocal microscope (Invitrogen A24864) to visualize the accumulation of Pa-PEG nanodots inside the cells after 8 h of incubation at 5 μM of Pa concentration, using the same cell preparing method. Dose-dependent flow cytometry was also administered, referring the reported procedure (Vranic et al., 2013). Concisely, 4T1 cells at a density of 1 x 10^5 cells treated with Pa-PEG nanodots at the final dose of 0, 1.25, 2.5, 5.0, 10, and 20 μM of Pa for 8 h were transferred into Eppendorf tubes and washed with cold PBS. Those of cells were centrifuged at 800 g at 4 °C for 5 min and suspended in 400 μL of PBS with 2 times washing. After centrifugation, the cells were dispersed into 500 μL of cold PBS and kept at 4 °C for flow cytometry analysis at 637 nm for excitation and 730 nm for detecting emission wavelength.

3.2.4 Intramolecular ROS generation detection

The cells were seeded into 12-well plates containing cover glass slip at a density of 1 x 10^5 cells/well and cultured for 12 h. The cell plates were divided into 2

groups of 4, including; (I) control; (II) light only; (III) sample adding only; and (IV) sample + light. After cell adherence, the Pa-PEG nanodots were added into group III and IV representing the experimental groups while free Pa molecules were added instead considering as the control groups, and both were incubated for 8 h before adding 2′,7′-dichlorofluoresceindiacetate (DCFH-DA) into each well at the concentration of 20 μM. Afterward, the cover glass slips of both groups were brought to image using Leica TCS-SP5II confocal microscope.

3.3 Animal experiments

3.3.1 Tumor implementation

4T1 xenografts were prepared by a subcutaneous injection of 1 x 10^6 cells in PBS (~50 μL) onto the back of shaved female balb/c mice. The mice were used when the volume of the tumor reached up to ~150 mm^3.

3.3.2 *In vivo* fluorescence imaging

Pa-PEG nanodots (300 μL, 1.8 mg mL^{-1}) were intravenously injected into 4T1 tumor-bearing mice. Accumulation of Pa-PEG nanodots was monitored using Maestro EX fluorescence imager with 660 nm excitation and 700 nm emission filters, respectively, with the exposure time of 50 ms. After 8 and 24 h post injection, the mice were sacrificed and the major organs including the tumor, liver, spleen, kidney, heart, stomach, lung, and intestine were collected for *ex vivo* distribution. Afterward, the tumor and major organs were frozen in optimum cutting temperature (OCT) solution at –80 ºC for histology studies using a confocal microscope (Leica TCS-SP5II, Germany).

3.3.3 *In vivo* photoacoustic imaging

The mice were intravenously injected with Pa-PEG nanodots and monitored for real-time accumulation of Pa-PEG nanodots at the tumor site and kidney using Visualsonic Vevo 2100 LAZER system with 710 nm excitation. Afterward, the mice were sacrificed, and the major organs were collected. FL and PA signals were displayed as radiant efficiency.

3.3.4 *In vivo* photodynamic therapy

The mice were randomly divided into four groups (n = 5) for various treatments: (i) control; (ii) light only; (iii) Pa-PEG i.v. injection; and (iv) Pa-PEG i.v. injection + light. After 300 μL of Pa-PEG nanodots (300 μL, 1.8 mg mL^{-1}) was injected into mice bearing 4T1 tumors, the tumors of group II and IV were exposed to a red LED lamp (power density = 10 mW cm^{-2}) for 60 min. The tumor sizes were measured every other day using a caliper for 2 weeks. Tumor volumes were calculated as (tumor length) $\times$ (tumor width)^2/2, and V/V_0 (V_0 is the initial tumor volume) was used as relative tumor volumes. Two days after treatment, the tumors from each group were embedded in paraffin for histology study.

3.3.5 Blood analysis and histology examination

Healthy balb/c mice were randomly divided into three groups (n = 3) after intravenously injected of Pa-PEG nanodots (300 μL, 1.8 mg mL^{-1}). The mice were sacrificed at first, and seventh day p.i., while other three untreated mice were used as the control. Subsequent, blood samples (~1 mL for each mouse) were collected for blood panel analysis and blood chemistry examination. In addition, major organs from each mouse were harvested for histological investigation.

3.3.6 Renal clearance

Balb/c mice were intravenous injected with the Pa-PEG nanodots and PBS as a control. Mice' urine were separately collected before and after injection for 30 min and then were imaged by Maestro EX fluorescence imager with 660 nm excitation and 700 nm emission filters, with the exposure time of 1,000 ms.

3.4 References

Cheng, L., Jiang, D., Kamkaew, A., Valdovinos, H. F., Im, H.-J., Feng, L., England, C. G., Goel, S., Barnhart, T. E., Liu, Z., and Cai, W. (2017). Renal-clearable PEGylated porphyrin nanoparticles for image-guided photodynamic cancer therapy. **Adv Funct Mater**. 27(34): 1702928. doi:10.1002/adfm.201702928.

Pietrangeli, D., Rosa, A., Pepe, A., Altieri, S., Bortolussi, S., Postuma, I., Protti, N., Ferrari, C., Cansolino, L., Clerici, A. M., Viola, E., Donzello, M. P., and Ricciardi, G. (2015). Water-soluble carboranyl-phthalocyanines for BNCT. Synthesis, characterization, and *in vitro* tests of the Zn(ii)-nido-carboranyl-hexyl thiophthalocyanine. **Dalton Trans**. 44(24): 11021-11028. doi:10.1039/ C5DT00394F.

Ramos, A. A., Nascimento, F. B., De Souza, T. F. M., Omori, A. T., Manieri, T. M., Cerchiaro, G., and Ribeiro, A. O. (2015). Photochemical and photophysical properties of phthalocyanines modified with optically active alcohols. **Molecules**. 20(8): 13575-13590.

Vranic, S., Boggetto, N., Contremoulins, V., Mornet, S., Reinhardt, N., Marano, F., Baeza-Squiban, A., Boland, S. (2013). Deciphering the mechanisms of cellular uptake of engineered nanoparticles by accurate evaluation of internalization

using imaging flow cytometry. **Part Fibre Toxicol**. 10(1): 2. doi:10.1186/ 1743-8977-10-2.

4.1.2 Colloidal stability examination

Pa-PEG nanoparticles in DI water were dispersed in 9% NaCl solution with a volume ratio of 1:1 and homogeneously mixed for stability test. It was found that all Pa-PEG could greatly dissolve in such high dose of salt solution with no aggregation when observed by naked eyes, or even the mixed solution was centrifuged at 10,000 rpm for 5 min. In contrast, free Pa molecules showed immediate aggregation in the saline solution, in which a high polar environment allows the hydrophobic core of free Pa molecules getting attached and stacked together in order to form aggregation. To prove that the aggregation of free Pa molecules was not from the self-aggregation in water but actually originated from the induction of the saline solution, free Pa molecules were dissolved in DMSO prior adding 9% NaCl at the same ratio. The resulting mixture revealed that the high salt concentration could induce the aggregation of free Pa molecules despite in a homogenous solution. Hence, the formation of the amide bond between PEG and free Pa molecule could excellently enhance the solubility of free Pa molecules in DI water (Figure 4.2).

Figure 4.2 The colloidal stability observation. (a) of Pa-PEG nanodots in a 9% NaCl, (b) of free Pa in the 9% NaCl, and (c) of free Pa in DMSO.

4.1.3 Purity investigation

Thin-layer chromatography (TLC) was carried out using a silica plate as a stationary phase and the mixture of acetone:dichloromethane (7:3) as a mobile phase. After the TLC plate was developed, spots of both Pa-PEG nanoparticle and free Pa molecule demonstrated a visible separation, suggesting that no free Pa were remaining inside the Pa-PEG nanoparticles (Figure 4.3). In addition to chemical selectivity, the Pa-PEG nanoparticle spot was preferably absorbed on the TLC plate compared to the free Pa molecules spot, indicating the vast increase of polarity after PEGylation and its high purity after dialysis.
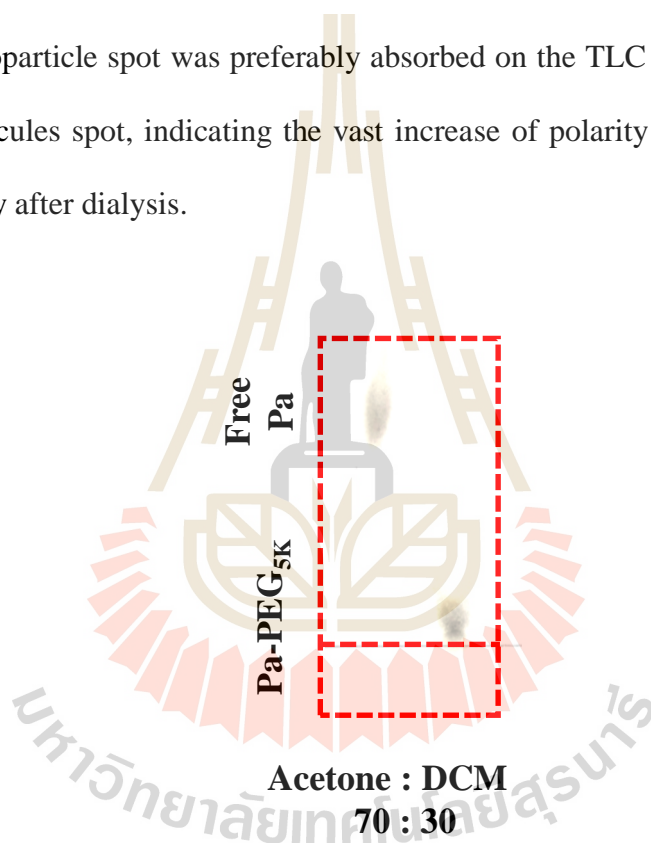
Figure 4.3 Thin-layer chromatography of free Pa and Pa-PEG products. Showing the obvious different distance with no free Pa spot on the Pa-PEG runway.

4.1.4 The confirmation of Pa and PEG conjugation

^{1}H-nuclear magnetic resonance (^{1}H-NMR) firstly performed a chemical shift pattern of free Pa molecules in DMSO-d_6. Then, the ^{1}H-NMR spectrum of Pa-PEG nanomaterials was recorded in comparison with the free Pa one. According to

the obtained spectra, the characteristic new peaks of PEG around 3.5 ppm were dominantly presented in Pa-PEG nanoparticles spectra after PEGylation with new other minor peaks and slightly shift, which derive from the change of the Pa molecules' environment. The additional peak of PEG with no significant change of free Pa fingerprint pattern confirmed the successful conjugation of PEG on the Pa surface (Figure 4.4).
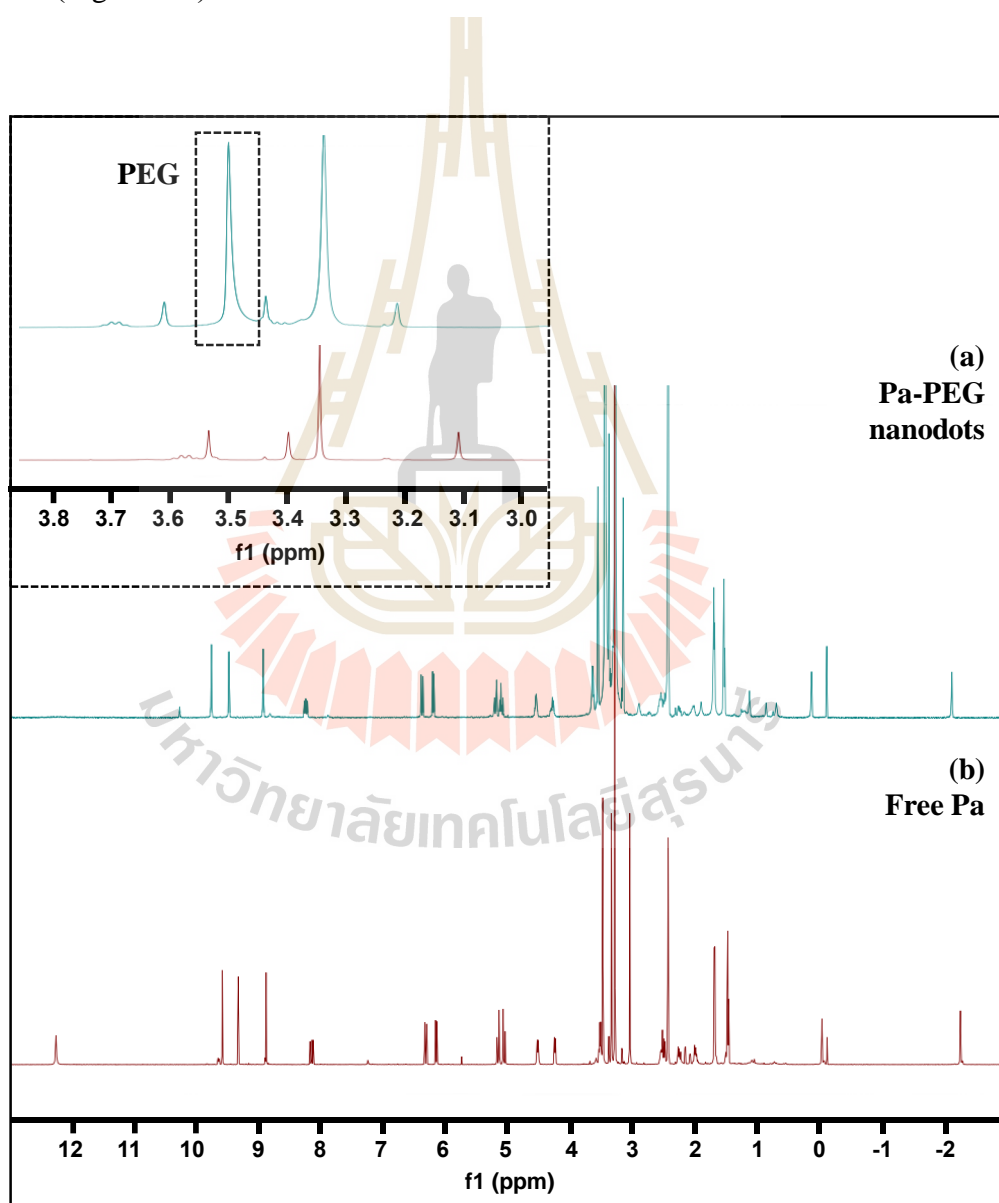
Figure 4.4 ^{1}H-NMR spectra of (a) Pa-PEG nanodots, and (b) free Pa in DMSO. Inserted figure confirmed the existence of PEG after PEGylation.

4.1.5 Molecular mass determination

Matrix-assisted desorption/ionization time-of-flight (MALDI-TOF) revealed the molecular mass peak of Pa-PEG, which was 5,863 m/z. Additionally, Abdellatif and co-worker reported that the mass spectrum of free amine PEG 5kDa showed the peak of mass spectrum in range of 4,300 – 4,800 m/z (Abdellatif, Osman, mohd ali, and Darras, 2016) while in this work the mass peak of Pa-PEG products were observed around 5,500-6,000 m/z, attesting the combination between 5 kDa of amine PEG chain and 534.6 Da of free Pa molecules. Furthermore, the mass spectrum also showed the characteristic pattern of PEG (Figure 4.5).
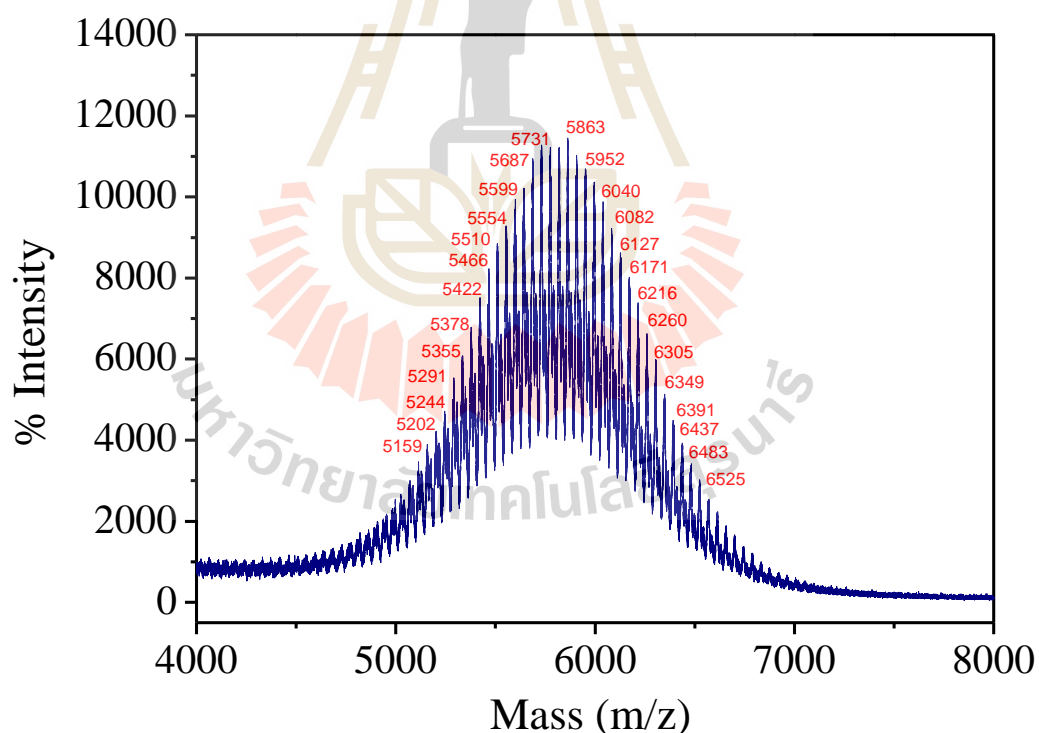
Figure 4.5 Mass spectrum of the Pa-PEG nanodots.

4.1.6 Nanodots formation, zeta-potentials, and stability

Transmission electron microscopy (TEM) image revealed the obtained nanoparticles were uniform nanodots morphology with 2.28 ± 0.45 nm in size (Figure 4.6). While the hydrodynamic size (HDs) was measured to be 5.76 ± 0.56 nm (Figure 4.7), a little larger than the size from TEM; this might be due to the HDs that corresponds to the core and the swollen corona of nanoparticles (Honary and Zahir, 2013; W. Li, Tan, Zhang, Wang, and Jin, 2017; Shen et al., 2017).
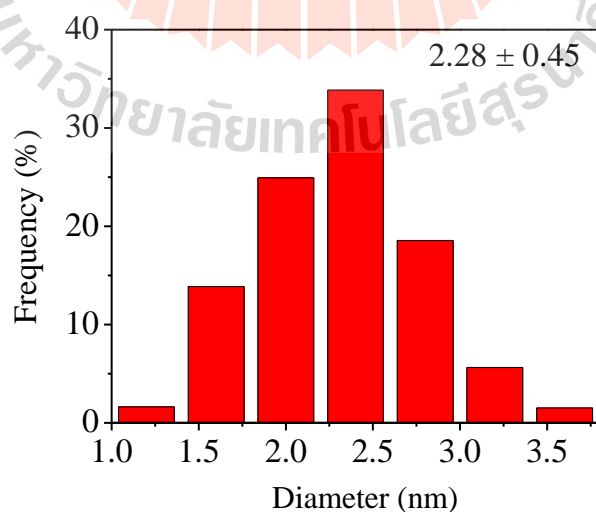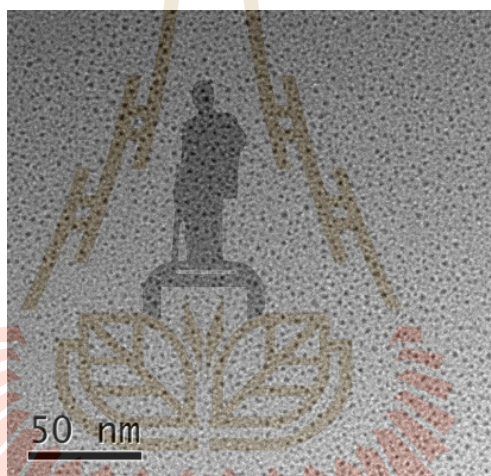
Figure 4.6 Morphology (above) and the diameter distribution of of Pa-PEG nanodots (below).
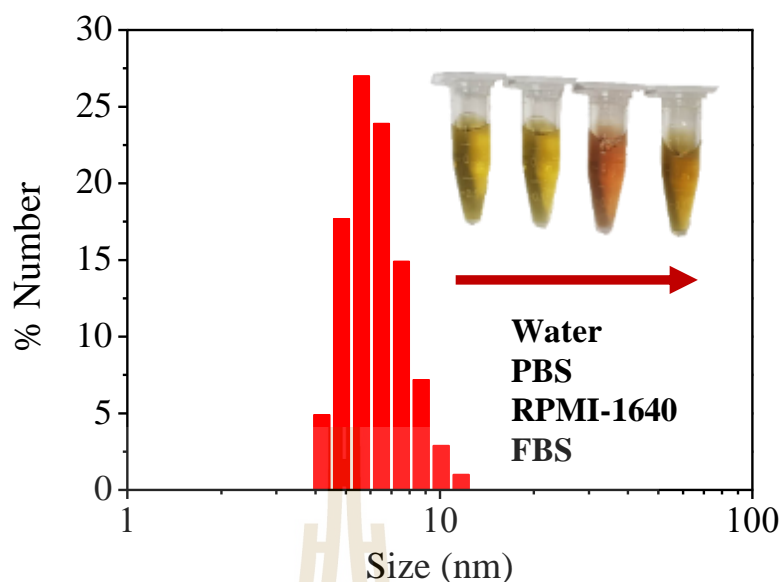
Figure 4.7 Hydrodynamic diameters of Pa-PEG nanodots after incubation in water. Inset: Photo of Pa-PEG nanodots in various physiological solutions.

In addition, red-shift of Soret and Q bands in absorption spectra after modification suggested that free Pa molecule in adducts might be contributed to form nanodots morphology *via* π-π stacking (Figure 4.10, section 4.2.1) (Würthner, Kaiser, and Saha-Möller, 2011). Moreover, the periphery of hydrophilic PEG moieties was able to stabilize the nanodots structure in water during the self-assembly process to maintain individual nanodots (X. Li, Lee, Huang, and Yoon, 2018; Tang et al., 2018; Zou et al., 2017).

The zeta-potentials of Pa-PEG nanodots and free Pa in DI water were -5.70 ± 1.37 and -11.76 ± 1.46 mV, respectively. The decrease of the negative charge of free Pa confirmed the conjugation of free Pa with amino group of PEG (Figure 4.8) (Du, Yu, and Zheng, 2018). Moreover, the HDs of Pa-PEG nanodots exhibited the steady diameter during the period of measurements, demonstrating long-time solubility and stability in DI water and FBS solution for at least 15 days (Figure 4.9).
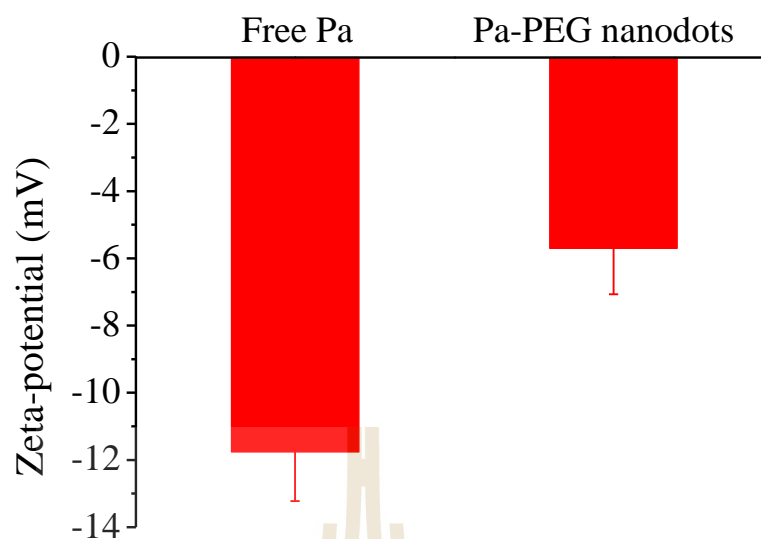
Figure 4.8 The zeta-potentials of free Pa and the Pa-PEG nanodots. Error bars were from three separated experiments.
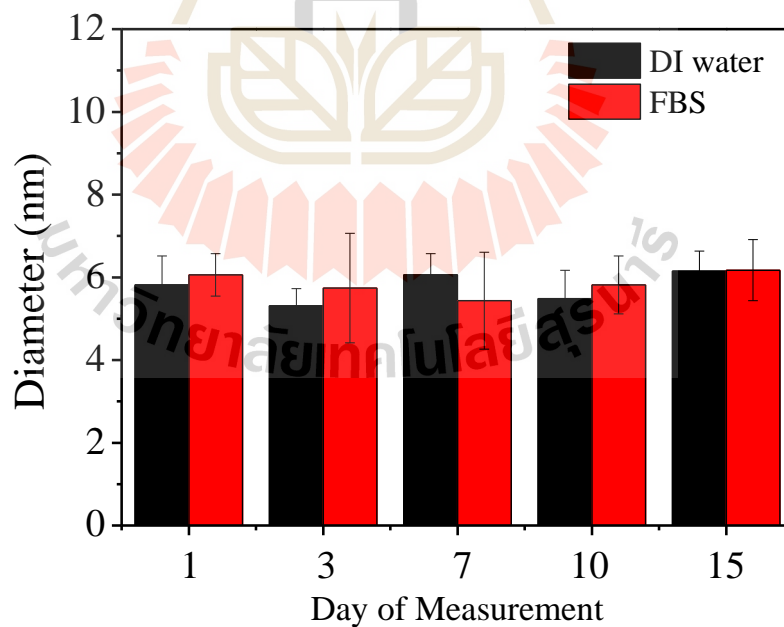
Figure 4.9 Long-term stability evaluation of Pa-PEG nanodots in DI water and FBS.

4.2 Optical properties and singlet oxygen production

4.2.1 Absorption spectra

Free Pa spectrum showed the intensive absorption bands around 383 nm and 680 nm, in which the latter band located in the deep-red region can emerge the generation of photodynamic therapeutic effect. In addition, the deep-red region also provides less absorption by biological substance, which allows high penetrability of therapeutic irradiation light. After PEGylation, however, the UV-Vis-NIR spectrum of Pa-PEG nanodots exhibited the remarkable absorption maxima shifted, accompanied with increasing sharpness from 384 to 450 nm and 680 nm to 710 nm in water (Figure 4.10). Surprisingly, the red-shift of the Q band allows an occurrence of photoacoustic effect, which can produce heat pulse, suggesting the Pa-PEG nanodots might offer *in vivo* photoacoustic imaging accompanied with *in vivo* fluorescent imaging.
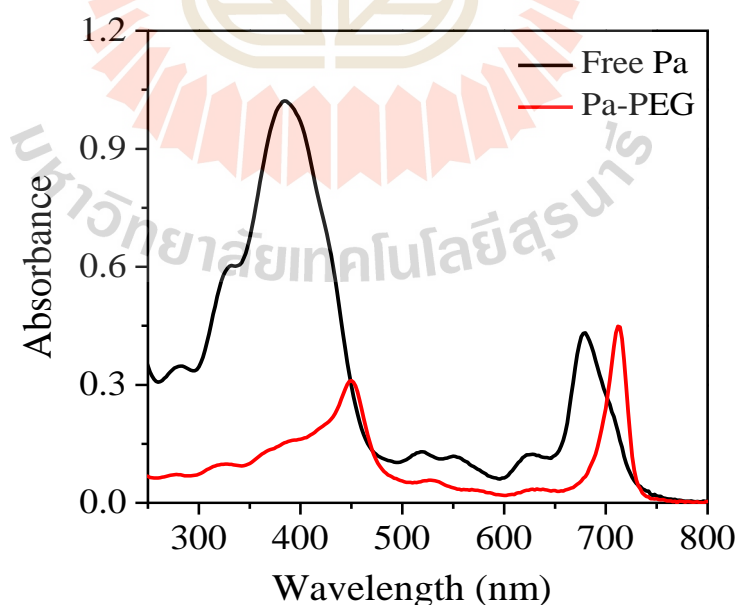
Figure 4.10 UV-Vis-NIR spectra of free Pa in DMSO and Pa-PEG nanodots in water.

4.2.2 Emission investigation

To ensure the optical properties of Pa-PEG nanodots serving as imaging-guided PDT, fluorescent emission and photoacoustic effect were investigated. Upon excitation at 660 nm, the Pa-PEG nanodots displayed a strong emission peak at 725 nm. In contrast, free Pa was mostly quenched in aqueous solution due to the formation of aggregation (Figure 4.11). The results suggested that the improvement of free Pa solubility by conjugating with hydrophilic polymer can enhance fluorescent signal in water, denoting the good property for *in vivo* fluorescent imaging. The standard curve between average FL signal at 660 nm excitation against various concentrations ranging from 3-28 μM was linearly increase with R^2 = 0.9870, showing the concentration-dependent and taking advantage to monitor a nanomaterial distribution in animal's organs (Figure 4.12).
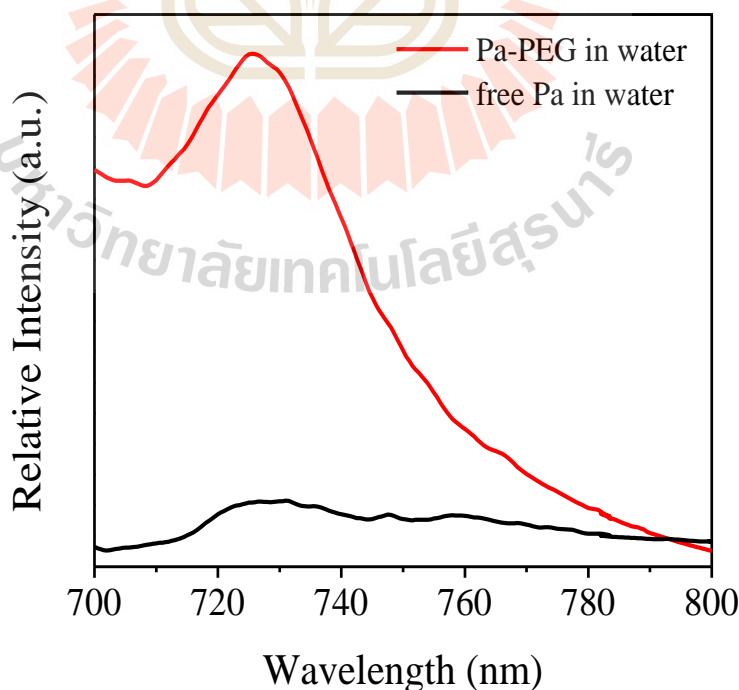
Figure 4.11 Fluorescent spectra of free Pa and the Pa-PEG nanodots in water.
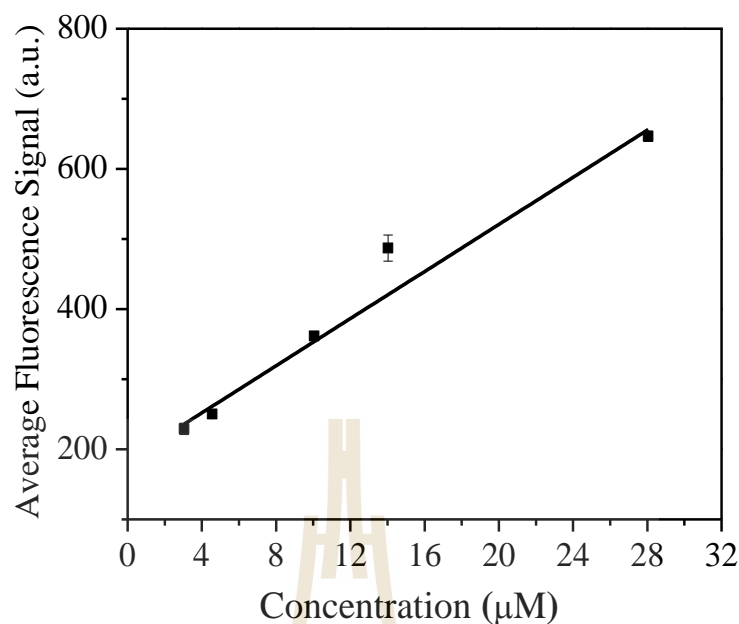
Figure 4.12 Linear relationship of fluorescence signal of the Pa-PEG nanodots.

In addition, exceptional photostability was observed under 1,000 ms of exposure time at 660 nm excitation as the Pa-PEG nanodots (30 μM) could maintain good fluorescence at least 12 days with trivial photodegradation. Moreover, the photograph of FL imaging of the Pa-PEG nanodots also exhibited strong fluorescent signals for up to 12 days, offering long-term investigation based on fluorescent imaging (Figure 4.13). The PA optical property was also evaluated using various concentrations of Pa-PEG nanodots ranging from 0-200 μM and it was found that the nanodots could produce high PA signal upon excitation at 710 nm, and the intensity was dose-dependent manner showing as a linear correlation with $R^2 = 0.9866$, taking advantage to track the amount of nanomaterial in animal's organs for comparing distribution in each organ (Figure 4.14, Figure 4.15).
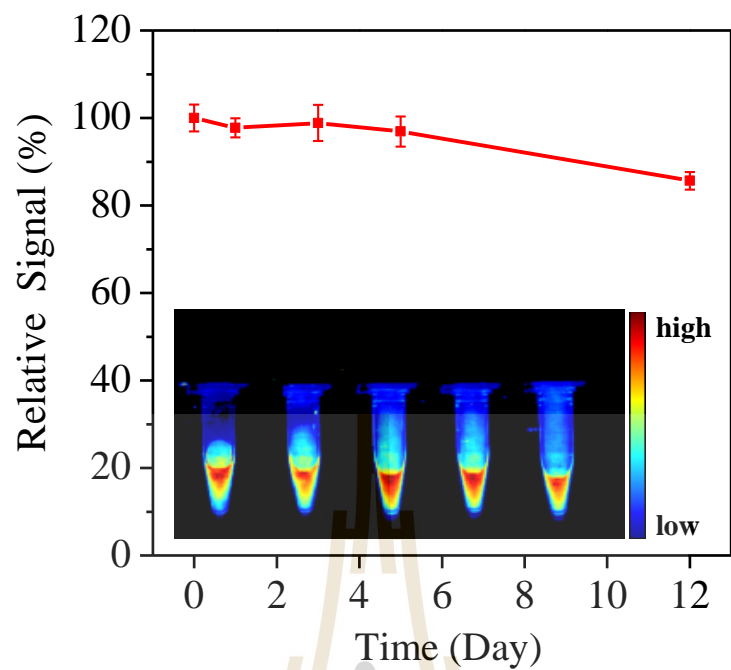
Figure 4.13 Fluorescence stability of Pa-PEG nanodots over extensive time. Inset: Photograph of fluorescence stability of Pa-PEG nanodots.
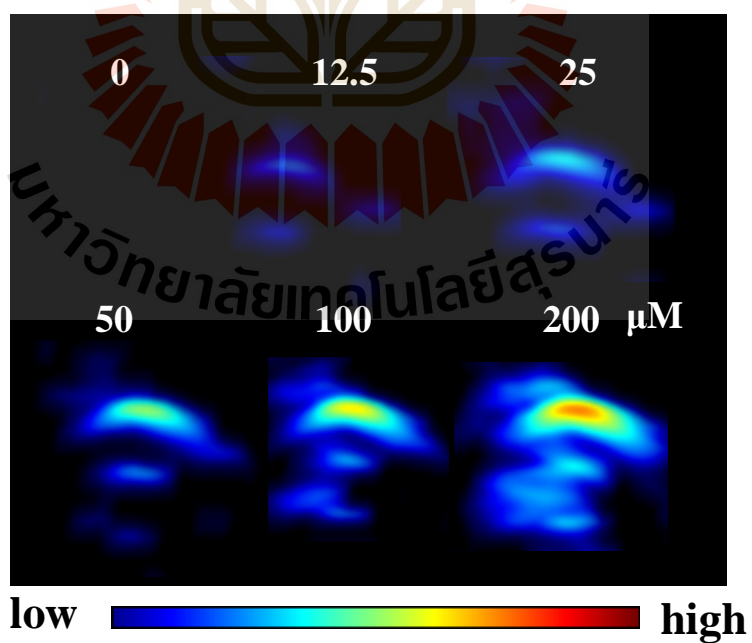
Figure 4.14 Photoacoustic images of Pa-PEG nanodots at various concentrations in water.
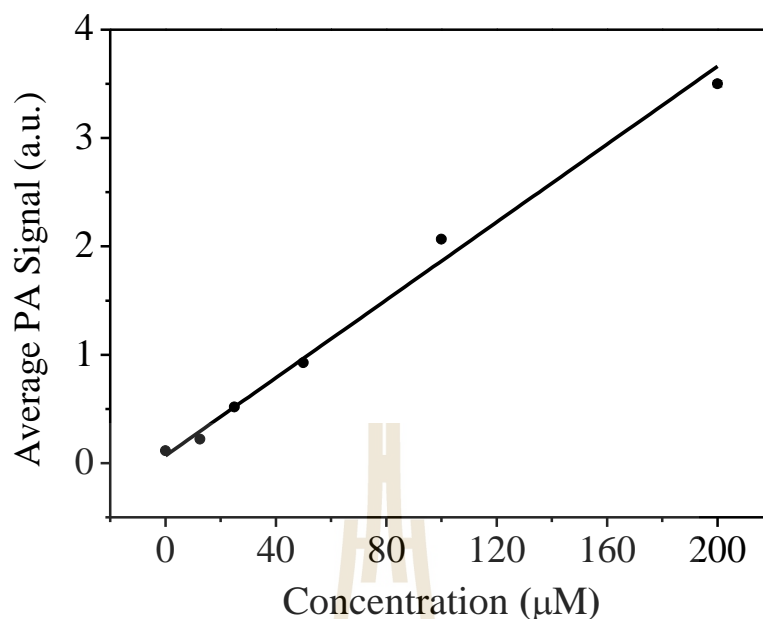
Figure 4.15 The linearity curve of photoacoustic signal against concentrations.

4.2.3 Singlet oxygen quantum yield

Singlet oxygen quantum yield (Φ_Δ) of free Pa and Pa-PEG nanodots were quantified in DMSO using 1,3-diphenylisobenzofuran (DPBF) as a singlet oxygen quencher, and zinc phthalocyanine (ZnPc) was used as a standard. The absorbance of DPBF photoconsumption during a red LED lamp (600~700 nm) irradiation was recorded by keeping track of the decrease of the DPBF maximum absorption at 418 nm, as a function of time (Figure 4.16). Based on first-order plots in Figure 4.17, the Φ_Δ of free Pa nanodots was 55.7% regarded to zinc phthalocyanine as the reference compound (Φ_Δ = 67% in DMSO) (Pietrangeli et al., 2015). Simultaneously, the Φ_Δ of free Pa-PEG nanodots was acquired as 53.6%, which was no significant difference compared to that of free Pa, implying the modification of Pa did not change the generation ability of singlet oxygen.
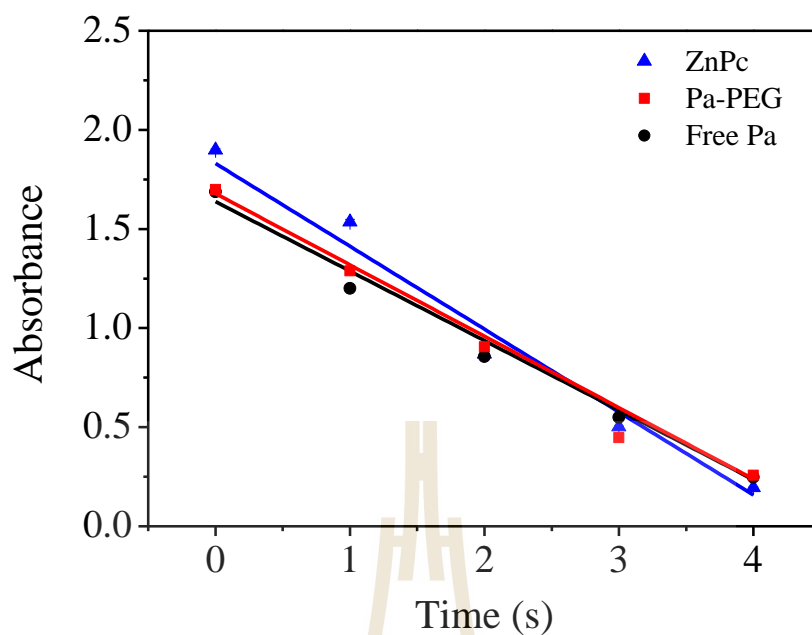
Figure 4.16 UV-Vis absorption of DPBF photodecomposition at 418 nm during reacting with $^1O_2$ under a 660 nm lamp irradiation.
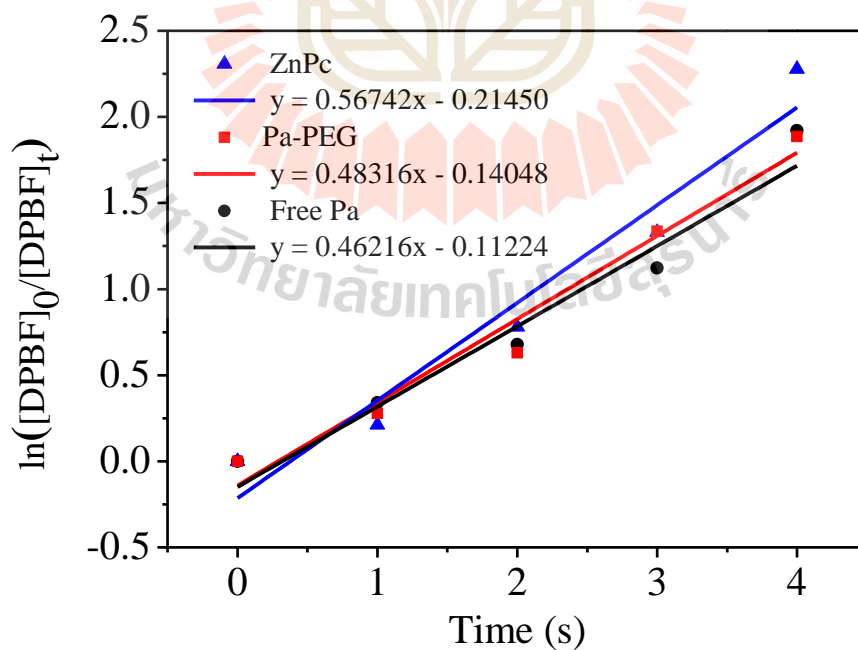
Figure 4.17 The first-order plots of photo consumption rate.

4.2.4 Singlet oxygen detection

Singlet oxygen production was monitored by detecting the fluorescent intensity change of singlet oxygen sensor green (SOSG), singlet oxygen quencher, at 494 nm after a 660 nm LED lamp irradiation of Pa-PEG nanodots. Under the same Pa concentration, the fluorescent signals of SOSG obtained from irradiated Pa-PEG nanodots were higher compared to those from free Pa molecule, indicating that more $^1O_2$ concentration could be generated in water, which might be due to the better solubility of Pa in water after PEGylation, Figure 4.18.
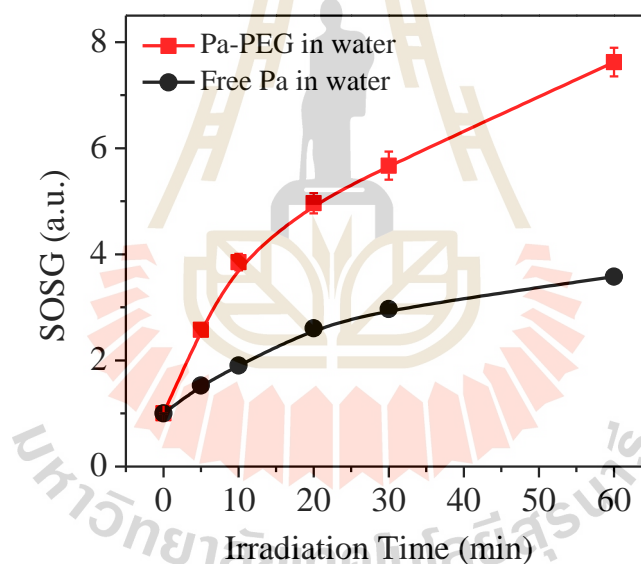
Figure 4.18 Singlet oxygen production rate of free Pa and Pa-PEG nanodots in water.

These optical properties and singlet oxygen production ability results suggest that our Pa-PEG nanodots might serve as a powerful agent for PA/FL imaging-guided PDT.

4.3 Cell assays

4.3.1 Cell viabilities assay

In vitro cytotoxicity of Pa-PEG nanodots was tested in 4T1 murine breast cancer cells using the standard methyl thiazolyl tetrazolium (MTT) assay. The cells maintained full viability when they were treated with Pa-PEG nanodots up to 20 μM for 24 h *without* irradiation (Figure 4.19), demonstrating that Pa-PEG nanodots could not induce cell death under no PDT treatment condition. On the other hand, the cells incubated with 0.25 μM of Pa-PEG nanodots and exposed to a 660 nm LED lamp for 30 min were mostly destroyed confirming singlet oxygen produced by PDT effect could mediate cell devastation (Figure 4.20).
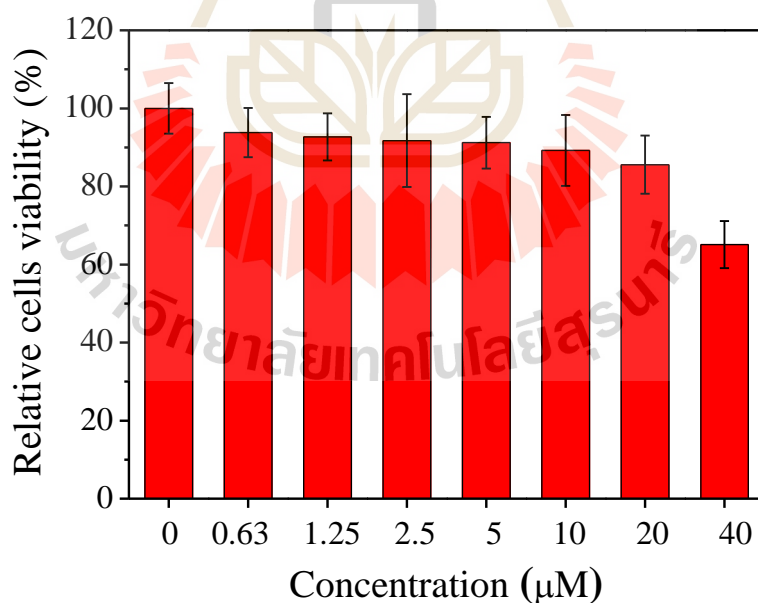
Figure 4.19 The relative cells viabilities of breast cancer (4T1) cells incubating with the Pa-PEG nanodots without lamp irradiation.
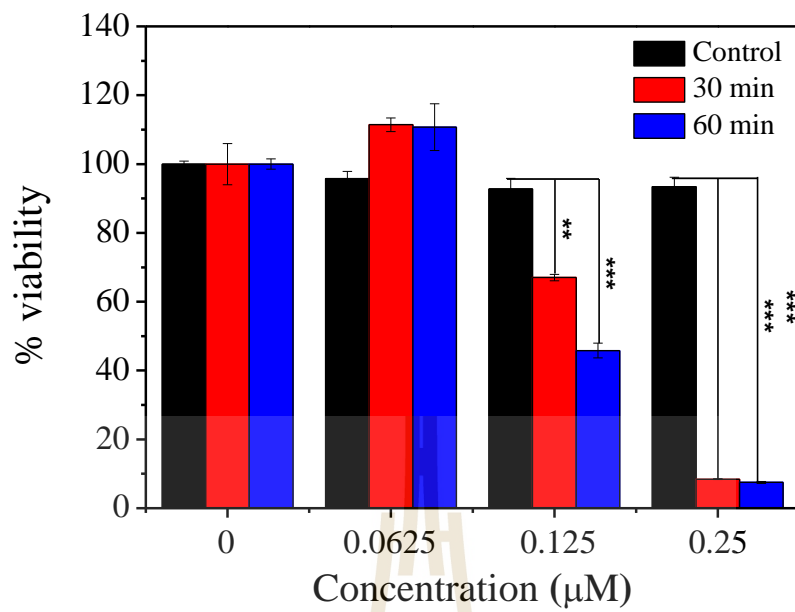
Figure 4.20 Relative cells viabilities of 4T1 cells treated the Pa-PEG nanodots at different Pa concentrations and irradiated with 660 nm lamp.
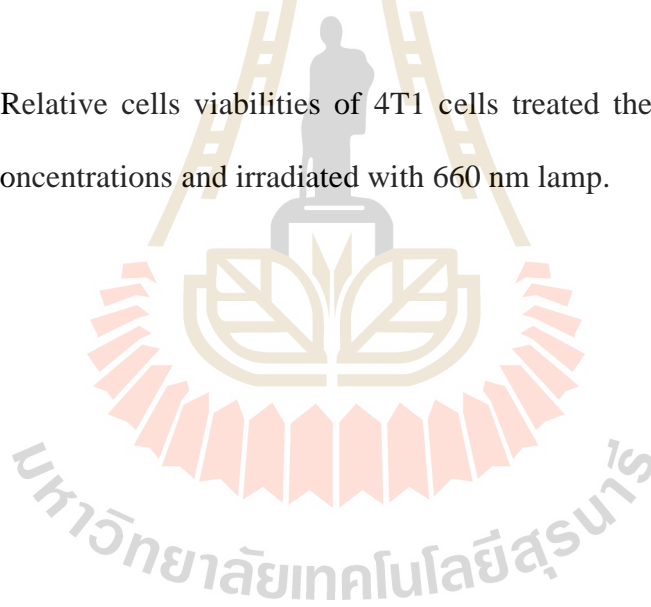
Next, calcein-AM and propidium iodide (PI) co-staining was also performed to ensure Pa-PEG nanodots triggered by a 660 nm light could induce cell death while the non-radiated cells remained alive. Regarding the results in Figure 4.21, green fluorescent light of calcein indicated the viable cells where the endogenous esterase enzyme in healthy cells can cleave the ester bond of calcein-AM, while damaged cells appeared in red fluorescence because PI can penetrate the cell membrane of dead cells and further intercalates between base pairs of DNA strands.
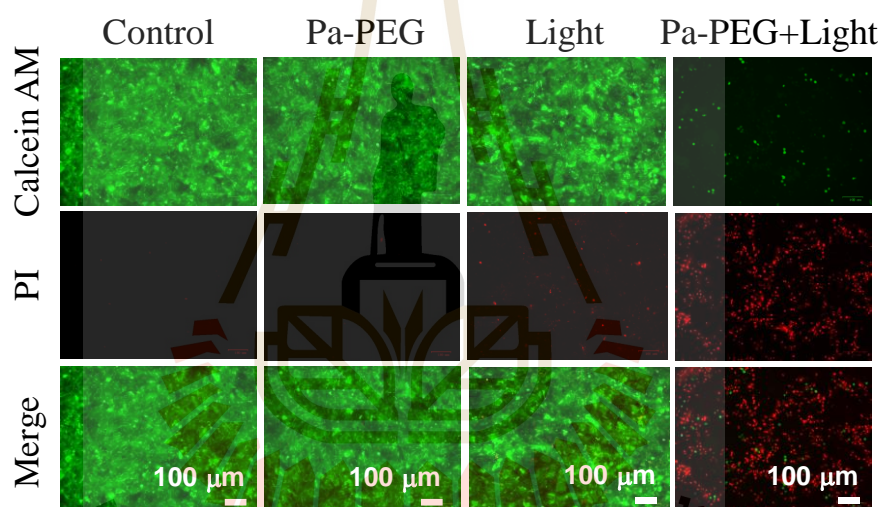
Figure 4.21 Fluorescence images of calcein-AM/PI co-stained 4T1 cells after various treatments with NIR-triggered light. Red and green indicated dead cells and living cells, respectively.

4.3.2 Cellular singlet oxygen detection

To ensure the presence of singlet oxygen inside the cells after irradiation, dichlorodihydrofluorescein diacetate (DCFH-DA) assay was conducted to visualize the existing of singlet oxygen. Non-fluorescence 2',7'-dichlorodihydrofluorescein diacetate was oxidized by ROS-mediated oxidation to obtain the green fluorescence of 2',7'-dichlorofluorescein (DCF) (Cheng et al., 2017). As shown in Figure 4.22, bright green fluorescence from DCF was significantly enhanced when the cells treated with Pa-PEG nanodots were irradiated compared to the other control groups, confirming the generation of singlet oxygen at the cellular level.
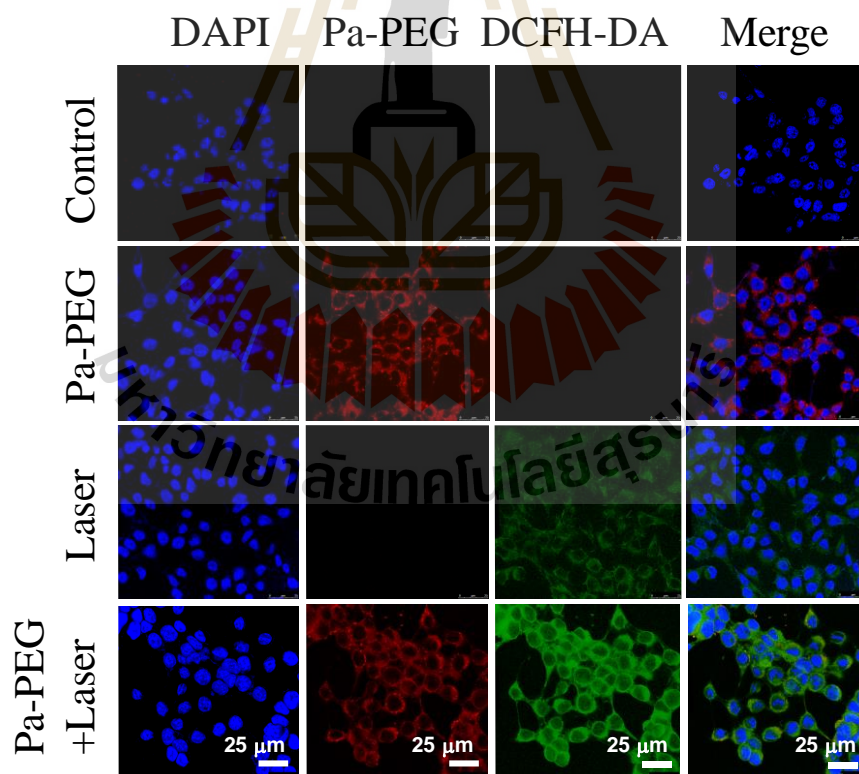
Figure 4.22 *In vitro* ROS production of control and Pa-PEG nanodots treatment in breast cancer cells. Scale bars = 25 μm.

4.3.3 Cellular uptake

Cellular uptake was also performed at different time points 0, 3, 8, and 12 h and monitored by a confocal microscope (Figure 4.23). 4′, 6-diamidino-2-phenylindole (DAPI) was used to stain the nucleus which presents in blue color. The red fluorescent signal was observed from 4T1 cells treated with Pa-PEG nanodots in the cytosol after incubation for 3 h, and the brightness increased to a maximum after 8 h incubation. In contrast, the red fluorescent signal of free Pa was barely observed inside the cells, regarding the aggregation quenched fluorescent signal of free Pa in water (Figure 4.24).
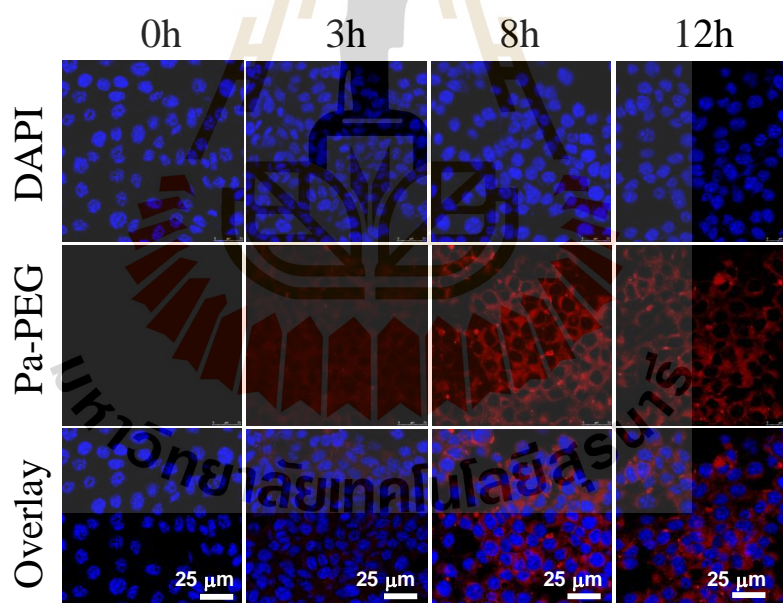
Figure 4.23 Cellular uptake of the Pa-PEG nanodots in 4T1 cells. Scale bars = 25 mm.
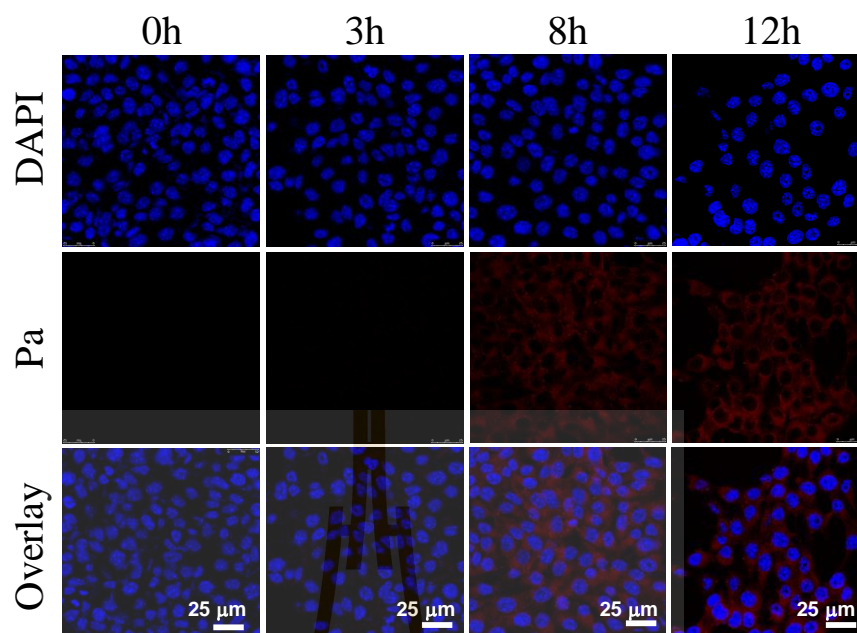
Figure 4.24 Cellular uptake of the free Pa in 4T1 cells. Scale bars = 25 mm.
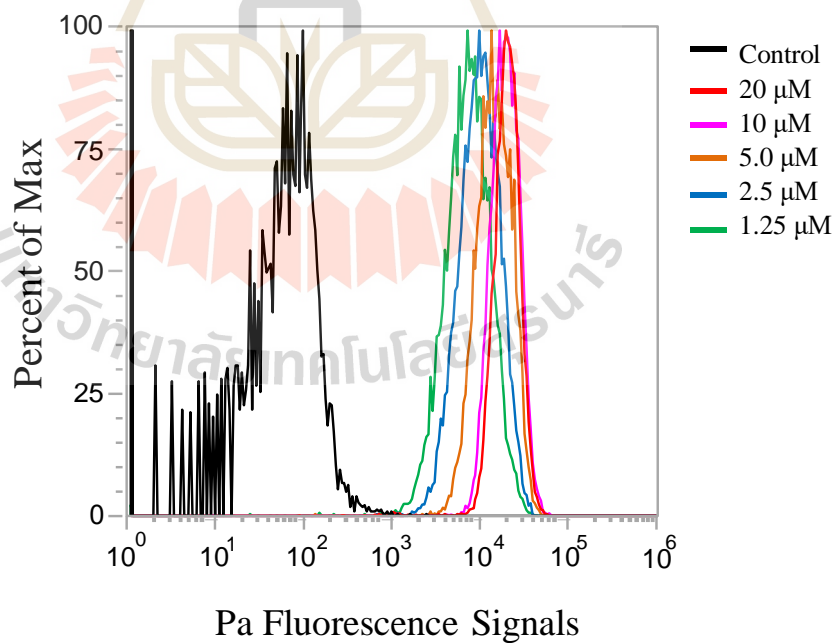
Figure 4.25 The histogram presents the increasing of fluorescence signals in 4T1 cells as a function of concentrations.

Furthermore, the internalization of Pa-PEG nanodots was quantified by flow cytometry (Figure 4.25). The histogram displayed that the fluorescence was significantly enhanced after treated with the Pa-PEG nanodots at various concentrations, confirming the localization inside the cells in a does-dependence manner. Moreover, the cellular uptake of Pa-PEG nanodots was also visualized by z-stacking confocal images (Figure 4.26). 3D images performed the localization of Pa-PEG nanodots in pink color around the nucleus-stained DAPI.

DAPI	Pa-PEG	Overlay
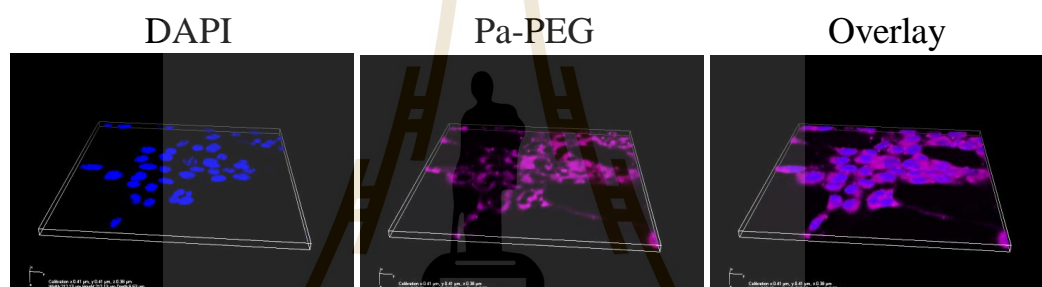
Figure 4.25 Z-stacking imaging of Pa-PEG nanodots incubated with 4T1 cells.

All *in vitro* results suggested that the Pa-PEG nanodots could easily pass through the cell membrane after incubated with the cells at least 8 h and produce a large amount of singlet oxygen inside the 4T1 cell upon exposure to the 660 nm irradiation for triggering the apoptosis process.

4.4 Animal experiments

4.4.1 Fluorescence imaging

4.4.1.1 Optimal time-based FL observation for PDT

Optimal time of Pa-PEG nanodots accumulation at the tumor site was monitored by *in vivo* PA/FL dual-modal imaging. First, Pa-PEG nanodots (300 μL, 1.8 mg mL^{-1} Pa concentration) were intravenously injected into 4T1 tumor-bearing mice and then the fluorescent signal was monitored at various time points. Figure 4.27 showed that Pa-PEG nanodots circulated rapidly through the whole body and were accumulated at the tumor site since the first 2 h post-injection (p.i.). The accumulation of Pa-PEG nanodots at the tumor area continuously increased to reach the maximum at 8 h p.i., suggesting the suitable time of light irradiation for PDT (Figure 4.28).
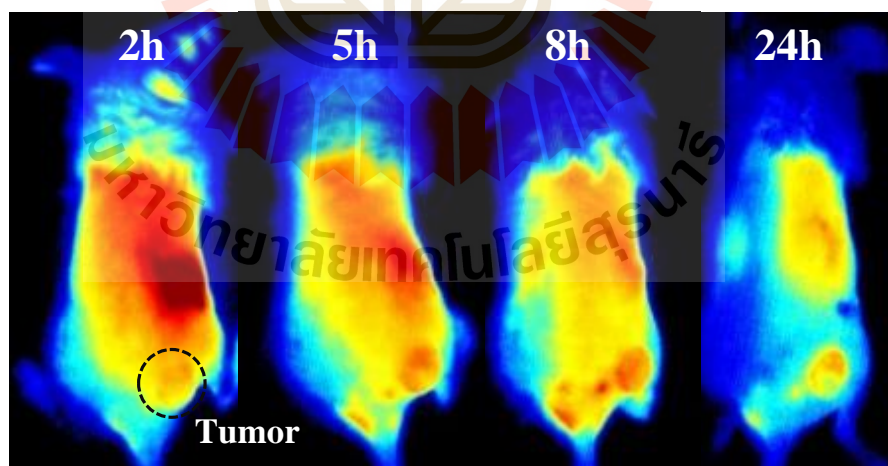
Figure 4.27 Fluorescence images of 4T1 tumor bearing mice post-injecting the Pa-PEG nanodots at different time points**.**
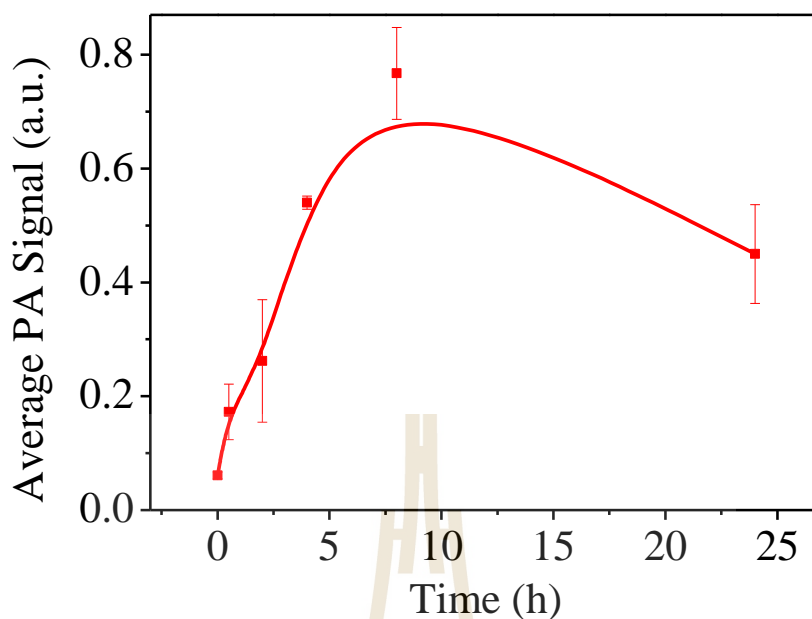
Figure 4.28 Fluorescence signals of tumor at different time points post-injection.

4.4.1.2 *Ex vivo* FL biodistribution

Major organs including liver, spleen, kidney, lung, intestine, stomach, heart, and tumor were taken out at 8 and 24 h p.i. for *ex vivo* fluorescence imaging, and the quantitative fluorescent biodistribution was analyzed (Figure 4.29, Figure 4.30). Strong fluorescent signals were observed from the organs at 8 h, including liver, spleen, kidney, and intestine. The moderate signals were observed from the tumor due to the equilibrium between tumor-targeting ability and clearance ability of Pa-PEG nanodots. The high signal at the stomach was from the food background. However, at 24 h p.i., the fluorescence signals were dimmed down, suggesting most of the nanodots were cleared from the major organs and tumor.
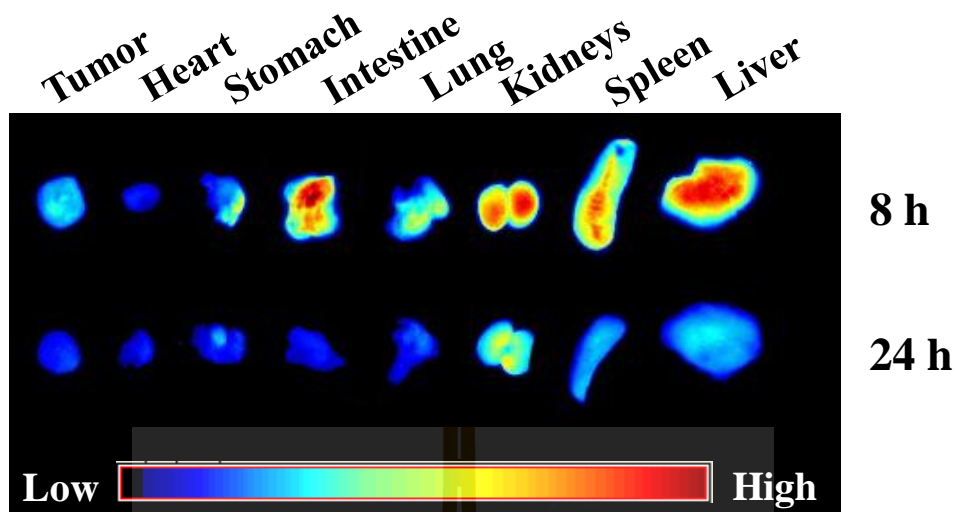
Figure 4.29 *Ex vivo* fluorescence images of main organs and tumor.
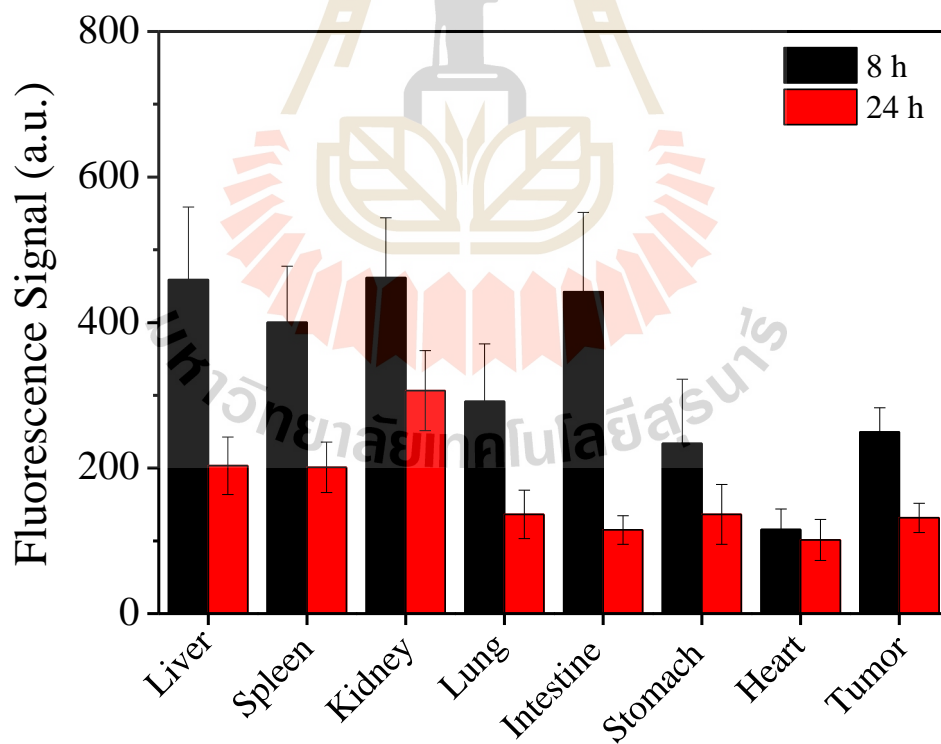
Figure 4.30 Fluorescence biodistribution of major organs and tumor.

4.4.1.3 Urine inspection

The intensive fluorescent signal of kidneys at 24 h p.i. in Figure 4.29 provided preliminary evidence that the ultra-small size of the Pa-PEG nanodots could pass through the kidneys' glomerular membrane for removing out the body *via* the urinary system (Arami, Khandhar, Liggitt, and Krishnan, 2015). To ensure the renal clearance, the mice were intravenously injected the Pa-PEG nanodots and allowed the circulation for half an hour. Afterward, the urine was collected for FL imaging, which found that the high fluorescent signal was observed. Showing the fluorescent signal in urine confirmed the ultrasmall Pa-PEG nanodots were cleared by the renal removing pathway (Figure 4.31).
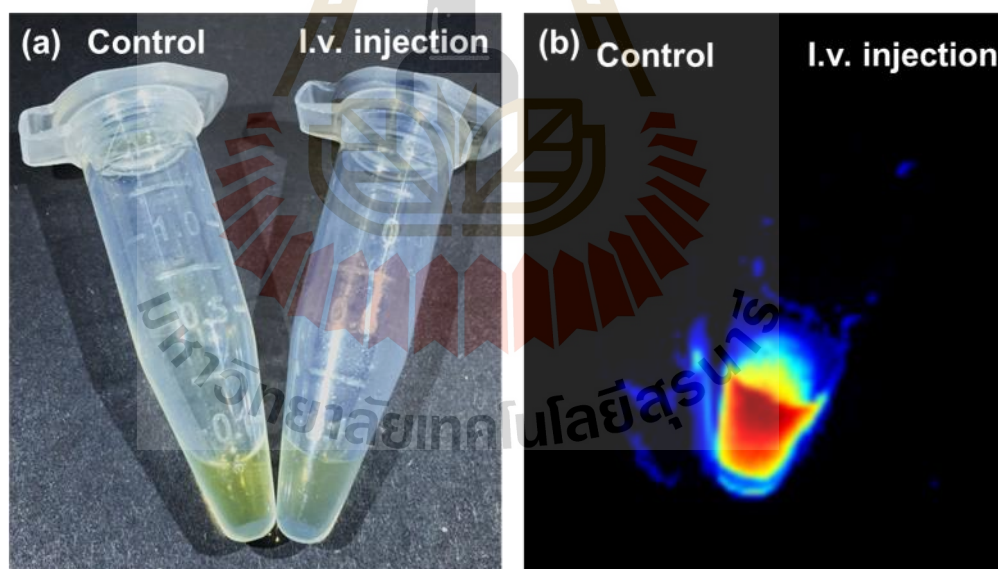
Figure 4.31 Photos of urine collected before and after i.v. injection of Pa-PEG nanodots. (a) White image, (b) Fluorescent image.

4.4.1.4 The observation of nanomaterial distribution in sliced organs

After 8 h p.i., major organs were sectioned and imaged under confocal microscopy to confirm the uptake of Pa-PEG nanodots. Strong red fluorescence was observed in liver, spleen, kidney, and intestine, and the moderate signal was observed from the tumor, indicating the existence of Pa-PEG nanodots in those organs (Figure 4.32).
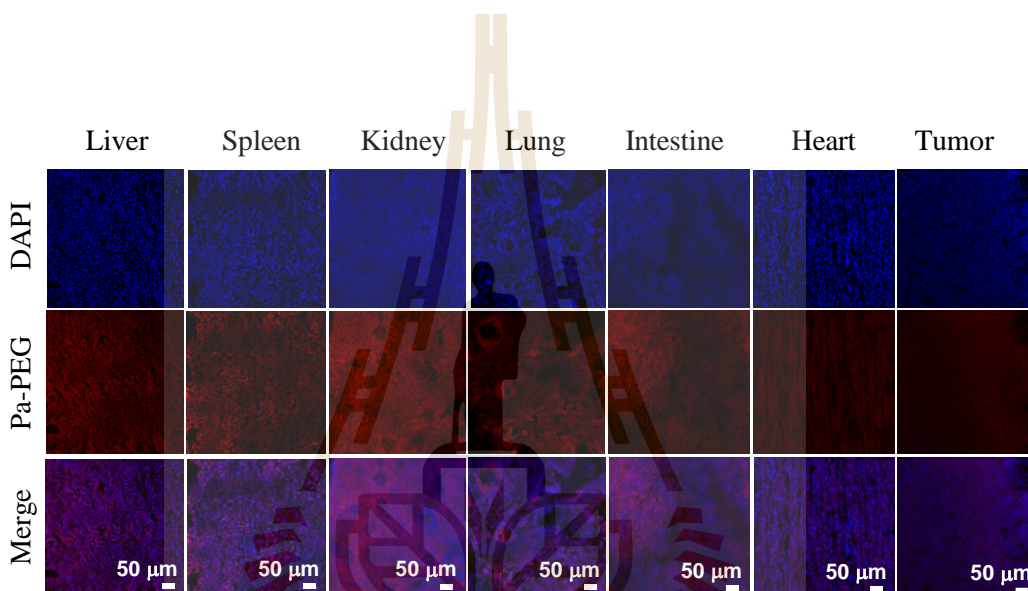
Figure 4.32 Confocal imaged tissue slides of major organs include liver, spleen, kidney, lung, intestine, heart, and tumor at 8 h post injection. Scale bar = 50 μm.

4.4.2 Photoacoustic imaging

4.4.2.1 Optimal time-based PA observation for PDT

in vivo PA imaging was conducted to ensure that Pa-PEG nanodots could serve as dual-modal imaging agent for cancer therapy, and to confirm the retention of Pa-PEG nanodots at the tumor site (Figure 4.33, Figure 4.34). Pre-injection was firstly imaged, and then time-dependent PA imaging was continued after i.v. injection of Pa-PEG nanodots (300 μL, 1.8 mg mL^{-1}) into 4T1 tumor-bearing

mice. PA signal at tumor region showed tumor uptake over time and the nanodots could obviously be retained to the highest distribution at 8 h p.i. before gradually decreased as the function of time until 24 h p.i., which was similar to the FL imaging results. Therefore, Pa-PEG nanodots could be an excellent guiding imaging agent for *in viv*o cancer therapy.
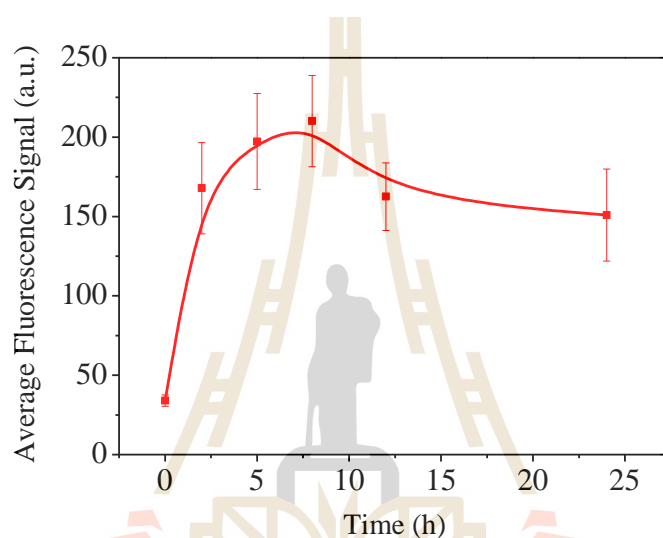
Figure 4.33 Photoacoustic signals of Pa-PEG nanodots at tumor analysis.
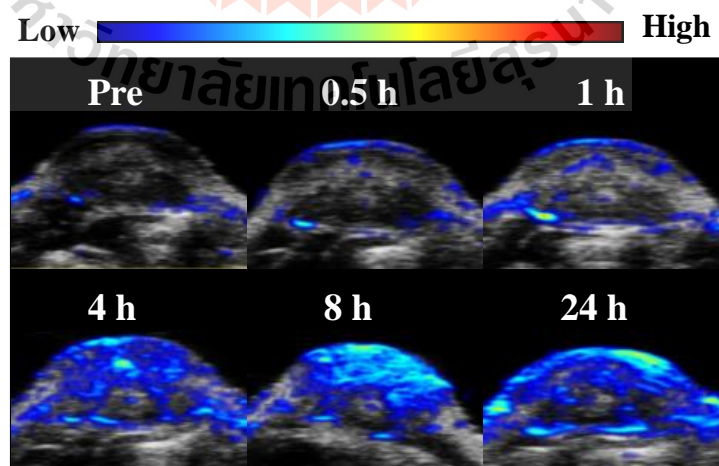
Figure 4.34 Photoacoustic images of Pa-PEG nanodots at tumor post injecting Pa-PEG nanodots at different time points.

4.4.2.2 Real-time PA visualization of kidneys

In general, nanoparticles containing size less than 8 nm with negative charge on the surface can be an advantage for renal clearable (Du et al., 2018; Shen et al., 2017). Thus, the Pa-PEG nanodots with about 5.76 nm (HD) in size with negative zeta potential were also investigated for renal clearance behavior. Time-dependent PA imaging was applied to visualize PA signal in mouse kidneys and the results showed that the signal was risen up during the first 2 h, suggesting the filtration at kidney was allowed by blood circulation after injecting Pa-PEG nanodots (Figure 4.35). After 2 h p.i., the organs were taken out for *ex vivo* PA imaging and the results exhibited Pa-PEG nanodots were observed in kidneys as well as other organs (Figure 4.36). The PA biodistribution pointed out the major accumulation of Pa-PEG nanodots was in the liver, spleen, and kidneys, suggesting that the blood circulation could provide physical filtration of Pa-PEG nanodots at kidney implying the renal pathway activation, while the accumulation in other organs was reabsorbed and circulated for further elimination (Kapusta, 2007).
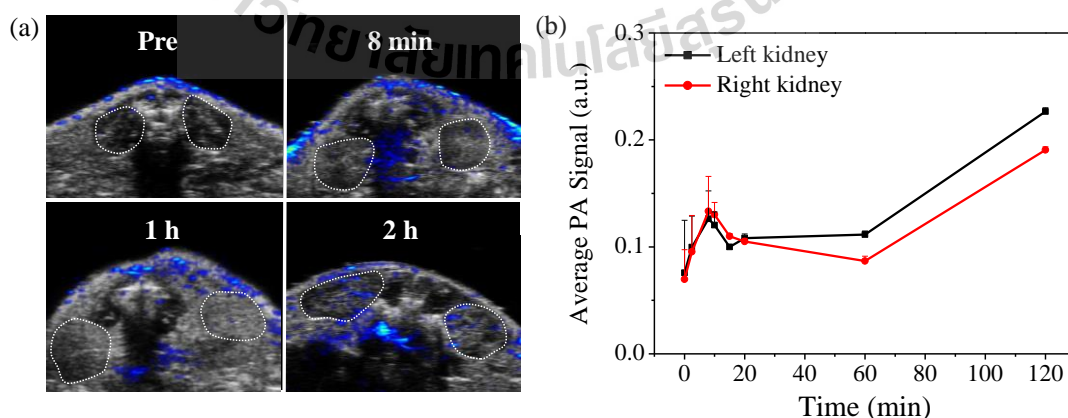
Figure 4.35 Pa-PEG nanodots visualization of kidney uptake. (a) real time *in vivo* PA signal at first 2 h p.i. (b) The plot of PA intensities in the kidney at first 2 h p.i.

(a)

(b)
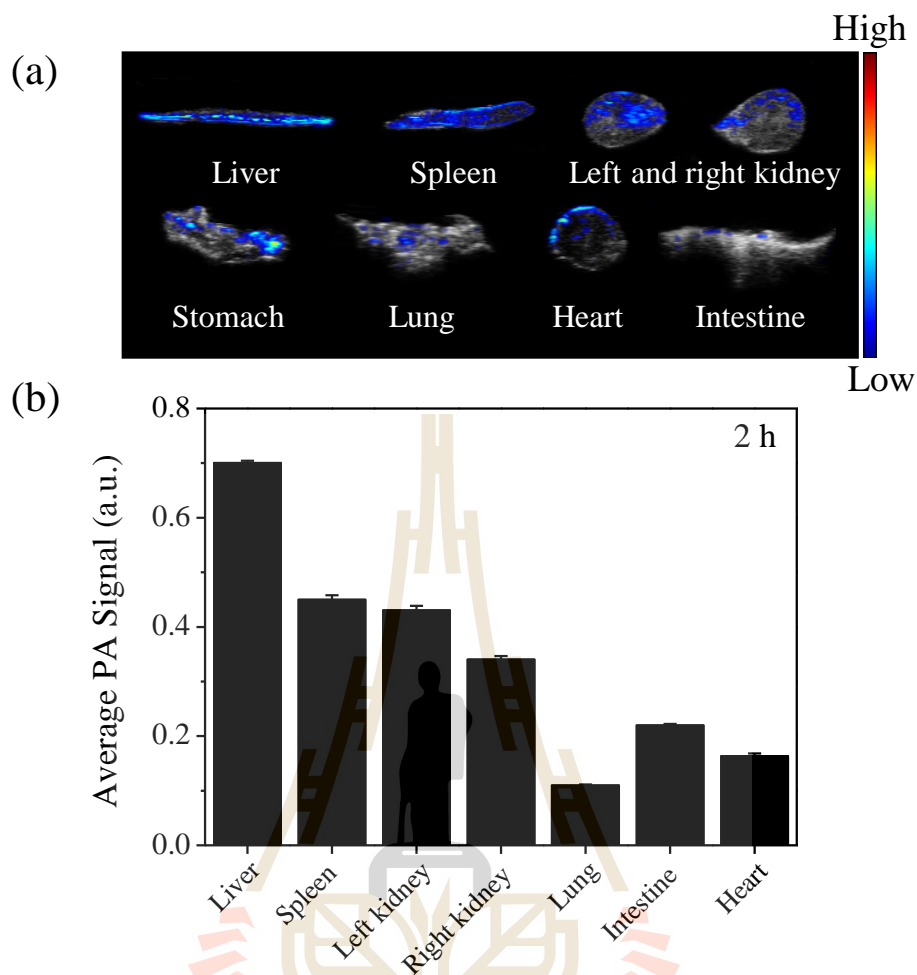
Figure 4.36 Biodistribution of Pa-PEG nanodots based on photoacoustic imaging. (a) *ex vivo* PA images of main organs were observed 2 h p.i. (b) Photoacoustic biodistribution of main organs measured at 2 h post injecting of the Pa-PEG nanodots.

4.4.3 Long-term investigation

4.4.3.1 Clearable monitoring

To demonstrate the excretable behavior of the Pa-PEG nanodots after treatment in long-term, *ex vivo* imaging of major organs were imaged using FL imaging at various time points, including 2 h, 12 h, 1 d, and 7 d (Figure 4.37). Time-dependent biodistribution showed strong Pa-PEG nanodots signal at the first 2 h p.i.

in liver, spleen, kidney, lung, and intestine. The uptake of liver, spleen, lung, and intestine was promptly reduced within 12 h, whereas the FL signal from the kidneys remained at a high level compared to other organs, suggesting that Pa-PEG nanodots could be cleared from the body by passing through the glomerular membrane of kidneys.
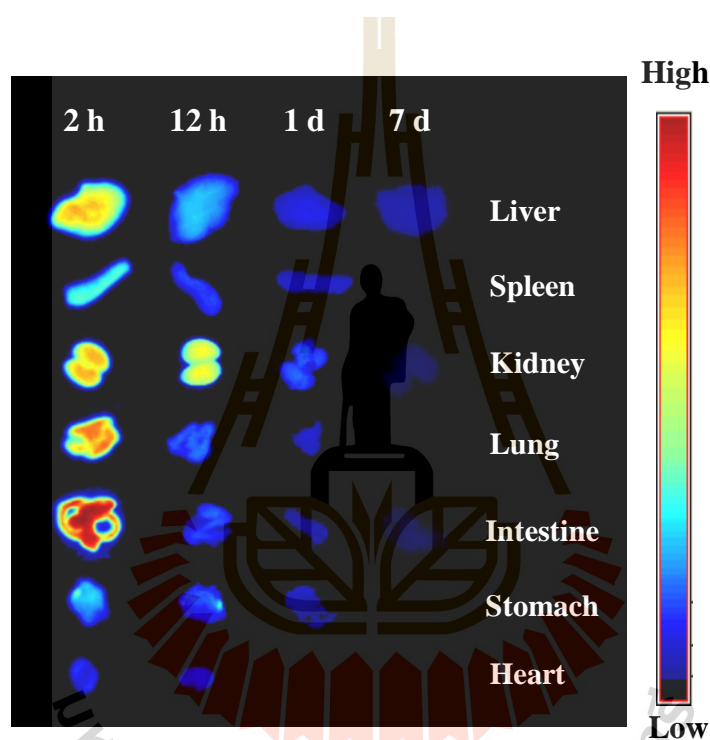
Figure 4.37 *Ex vivo* fluorescence of major organs over 2 h, 12 h, 1 d, and 7 d.

Relative FL intensities at 7-day p.i. revealed the disappearance of signals in several organs, including spleen, kidney, lung, intestine, and heart, pointing out the completed clearance after injection for 7-day (Figure 4.38). Pa-PEG nanodots that remained in the liver might enter the bile *via* the hepatic circulation system, and further excreted in feces (Kapusta, 2007).
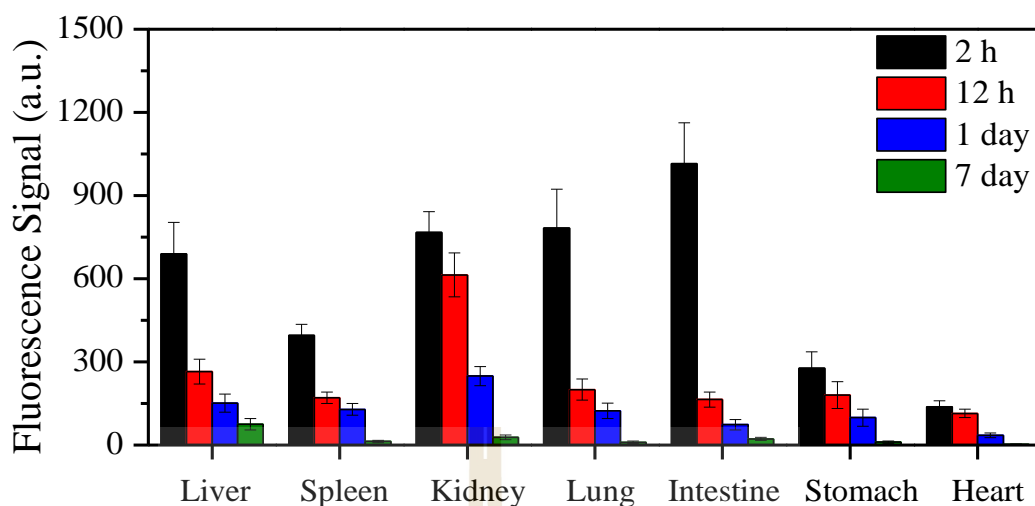
Figure 4.38 Fluorescent biodistribution of the Pa-PEG nanodots in major organs analysis.

Notably, biodistribution-based PA imaging in Figure 4.36 displayed that at 2 h p.i. PA signal in the liver was slightly higher than that of the kidney, while FL signals of the liver and kidneys at 2 h p.i. in Figure 4.38 were about the same intensities. These might be because a large amount of Pa-PEG nanodots in the liver and intestine regarding both imaging techniques came from a cooperative excretion, *via* bile clearance with an entero-hepatic cycle that causes biodistribution variation in the liver and intestine at the first 2 h, and *via* renal elimination (Rapozzi et al., 2010).

However, the renal removing pathway is dominant clearable behavior for long-term drainage owning to the ultra-small size of the Pa-PEG nanodots, which strongly supported by the observation of FL/PA signals in kidneys and fluorescent signal in the urine.

4.4.3.2 Blood analysis

Blood routine and blood biochemistry were examined to evaluate *in vivo* long-term toxicity of Pa-PEG nanodots (Figure 4.39). In blood routine examination, several variables were investigated, including white blood cells (WBC), red blood cells (RBC), hemoglobin (HGB), hematocrit (HCT), mean corpuscular volume (MCV), mean corpuscular hemoglobin concentration (MCHC), and platelet (PLT). In addition, the investigated parameters of blood biochemistry were Aspartate aminotransferase (AST), Alanine aminotransferase (ALT), Alkaline phosphatase (ALP), and UREA. It was found that there was no significant variant in AST, ALT, ALP, and UREA level indicating that the function of liver and kidney were normal (Cheng et al., 2017). Consequently, all blood routine and blood biochemistry parameters were remaining at the regular level as the untreated group within 7-day p.i., suggesting that the Pa-PEG nanodots are safe for *in vivo* PDT in short- and long-term circulation in the blood system.

4.4.3.3 Tissue morphology change

To verify that the Pa-PEG nanodots did not induce cytotoxicity, H&E staining of main organs demonstrated no noticeable eradication of tissues for long-time treatment (Figure 4.40). All these results suggested that the inflammatory disorder response was rapidly improved through the rapid clearance of Pa-PEG nanodots over 7 days without tissue destruction or morphology change. Therefore, the Pa-PEG nanodots could be safely used for *in vivo* long-term imaging-guided PDT.
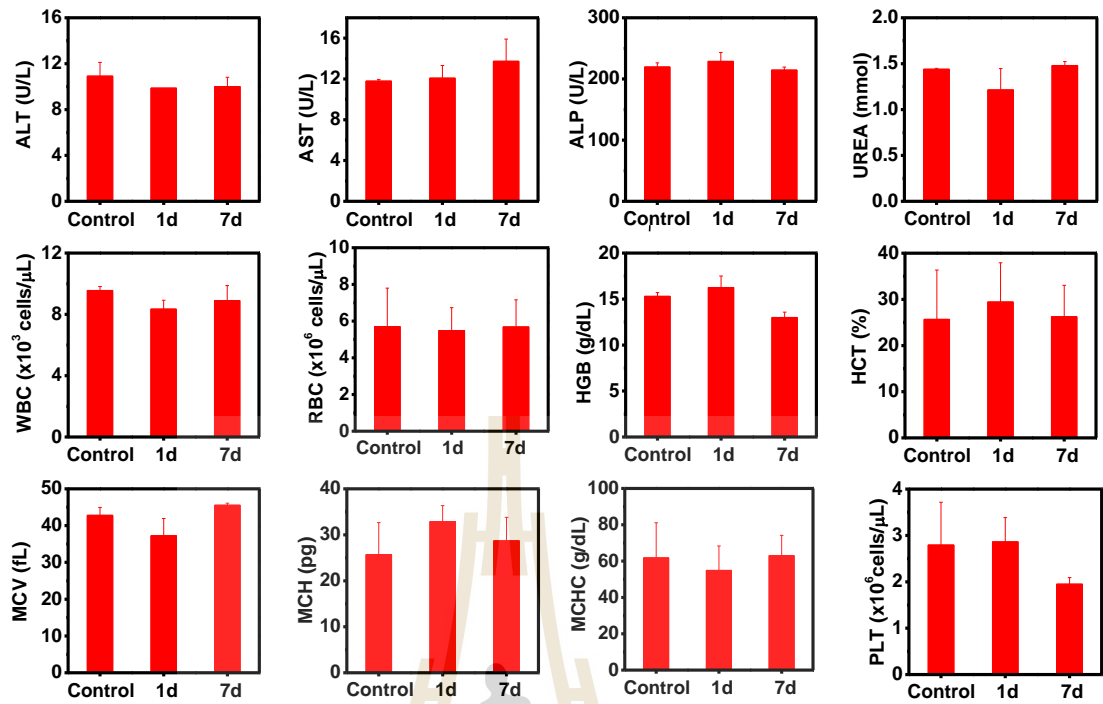
Figure 4.39 Blood routine and blood biochemistry analysis.
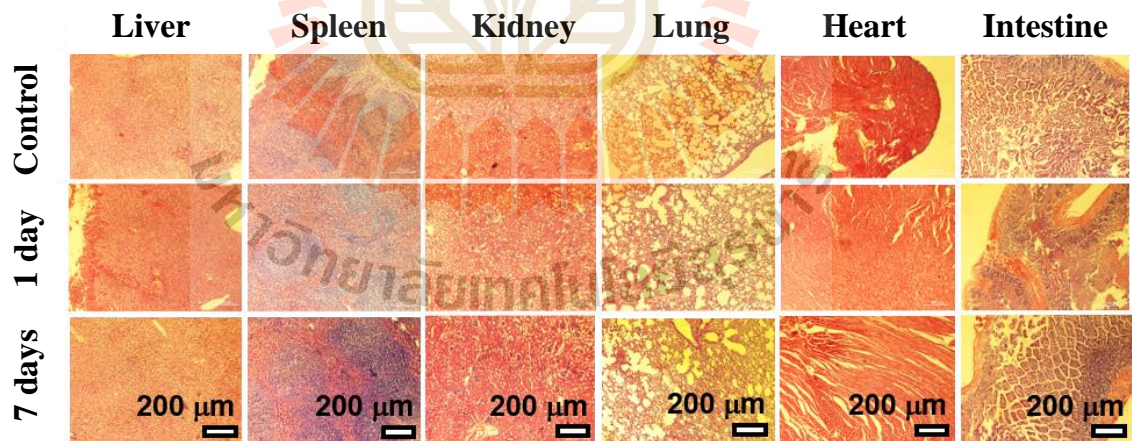
Figure 4.40 H&E stained major organs.

4.4.3.4 Anti-tumor efficacy

In vivo PDT was investigated using 4T1 xenograft mice. Twenty mice were randomly divided into 4 groups (n = 5); (i) PBS injection for control, (ii) 660 nm lamp irradiation only (10 mW cm^{-2}, 60 min), (iii) Pa-PEG nanodots only (300 μL, 1.8 mg mL^{-1}), and (iv) Pa-PEG nanodots with 660 nm lamp irradiation at 8 h p.i.. Tumor size was measured every other day for 14 days using a caliper. Figure 4.41 showed that tumors from the treatment group were significantly affected by the eradication from photodynamic phenomena after light exposure, while tumors from other three control groups were continuously grown in a similar manner over the period of 14 days. Hence, the combination of the Pa-PEG nanodots injection and lamp excitation demonstrated an effective anti-tumor efficacy.
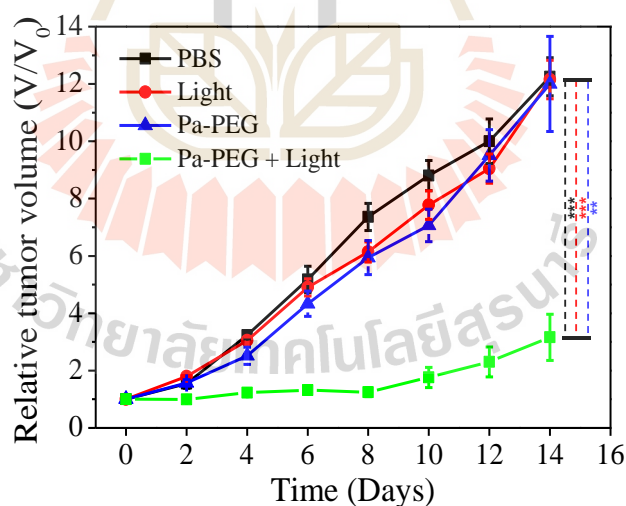
Figure 4.41 The tumor growth curves of 4 different groups (n = 5) of balb/c mice after various treatment: PBS injection (control); 660 nm lamp irradiation only (light); Pa-PEG injection only (Pa-PEG); and the Pa-PEG nanodots injection with 660 nm lamp irradiation (Pa-PEG + light). Statistical analysis is based on independent t-test (***p < 0.001, **p < 0.01, or *p < 0.05)

4.4.3.5 Health assessment and tumor checkup

After PDT treatment, tumor weight and tumor size at day 14 also confirmed the effectiveness of light-induced PDT with Pa-PEG nanodots treatment (Figure 4.42, Figure 4.43). The tumor weight obtained from the PDT treatment group was obviously lighter and smaller than the other three control groups. The comparison between the representative mouse from each group on day 0 and day 14 clearly established Pa-PEG nanodots as a powerful PDT agent (Figure 4.44).
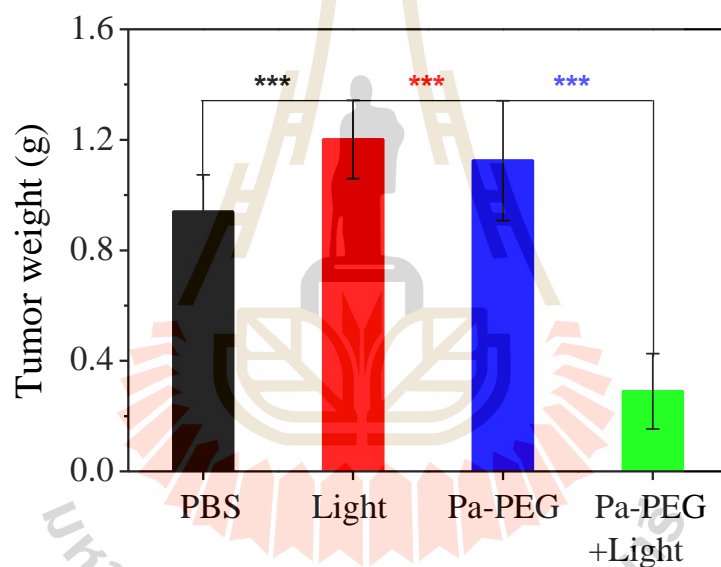
Figure 4.42 Tumor weight of different groups taken at the 14 days.
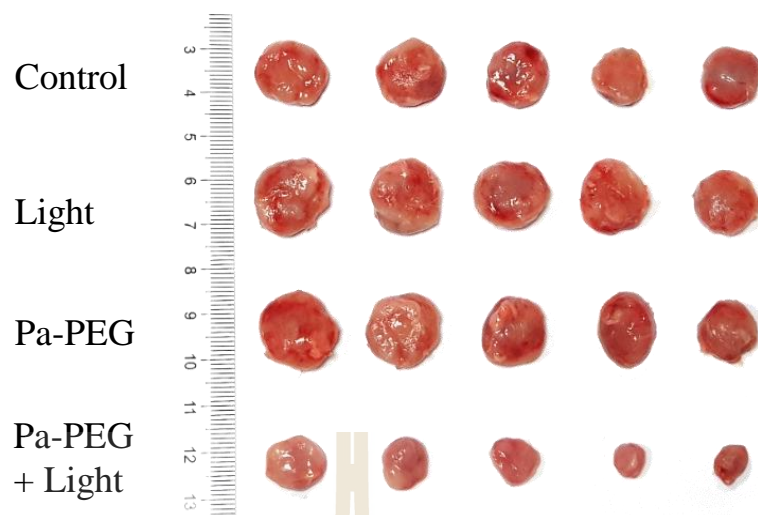
Figure 4.43 Photographs of the tumor tissue at the 14 days.

Figure 4.44 H&E staining of tumor after various treatments.

Moreover, H&E staining conducted after 16 h post-treatment showed that most of the cancerous cells were destroyed, whereas the other three non-treatment groups exhibited no significant transformation of cell morphology compared with the tumors from the control group (Figure 4.45). Furthermore, the bodyweight rate of all groups was monitored throughout the treatment period, in which no significant weight loss was observed, indicating all of the mice remained in the healthy state until the end of the experiment (Figure 4.46).

| | Control | Light | Pa-PEG | Pa-PEG + Light |
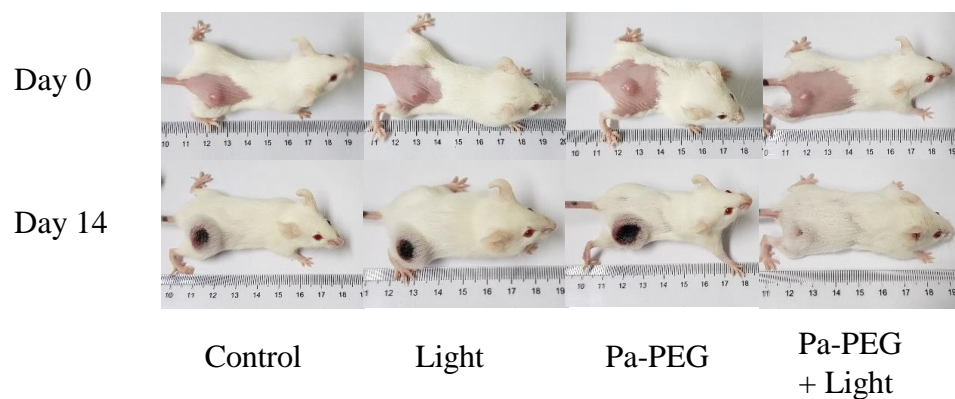
Figure 4.45 Representative photographs of mice from different groups taken before (day 0) and after treatment at 14 days.
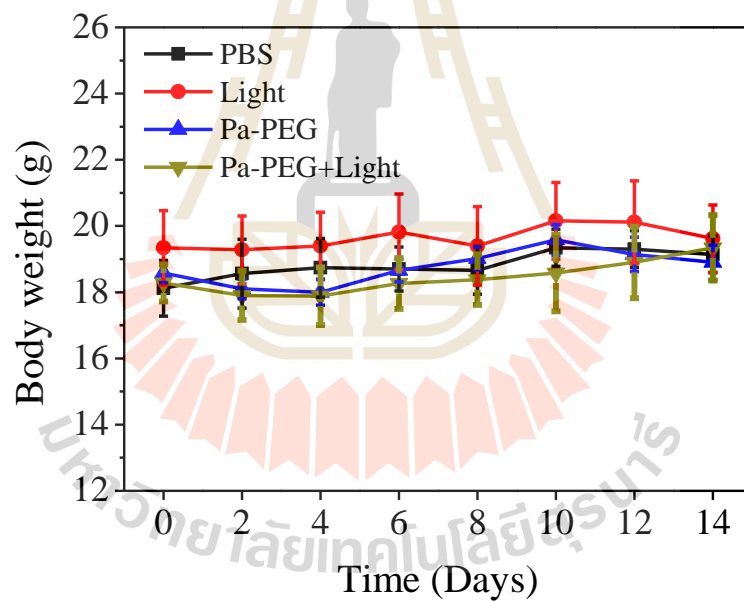
Figure 4.46 The body weight curves of each treatment groups.

4.5 References

Abdellatif, D. A. A. H., Osman, S., Mohd-Ali, M. T., and Darras, F. (2016). N-terminal mono-PEGylation of octreotide. **PJIDRD**. 1: 1-8.

Arami, H., Khandhar, A., Liggitt, D., and Krishnan, K. M. (2015). *In vivo* delivery, pharmacokinetics, biodistribution and toxicity of iron oxide nanoparticles. **Che Soc Rev**. 44(23): 8576-8607. doi:10.1039/C5CS00541H.

Cheng, L., Jiang, D., Kamkaew, A., Valdovinos, H. F., Im, H.-J., Feng, L., England, C. G., Goel, S., Barnhart, T. E., Liu, Z., and Cai, W. (2017). Renal-clearable PEGylated porphyrin nanoparticles for image-guided photodynamic cancer therapy. **Adv Funct Mater**. 27(34): 1702928. doi:10.1002/adfm.201702928.

Du, B., Yu, M., and Zheng, J. (2018). Transport and interactions of nanoparticles in the kidneys. **Nat Rev Mater**. 3: 358-374. doi:10.1038/s41578-018-0038-3.

Honary, S., and Zahir, F. (2013). **Effect of zeta potential on the properties of nano-drug delivery systems - A Review (Part 2)** (Vol. 12).

Kapusta, D. (2007). Drug Excretion. In S. J. Enna and D. B. Bylund (Eds.): **xPharm: The comprehensive pharmacology reference** (pp. 1-2). New York: Elsevier.

Li, W., Tan, G., Zhang, H., Wang, Z., and Jin, Y. (2017). Folate chitosan conjugated doxorubicin and pyropheophorbide acid nanoparticles (FCDP–NPs) for enhance photodynamic therapy. **RSC Adv**. 7(70): 44426-44437. doi:10.1039/C7RA08757H.

Li, X., Lee, D., Huang, J.-D., and Yoon, J. (2018). Phthalocyanine-assembled nanodots as photosensitizers for highly efficient type I photoreactions in photodynamic therapy. **Angew Chem Int Ed**. 57(31): 9885-9890. doi:10.1002/anie.201806551.

Pietrangeli, D., Rosa, A., Pepe, A., Altieri, S., Bortolussi, S., Postuma, I., . . . Ricciardi, G. (2015). Water-soluble carboranyl-phthalocyanines for BNCT. Synthesis, characterization, and *in vitro* tests of the Zn(ii)-nido-carboranyl-hexylthiophthalocyanine. **Dalton T**. 44(24): 11021-11028. doi:10.1039/C5DT 00394F.

Rapozzi, V., Zacchigna, M., Biffi, S., Garrovo, C., Cateni, F., Stebel, M., Zorzet, S., Bonora, G. M., Drioli, S., Xodo, L. (2010). Conjugated PDT drug: Photosensitizing activity and tissue distribution of PEGylated pheophorbide a. **Cancer Biol Ther**. 10(5): 471-482. doi:10.4161/cbt.10.5.12536.

Shen, S., Jiang, D., Cheng, L., Chao, Y., Nie, K., Dong, Z., Kutyreff, C. J., Engle, J. W., Huang, P., Cai, W., Liu, Z. (2017). Renal-clearable ultrasmall coordination polymer nanodots for chelator-free ^{64}Cu-labeling and imaging-guided enhanced radiotherapy of cancer. **ACS Nano**. 11(9): 9103-9111. doi:10.1021/acsnano.7b03857.

Tang, W., Yang, Z., Wang, S., Wang, Z., Song, J., Yu, G., Fan, W., Dai, Y., Wang, J., Shan, L., Niu, G., Fan, Q., and Chen, X. (2018). Organic semiconducting photoacoustic nanodroplets for laser-activatable ultrasound imaging and combinational cancer therapy. **ACS Nano**. 12(3): 2610-2622. doi:10.1021/acs nano.7b08628.

Würthner, F., Kaiser, T. E., and Saha-Möller, C. R. (2011). J-Aggregates: From serendipitous discovery to supramolecular engineering of functional dye materials. **Angew Chem Int Ed**. 50(15): 3376-3410. doi:10.1002/anie.2010 02307.

Zou, Q., Abbas, M., Zhao, L., Li, S., Shen, G., and Yan, X. (2017). Biological photothermal nanodots based on self-Assembly of peptide–porphyrin conjugates for antitumor therapy. **J Am Chem Soc**. 139(5): 1921-1927. doi:10.1021/jacs.6b11382.
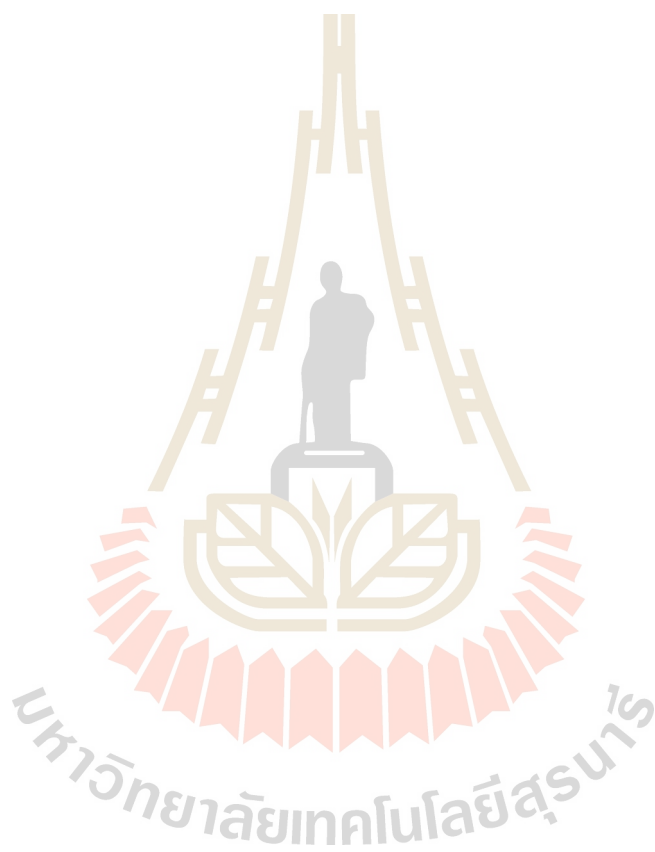
CHAPTER VI

CONCLUSION

In this thesis, we reported a facile method to prepare NPs for dual-modal imaging-guided PDT combined with renal clearable function. Pyropheophorbide-a (Pa) was conjugated with polyethylene glycol 5K (PEG) to obtain Pa-PEG nanodots with diameter ~2 nm from TEM. Optical characterizations demonstrated that the Pa-PEG nanodots showed a fluorescent and photoacoustic signal in a dose-dependent manner, which could serve as a nanoprobe for monitoring the nanodots accumulation at the tumor site. Moreover, the singlet oxygen production rate of the Pa-PEG nanodot was approximately two times improved against free Pa molecules. *In vitro* studies suggested that the Pa-PEG nanodots revealed an excellent photodynamic therapy effect with 92% 4T1-tumor cell elimination after exposure to 660 nm irradiation for 30 min. As monitored by the FL/PA dual-modal imaging *in vivo*, the nanodots could accumulate at the tumor site via EPR effect and reached the maximum concentration at 8 h p.i., which was considered as the appropriate time for PDT treatment. Finally, the tumor growth rate of the xenograft mice treated with the Pa-PEG nanodots (1.8 mg mL^{-1}, 300 µL) was effectively inhibited by PDT. In addition, the observation of fluorescent signal in urine implied that these small particles could be excreted out of the body via the renal pathway. Based on this study, the Pa-based nanodots are a remarkable tumor-pointer in living organisms and can minimize long-term toxicity by showing rapid clearance, after PDT treatment.
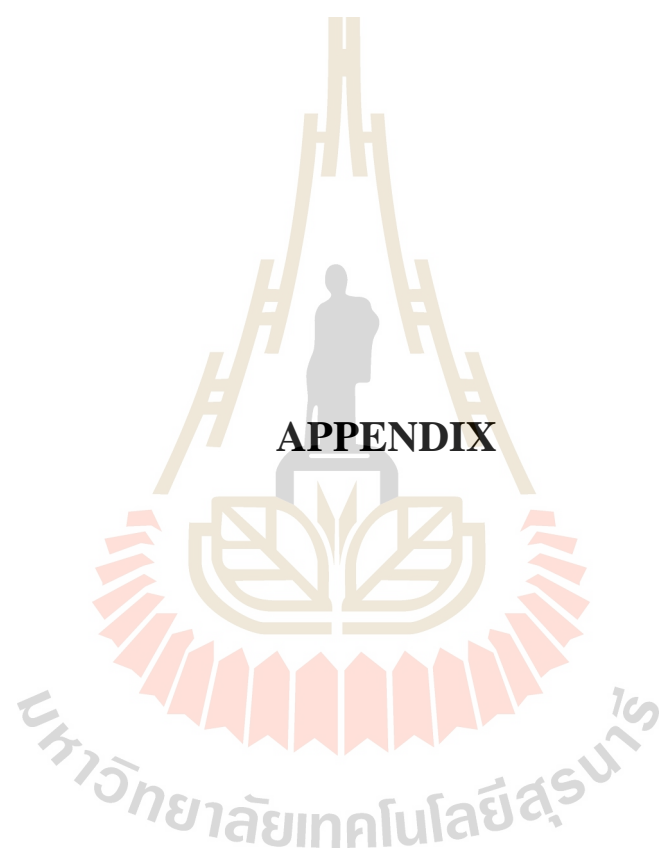
APPENDIX

APPENDIX A

THESIS OUTPUT

Publication

     Siwawannapong, K., Zhang, R., Lei, H., Jin, Q., Tang, W., Dong, Z., Lai, RY., Liu, Z., Kamkaew, A., and Cheng, L. (2020). Ultra-small Pyropheophorbide-a Nanodots for Near-infrared Fluorescence/Photoacoustic Imaging-guided Photodynamic Therapy. **Theranostics**. 10(1): 62-73. doi:10.7150/thno.35735

Awards

     Poster presentation award as presenting author of the poster "*PEGylated Pyropheophorbide-a for Fluorescence/Photoacoustic Dual-modal Imaging-guided Photodynamic Therapy*" in the session Imaging Cancer Therapy II, in: The 14th European Molecular Imaging Meeting (EMIM) 2019, Scotland.

     Oral presentation award in the recognition of outstanding oral presentation entitles "*PEGylated Pyropheophorbide-a for Fluorescence/Photoacoustic Dual-modal Imaging-guided Photodynamic Therapy*" in the 6th Thailand International Nanotechnology Conference (Nano Thailand) 2018, Thailand.

CURRICULUM VITAE

Name   Mister Kittipan Siwawannapong

Date of Birth February 19th, 1995, Nakhon Ratchasima, Thailand

Education

2013-2016 B.Sc. (Chemistry), First class honors, Suranaree University of

     Technology, Nakhon Ratchasima, Thailand

2017-Present M.Sc. candidate (Organic Chemistry), Suranaree University of

     Technology, Nakhon Ratchasima, Thailand

Scholarship

2015-Present Development and Promotion of Science and Technology Talents

     Project (DPST), supported by Thai government.

Publications

    Siwawannapong, K., Zhang, R., Lei, H., Jin, Q., Tang, W., Dong, Z., Lai, RY., Liu, Z., Kamkaew, A., and Cheng, L. (2020). Ultra-small Pyropheophorbide-a Nanodots for Near-infrared Fluorescence/ Photoacoustic Imaging-guided Photo-dynamic Therapy. **Theranostics**. 10(1): 62-73. doi:10.7150/thno.35735.

    Siriwibool, S., Kaekratoke, N., Chansaenpak, K. **Siwawannapong, K.**, S., Panajapo, P., Sagarik, K., Noisa, P., Lai, R-Y., and Kamkaew, A. (2020). Near-Infrared Fluorescent pH Responsive Probe for Targeted Photodynamic Cancer Therapy. **Sci. Rep**. 10(1283): doi.org/10.1038/s41598-020-58239-5.